

**STUDIES ON SYNCHROTRON RADIATION INDUCED
CONTAMINATIONS AND DEVELOPMENT OF OPTICS
REFURBISHING TECHNIQUES**

By
PRAVEEN KUMAR YADAV
PHYS03201404002

Raja Ramanna Centre for Advanced Technology, Indore

A thesis submitted to the
Board of Studies in Physical sciences
In partial fulfillment of requirements
for the degree of
DOCTOR OF PHILOSOPHY
of
HOMI BHABHA NATIONAL INSTITUTE

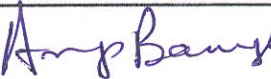
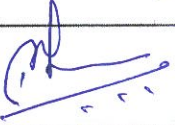
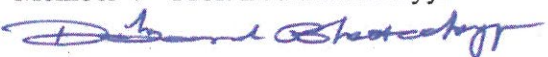


July, 2021

Homi Bhabha National Institute

Recommendations of the Viva Voce Committee

As members of the Viva Voce Committee, we certify that we have read the dissertation prepared by **Praveen Kumar Yadav** entitled "**Studies on Synchrotron Radiation Induced Contaminations and Development of Optics Refurbishing Techniques**" and recommend that it may be accepted as fulfilling the dissertation requirement for the award of Degree of Doctor of Philosophy.

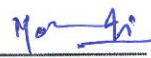
Chairman – Prof. Arup Banerjee		Date 10/06/2021
Guide/Convener – Prof. Mohammed H. Modi		Date 10.6.2021
Examiner – Prof. D.M. Phase		Date 10.6.2021
Member 1 – Prof. Tapas Ganguli		Date 10/06/2021
Member 2 – Prof. A.K. Karnal		Date 10/06/2021
Member 3 – Prof. S.M. Gupta		Date 10.06.2021
Member 4 – Prof. D. Bhattacharyya		Date 10/06/2021

Final approval and acceptance of this thesis is contingent upon the candidate's submission of the final copies of the thesis to HBNI.

I/We hereby certify that I/we have read this thesis prepared under my/our direction and recommend that it may be accepted as fulfilling the thesis requirement.

Date: 10.6.2021

Place: RRCAT, Indore


(Guide: Prof., M.H. Modi)

STATEMENT BY AUTHOR

This dissertation has been submitted in partial fulfillment of requirements for an advanced degree at Homi Bhabha National Institute (HBNI) and is deposited in the Library to be made available to borrowers under rules of the HBNI.

Brief quotations from this dissertation are allowable without special permission, provided that accurate acknowledgement of source is made. Requests for permission for extended quotation from or reproduction of this manuscript in whole or in part may be granted by the Competent Authority of HBNI when in his or her judgment the proposed use of the material is in the interests of scholarship. In all other instances, however permission must be obtained from the author.



Praveen Kumar Yadav

DECLARATION

I, hereby declare that the investigation presented in the thesis has been carried out by me. The work is original and has not been submitted earlier as a whole or in part for a degree/diploma at this or any other Institution/University.



Praveen Kumar Yadav

List of Publications arising from the thesis

Journals

1. “Ex-situ characterization of synchrotron radiation induced carbon contamination on LiF window”, P.K. Yadav, M.H. Modi, M.K. Swami, P.J. Singh, *Journal of Electron Spectroscopy and Related Phenomena*, **2016**, 211, 64–69.
2. “Structural variation in a synchrotron-induced contamination layer (a-C:H) deposited on a toroidal Au mirror surface”, P. K. Yadav, R. K. Gupta, M. K. Swami and M. H Modi, *J. Synchrotron Rad.* **2017**, 24, 757–764.
3. “Refurbishing of Au coated toroidal mirror by capacitively coupled RF plasma discharge”, P. K. Yadav, M. Kumar, R. K. Gupta, M. Sinha, J. A. Chakera and M. H. Modi, *J. Synchrotron Rad.* **2019**, 26, 1152–1160.
4. “Carbon removal from mirror like gold surface by UV light, RF plasma and IR laser exposure: A comparative study”, P. K. Yadav, R. K. Gupta, A. K. Choubey, S. Ali, U. K. Goutam, M. H. Modi. *Applied Optics*, **2021**, 60(1), 89-97.

Conferences

1. “Cleaning of optical surfaces by capacitively coupled RF discharge plasma”, P. K. Yadav, M. Kumar, S. K. Rai, J. A. Chakera, C. Mukherjee, M. Nayak, P. A. Naik, and G. S. Lodha, *AIP Conf. Proc.*, **2014**, 1591, 890-892.
2. “Removal of carbon contaminations by RF plasma generated reactive species and subsequent effects on optical surface”, P. K. Yadav, M. Kumar, S. K. Rai, M. H. Modi, J. A. Chakera, M. Nayak, P. A. Naik and G. S. Lodha, *AIP Conf. Proc.*, **2015**, 1665, 080062.
3. “Synchrotron radiation induced contamination on LiF window: Characterization by Raman spectroscopy”, P. K. Yadav and M. K. Swami, *AIP Conf. Proc.*, **2016**, 173, 080069.

4. “Refurbishing of carbon contaminated pre-mirror of reflectivity beamline at Indus-1”, P. K. Yadav, M. Kumar, R. K. Gupta, M. Sinha, H. S. Patel, and M. H. Modi, *AIP Conf. Proc.*, **2018**, 1942, 080052.
5. “Use of zero order synchrotron radiation for in-situ cleaning of beamline optics: Results of trial experiments”, P. K. Yadav, R. K. Gupta and M. H. Modi, *AIP Conf. Proc.* **2019**, 2115, 030290.
6. “Analysis of Au film surface after carbon layer removal with ultra violet radiation, rf plasma and IR laser”, P. K. Yadav, R. K. Gupta, A. K. Choubey, Sabir Ali and M. H. Modi, *AIP Conf. Proc.* **2020**, 2265, 030253.



Praveen Kumar Yadav

Dedicated to.....

My Beloved Parents and Family Members

ACKNOWLEDGEMENTS

First and foremost, I wish to express my heartfelt gratitude to my research guide **Dr. Mohammed Hussien Modi** for his inspiring guidance, strong motivation, valuable advice and encouragement from the very early stage of this research. I am also indebted to him for patiently going through the various versions of my thesis and for his critical comments.

I would also like to express my sincere gratitude to **Dr. Shailendra Kumar** for his generous involvement, constructive inputs and the numerous fruitful discussions.

I am highly grateful to **Dr. G. S. Lodha**, Ex. Head, Indus Synchrotron Utilization Division and **Dr. Tapas Ganguli** Head, Synchrotron Utilization Section, RRCAT, for giving me the excellent opportunity to carry out my research work and providing me all the infrastructure and required facilities during the course of this research. Their constructive comments and moral help during all aspects of this work have provided a good basis for the present thesis.

With gratitude, I acknowledge **Dr. Arup Banerjee** Dean Academic at RRCAT, **Dr. Harnath Ghosh**, **Dr. Avijit Choudhary**, **Dr. L.M. Kukreja**, **Dr. Mukesh Joshi**, **Dr. S.R. Mishra** faculty at RRCAT, HBNI for their constant help and support.

My sincere thanks go to my dissertation committee members **Dr. P. A. Naik**, **Dr. S. M. Oak**, **Dr. (Smt.) Rama Chari**, **Dr. D. Bhattacharyya**, **Dr. A. K. Karnal** and **Dr. S. M. Gupta** for their enlightening suggestions, support and encouragement during annual course evaluations which were important in improving the quality of this research.

I would like to thank to all our colleagues in department, especially **Dr. Anil Sinha, Dr. Sanjay Rai, Dr. C. Mukherjee, Dr. Pragya Tiwari, Shri. S. R. Kane, Dr. Rahul Shukla, Dr. P. N. Rao, Mr. R. K. Gupta, Mr. M. N. Singh, Mr. U. K. Goutam, Mr. P. D. Saxena, Mr. Rajneesh Dhawan, Mr. Mukund Kumar, Dr. A. K. Choubey, Mr. Sabir Ali and Dr. D. M. Phase, Dr. M. Gupta and Dr. V. Sathe** from UGC-DAE-Indore for immense help during experiments.

I would like to acknowledge all the **teachers**; I learnt from since my childhood, I would not have been here without their guidance, blessings and support.

I convey my heartfelt gratitude to all my family members especially to my parents for their love and encouragement throughout my life. I express my eternal gratitude to my brothers and sisters for their constant emotional support, without their constant support and encouragement, this work would not have reached the present stage.

Last but not least I would like to thank my wife **Anupama Yadav** for her exceptional care, personal support and great patience throughout these years. I would like to express thanks to my daughters **Dona** and **Darsha** who in her own way geared me up to reach the goal.

CONTENTS

	Page No.
SUMMARY	vi
LIST OF FIGURES	viii
LIST OF TABLES	xv
CHAPTER 1: INTRODUCTION	1-22
1.1 Overview.....	1
1.2 Nature of Synchrotron Radiation Induced Carbon Layer.....	4
1.3 Growth Mechanism of Synchrotron Radiation Induced Carbon Layer.....	6
1.3.1 Adsorption of Hydrocarbon Gases.....	6
1.3.2 Cracking of Adsorbed Hydrocarbons.....	8
1.3.2.1 Cracking of Hydrocarbons by SR Photons...	8
1.3.2.2 Cracking of Hydrocarbons by Secondary Electrons.....	9
1.4 Thickness of Carbon Layer.....	10
1.5 Consequences of Carbon Deposition on Synchrotron Optics.....	11
1.5.1 Reflectivity Loss near Carbon K-edge.....	11
1.5.2 Reflectivity Loss due to Destructive Interference in High Energy Region.....	12
1.5.3 Effect of Surface Roughness on Reflectivity.....	14
1.5.4 Variation in Reflected Intensity Ratio of P to S Polarizations of SR Beam.....	15
1.6 Techniques for Carbon Removing from Optical Components.....	16
1.7 Scope of Present Work.....	21

CHAPTER 2: OPTICS REFURBISHING SETUPS AND EXPERIMENTAL TECHNIQUES	23-66
2.1 Overview.....	23
2.2 Optics Refurbishing Setups.....	23
2.2.1 Inductively Coupled RF Plasma Source	23
2.2.2 Capacitively Coupled RF Plasma Cleaning Setup..	25
2.2.2.1 Electrode Assembly and Vacuum Chamber	25
2.2.2.2 Importance of rf Frequency.....	27
2.2.2.3 Effect of Electrodes Dimensions.....	29
2.2.2.4 Optimization of rf Power and Exposure Time... ..	31
2.2.3 UV Cleaning Setup.....	34
2.2.3.1 Description of In-situ Cleaning Setup at Reflectivity Beamline of Indus-1	35
2.2.3.2 Xenon Excimer UV Radiation Setup for Carbon Cleaning.....	38
2.2.4 IR Laser Cleaning Setup.....	41
2.2.4.1 Optimization of Laser System for Carbon Cleaning.....	44
2.3 Surface Analysis Techniques.....	49
2.3.1 Soft X-ray Reflectivity (SXR).....	49
2.3.1.1 Soft X-ray Reflectivity Beamline at Indus-2.....	51
2.3.2 Grazing Incidence X-ray Diffraction (GIXRD)....	53
2.3.3 X-ray Photoelectron Spectroscopy (XPS).....	55
2.3.4 Atomic Force Microscopy (AFM).....	57
2.3.4.1 Modes of AFM Operation.....	60
2.3.5 Raman Spectroscopy.....	61
2.3.6 Optical Emission Spectroscopy.....	64
2.4 Summary.....	65

CHAPTER 3: CHARACTERISTICS OF SYNCHROTRON RADIATION INDUCED CARBON LAYER.....	67-90
3.1 Overview.....	67
3.2 Samples for Study.....	69
3.2.1 Toroidal Mirror of Reflectivity Beamline.....	69
3.2.2 LiF Window of HRVUV Beamline.....	70
3.3 Contamination Layer Thickness and Density.....	71
3.4 Crystallinity of Synchrotron Radiation Induced Carbon Layer.....	74
3.5 Chemical Analysis of Synchrotron Radiation Induced Carbon Layer.....	78
3.5.1 X-ray Photoelectron Spectroscopy.....	78
3.5.2 Raman Analysis of Synchrotron Radiation Induced Carbon Layer.....	80
3.6 Summary.....	89
CHAPTER 4: REFURBISHMENT OF X-RAY OPTICS BY CAPACITIVE COUPLED RF PLASMA.....	91-106
4.1 Overview.....	91
4.2 Refurbishment of Carbon Contaminated X-ray Mirrors	92
4.2.1 Cleaning of Carbon Contaminated Spherical Mirror using rf plasma.....	92
4.2.2 Cleaning of Carbon Contaminated Toroidal Mirror using RF plasma.....	97
4.3 Analysis of Mirror Surface before and after Plasma Exposure.....	98
4.3.1 Structural Analysis and Reflectivity Gain of X-ray Mirror after Plasma Exposure.....	98
4.3.2 Surface Morphology before and after Plasma Exposure.....	102
4.3.3 Raman Spectra of Mirror Surface before and after Plasma Exposure.....	103
4.4 Summary.....	105

CHAPTER 5: REFURBISHMENT OF X-RAY OPTICS BY ULTRAVIOLET IRRADIATION.....	107-125
5.1 Overview.....	107
5.2 Mechanism of UV Radiation Cleaning.....	108
5.3 Cleaning Characteristics of Au Thin Film Surface using 172 nm UV Radiations.....	110
5.3.1 Structural and Optical Parameters and Soft X-ray Reflectivity of UV cleaned Surface.....	111
5.3.2 Surface Analysis by XPS in Carbon K-edge Region	114
5.3.3 Analysis of Bulk Structural Properties by GIXRD..	115
5.3.4 Analysis of Surface by Raman Spectroscopy.....	116
5.4 <i>Ex-situ</i> Cleaning of Synchrotron Optics by UV Radiation Exposure.....	118
5.5 <i>In-situ</i> Mirror Cleaning by Zero Order Synchrotron Radiations.....	120
5.5.1 In-situ Cleaning Procedure for Post Mirror Cleaning at Reflectivity Beamline of Indus-1.....	121
5.5.2 Results of <i>In-situ</i> Cleaning of Post Mirror.....	122
5.6 Summary.....	124
CHAPTER 6: REFURBISHMENT OF X-RAY OPTICS BY IR LASER SCANNING.....	126-155
6.1 Overview.....	126
6.2 Absorption of Laser Energy and Temperature Rise of Material.....	127
6.3 Material Response during Laser Exposure.....	129
6.4 Threshold Fluence for Laser Cleaning.....	132
6.5 Carbon Removal from X-ray Optics like Surface using IR Laser.....	133
6.5.1 Sample for Study.....	133
6.5.2 Carbon Removal using IR Laser.....	134
6.6 Characterization of Carbon Coated Au Surface after Laser Treatment.....	136

6.6.1	Structural and Optical Parameters before and after Carbon Cleaning.....	136
6.6.2	XPS Analysis of Au Surface before and after Carbon Cleaning.....	139
6.6.3	Analysis of Au Surface before and after Carbon Cleaning by Raman Spectroscopy.....	140
6.6.4	Analysis of Bulk Structural Properties by GIXRD.....	141
6.7	Comparison of IR Laser Cleaning with UV and RF Plasma Cleaning.....	143
6.7.1	Surface and Bulk Properties after Carbon Removal.....	143
6.7.2	Chemical Property of Surface after Carbon Cleaning.....	151
6.8	Summary.....	155
CHAPTER 7:	CONCLUSIONS AND FUTURE WORK.....	156-158
	APPENDIX (I-IV).....	159-171
	REFERENCES.....	172-186

LIST OF FIGURES

S. No.	Title of Figure	Page No.
1.1	Quadrupole mass analyzer spectrum (partial pressure of residual gases) recorded at reflectivity beamline of Indus-1 in absence of synchrotron radiation beam.....	2
1.2	Synchrotron radiation induced carbon contaminated spherical gold coated mirror. The black region at mirror surface represents carbon contaminations.....	4
1.3	Schematic representation of adsorption, desorption and reflection of hydrocarbon molecules on optics surface.....	7
1.4	Representation of cracking of adsorbed hydrocarbon molecules by incident photons, reflected photons and by secondary electrons on Au surface.....	9
1.5	Comparison of soft x-ray (50 eV-320 eV) reflectivity of carbon contaminated Au mirror to pristine Au mirror at 2 degree incidence angle.....	12
1.6	Effect of carbon layer thickness on x-ray reflectivity of carbon contaminated Au mirror in 300 eV to 2 keV energy range at 2.5 degree incidence angle (simulated from CXRO website).....	13
1.7	X-ray reflectivity of carbon contaminated Au mirror in 300 eV to 2 keV energy range at 2.5 degree incidence angle. Effect of surface roughness of carbon layer on reflectivity is also shown (simulated from CXRO website).....	14
2.1	Schematic diagram for optics cleaning using inductively coupled plasma source.....	24
2.2	Schematic diagram of electrode assembly used for generating capacitively coupled rf plasma.....	26
2.3	In-house developed capacitive coupled rf (13.56 MHz) plasma cleaning system.....	27

2.4	Schematic representation of self bias voltage (V_{sb}) developed on powered electrode (a) Asymmetric configuration (b) Symmetric configuration.....	30
2.5	Self bias voltage (V_{sb}) on power electrode (a) by varying applied RF power (b) by varying oxygen gas pressure.....	31
2.6	X-ray reflectivity of Pt surface before and after plasma exposure (a) Different exposure time at 10 watts power (b) Different power at 30 minutes exposure time.....	33
2.7	X-ray photoelectron spectra of Au surface before and after plasma exposure at 10 W rf power and at 5×10^{-2} mbar oxygen pressure for 20 minutes of exposure.	34
2.8	Mechanical layout of reflectivity beamline (BL-04) at Indus-1 SR source.....	36
2.9	Schematic diagram of post mirror section with gas inlet system for <i>insitu</i> cleaning of post mirror (TM2) at reflectivity beamline of Indus-1.....	37
2.10	Xenon lamp (EX-mini L12530-01) used for cleaning of mirror and grating.....	39
2.11	Confocal microscopy images ($355 \mu\text{m} \times 473 \mu\text{m}$) of Pt/C samples after different exposure time by excimer UV radiations at 5 mm distance from source.....	40
2.12	Soft x-ray reflectivity of Pt/C samples after different exposure time by UV radiations at 5 mm distance from source.....	41
2.13	Yb:YAG fiber laser configuration, showing cavity formed by inter core fiber Bragg gratings.....	42
2.14	Schematic diagram of laser beam steering with x and y galvanometer mirror drives.....	43
2.15	Laser beam spot diameter with (a) laser power (b) scan speed (c) pulse frequency.....	45
2.16	Calculated values of (a) laser fluence and (b) beam spot overlapping with laser scan speed.....	46

2.17	The confocal microscopic images ($473\ \mu\text{m} \times 355\ \mu\text{m}$) after carbon cleaning from Au thin film surfaces at different scanning parameters: power, scan speed (v), number of passes and hatching separation.....	48
2.18	Representation of x-ray reflection at an interface of two different refractive index (n_1 and n_2) materials.....	50
2.19	Optical layout of reflectivity beamline at Indus-2 synchrotron source. Various optical elements of the beamline are indicated in figure.....	52
2.20	Inside view of experimental chamber with goniometer, x-y-z sample scanning stages and detector at reflectivity beamline of Indus-2.....	53
2.21	Experimental station for diffraction measurement at angle dispersive X-ray diffraction beamline (BL-12) of Indus-2 SR source.....	54
2.22	Schematic diagram of X-ray Photoelectron Spectroscopy experimental setup.....	57
2.23	Schematic diagram of atomic force microscope (AFM) apparatus and related basic components.....	59
2.24	Energy level diagram of Raman scattering indicating Stokes, Anti-stokes and Rayleigh lines.....	62
2.25	Schematic diagram of optical emission spectrometer used for measuring optical emission lines of CO and O in rf plasma chamber during optics cleaning.....	64
3.1	Indus-1 reflectivity beamline (BL-04) optical layout with carbon-contaminated Au coated pre-mirror. TM1 and TM2 represent pre and post toroidal mirrors, S1 and S2 represents entrance and exits slits.....	70
3.2	Carbon contaminated LiF window of 50 mm diameter. Marked area in photograph indicates contamination region as well as SR beam foot print	71
3.3	Experimentally measured and fitted reflectivity spectra of (a) carbon-contaminated Au mirror surface (b) carbon contaminated LiF window surface.....	72

3.4	Grazing incidence X-ray diffraction pattern of SR induced carbon contamination layer from Au mirror surface.....	75
3.5	Grazing incidence X-ray diffraction pattern measured by Cu K_{α} radiation ($\lambda=1.54 \text{ \AA}$) source (a) carbon contamination layer deposited on LiF window (b) commercial graphitic carbon sample.	76
3.6	Magnified image of diffraction spectra of contaminated layer at (a) $2\theta = 28.3^{\circ}$ (b) $2\theta = 75.3^{\circ}$	77
3.7	Carbon (1s) XPS spectra recorded using Al K_{α} (1486.6 eV) radiation source from carbon contaminated LiF surface and commercial graphitic carbon samples. Inset shows survey scan in 200 eV-1100 eV energy range.....	79
3.8	Measured and fitted Raman spectrum of (a) synchrotron radiation induced carbon deposited on LiF window (b) Raman spectrum taken from commercial graphitic carbon.....	81
3.9	Carbon contaminated mirror, intersection point of vertical lines (orange color) and horizontal line (blue) indicates the Raman measurement point. The distance between the points is 25 mm.....	82
3.10	(a) Raman spectra (P-1 to P-12) from the surface of contaminated mirror, measurement points are shown in Figure 3.9. (b) corresponding D and G-peak positions (i-ii), D and G-peak width (iii-iv), I(D)/I(G) ratios (v-vi) cluster size (nm) (vii), calculated from Lorentzian fittings..	83
3.11	Plot of ratio of the slope (m) of the linear background of Raman spectrum to the G-peak intensity as a function of distance from the mirror center.....	88
4.1	Carbon contaminated toroidal gold mirror removed from reflectivity beam line (BL-04) of Indus-1 for carbon cleaning experiments	93
4.2	Optical emission spectrum recorded at different time during cleaning of carbon contaminated mirror by rf plasma exposure.....	94
4.3	Refurbished gold coated toroidal mirror after rf plasma exposure for one hour.....	96

4.4	Gold coated spherical mirror (a) before and (b) after plasma exposure.....	97
4.5	Measured (open circles) and fitted (continuous lines) soft x-ray reflectivity spectra taken before and after the removal of carbon contamination layer. Vertical dashed lines indicate the position of critical momentum transfer (Q_c) for C and Au.....	100
4.6	(a) Energy (750 eV to 1500 eV) dependent soft x-ray reflectivity of mirror before and after rf plasma cleaning at 2 degree incidence angle (b) Change (ΔR) in soft x-ray reflectivity after plasma cleaning.....	102
4.7	Three dimensional atomic force microscopy images ($2.5\mu\text{m} \times 2.5\mu\text{m}$) (a) before and (b) after cleaning the mirror. AFM images clearly indicate that surface topography of mirror changes after carbon cleaning	103
4.8	Raman spectra (a) before (black) and (b) after (red) plasma exposure from mirror surface. P-1 to P-12 indicates measurement points on mirror surface in interval of 25 mm along the length of mirror.....	105
5.1	Mechanism of carbon removal by UV radiation in presence of oxygen environment.....	110
5.2	(a) Measured and fitted soft x-ray reflectivity spectra of carbon coated Au film, before and after carbon layer removal and pristine Au sample (b) Energy dependent soft x-ray reflectivity spectra of pristine Au, carbon coated (Au/C) and after carbon cleaning by UV exposure.....	113
5.3	Deconvoluted XPS spectra in carbon K-edge region (a) Au/C untreated (b) Au/C UV treated (c) Au untreated samples.....	114
5.4	Grazing incidence angle X-ray diffraction spectra before and after carbon cleaning from Au thin film surfaces.....	116
5.5	Raman spectra of (a) Pristine Au surface (b) Carbon cleaned Au surface by UV radiation exposure (c) Untreated carbon coated (Au/C) thin film surface.....	117

5.6	Pt coated post mirror (TM2) (a) before (b) after UV radiation exposure of 7 hrs.....	119
5.7	Au coated mirror (TM1) (a) before (b) after UV radiation exposure of 18 hrs.....	120
5.8	Au coated grating (a) before (b) after UV radiation exposure of 18 hrs.....	120
5.9	Reflectivity ratios of two independent measurements before cleaning the mirror in 100 eV-300 eV energy range.....	123
5.10	(a) Measured photon intensity in reflectivity beamline before (black curve) and after (red curve) in-situ cleaning the post mirror (b) Photon intensity ratio after cleaning to before cleaning.....	124
6.1	Confocal microscopic images ($473 \times 355 \mu\text{m}^2$) of carbon cleaned gold thin film surfaces (gold deposited on Si wafer) at two different fluence values (a) $F=0.26 \text{ J/cm}^2$ and (b) 0.5 J/cm^2 . The marked black spots represent damage region of gold surface at 0.5 J/cm^2 fluence value...	133
6.2	Gold coated mirror (a) Before carbon coating (b) After carbon coating	134
6.3	Schematic diagram of laser beam scanning on carbon coated surface. L_x and L_y represents sample length and width, S_x and S_y represents laser beam size in x and y directions and V_{scan} represents laser scan speed in x direction.....	135
6.4	The confocal microscopic images ($473 \mu\text{m} \times 355 \mu\text{m}$) of carbon coated Au thin film surface (a) before and (b) after laser cleaning at 0.26 J/cm^2 fluence and at 85% overlapping of laser pulses.....	136
6.5	Measured and fitted soft x-ray reflectivity spectra before and after carbon cleaning from Au surface by IR laser and pristine Au surfaces.....	137
6.6	XPS spectra in C (1s) region (a) Au/C untreated, (b) Au/C laser treated and (c) pristine Au samples.....	139

6.7	Raman spectra of carbon coated Au surface before and after carbon IR laser exposure cleaning.....	141
6.8	Grazing incidence x-ray diffraction spectra of carbon coated Au samples (a) before (b) after IR laser treatments for carbon removal.....	142
6.9	(a) Measured and fitted soft x-ray reflectivity spectra (b) Relative optical density profile of carbon coated Au surface, before and after carbon layer removal with UV, RF plasma and IR laser techniques. Vertical dashed line in (a) represents carbon critical momentum position on x -axis.	144
6.10	Energy dependent soft x-ray reflectivity spectra of untreated carbon coated Au film surface, before and after carbon layer removal and pristine Au thin film surface.....	146
6.11	Grazing incidence X-ray diffraction spectra of untreated carbon coated Au film surface, before and after carbon layer removal and pristine Au thin film surface.....	148
6.12	Diffraction peaks area intensity ratios of Au (220) to Au (111) peak before and after different surface treatments.....	148
6.13	Atomic force microscopic images ($5 \times 5 \mu\text{m}^2$) of (a) Pristine Au, (b) Unexposed Au/C (c) UV exposed Au/C (d) Plasma exposed Au/C (e) IR laser exposed Au/C	150
6.14	Deconvoluted XPS spectra in C (1s) (a) Untreated Au/C (b) Pristine Au (c) Au/C plasma treated (d) Au/C UV treated (e) Au/C laser treated sample surfaces.....	151
6.15	XPS C (1s) peak area intensity ratio of untreated Au/C, pristine Au, laser, plasma and UV treated Au/C to untreated Au, obtained using XPS.....	152
6.16	Raman spectra of carbon coated Au film before and after different treatments for carbon removal. (a) Pristine Au (b) Plasma treated (c) UV treated (d) Laser treated (e) Au/C untreated. Various peaks (G, D, D2, D4) related to graphitic carbon are indicated in (d) and (e).....	154

LIST OF TABLES

S. No.	Title of Table	Page No.
2.1	Structural parameters (thickness (t), roughness (σ)) of Pt/C sample determined by soft x-ray reflectivity curves fitting after different time of UV exposure.....	41
3.1	Structural (t- thickness, σ - roughness and O.D- optical density) and optical (δ and β) parameters of carbon contamination layer deposited on Au coated mirror surface measured at three different wavelengths of incident radiation.....	73
3.2	Structural (t- thickness, σ - roughness and O.D- optical density) and optical (δ and β) parameters of carbon contamination layer deposited on LiF window surface measured at three different wavelengths of incident radiation.....	74
4.1	Structural parameters [thickness (t), roughness (σ)] and optical constants (δ and β) of carbon, gold and chromium layers of carbon contaminated mirror before and after plasma cleaning obtained by the fitting of soft x-ray (1200 eV) reflectivity data.....	100
5.1	Optical and structural parameters obtained by curve fittings of soft x-ray reflectivity curves (measured at $\lambda=90 \text{ \AA}$) of pristine Au, carbon coated Au sample before and after carbon layer removal. Bulk optical constant values are indicated in bracket.....	113
6.1	Optical and structural parameters obtained by soft x-ray ($\lambda=90 \text{ \AA}$) reflectivity curve fittings using SRxrr tool. Bulk optical constant values are mentioned in bracket.....	138
6.2	Optical and structural parameters obtained by soft x-ray ($\lambda=90 \text{ \AA}$) reflectivity curve fittings of carbon coated Au film before and after carbon layer removal using UV, RF plasma and IR laser surface exposures.	145

7 Conclusions and Future Work

Synchrotron radiation induced carbon contamination on optical elements is a serious issue in SR beamlines. The characteristic of carbon deposition in SR beamlines is not well known and still debatable. In order to know characteristics of SR induced carbon layer on optical elements, SR induced carbon contaminated Au coated toroidal mirror of reflectivity beamline and a LiF window of high resolution vacuum ultraviolet beamline of Indus-1 are taken for a case study. A detailed characterization of these two objects is carried out using different surface analysis techniques. Detail analyses of different data taken from carbon contaminated Au mirror surface reveals that nature of carbon growth has direct correlations with synchrotron dose. Red shift in G and D peaks positions in Raman Spectra (RS) indicates that number of carbon layer stage increases with photon dose and the carbon layer has mixed phases of sp^3 and sp^2 hybridized carbon contents. Raman Spectroscopy results also reveal that disordering and cluster size in the layer increases with photon dose. The contamination layer has presence of hydrogen (hydrogenated carbon layer) and hydrogen contents decrease with photon dose. Soft x-ray reflectivity results indicate that maximum carbon layer thickness is of the order of 406 Å and surface roughness ~60 Å. The density of carbon layer in maximum thickness region is about 75% of graphitic carbon density. The Raman Spectroscopy and XPS results of carbon layer deposited on LiF window surface also show graphitic carbon nature.

In order to refurbish the contaminated optics, a capacitively coupled RF plasma system is in-housed developed. The system parameters are optimized such that the

process does not damage the Au or Pt coating of actual mirror. At optimized parameters the system was successfully used to clean different mirrors of Indus synchrotron beamlines. Post cleaning characterization using different analytical techniques suggests that the mirror surface and Au coating remains intact after the optimized cleaning process. An in-situ cleaning technique is deployed at Indus-1 reflectivity beamline for post mirror cleaning. After exposure of ~ 40 hrs with zero order synchrotron radiations in presence of oxygen environment the photon intensity in carbon K-edge region increases by 35%. Excimer based UV radiation and Yb:YAG infrared nanoseconds (*ns*) pulsed laser facilities are also setup in laboratory for optics refurbishing applications. All these techniques are used for cleaning various optical components of Indus synchrotron beamlines. In order to find out merits and demerits of cleaning techniques results of all three techniques used in study are compared. In-situ cleaning by zero order synchrotron radiation is not included in the comparison because the sample was different as it was in case of RF plasma, UV and IR laser treatments.

In comparative study of carbon removal from mirror like surfaces using UV radiation, RF plasma and IR laser, it is observed that UV and RF plasma exposures completely removed carbon without affecting the surface roughness whereas the IR laser exposed samples show the presence of carbon in Raman and XPS spectra but not in SXR. These results suggest that after IR laser treatment some carbon particulates resettled on the cleaned surface from the removal debris as the used suction system needs further optimization to remove the carbon debris effectively. Redeposition of carbon particles restricts the efficiency laser cleaning technique. UV and plasma cleaned

samples showed a gain in the soft x-rays reflectivity near carbon K-edge region in comparison to carbon coated Au sample whereas the IR laser treated sample showed reflectivity gain near carbon K-edge region but not upto pristine Au surface reflectivity. In low energy region (100 eV to 200 eV) the sample shows loss in the reflectivity in comparison the pristine sample. The carbon removal by zero order synchrotrons radiation in presence of oxygen partial pressure is relatively slow process. Maintaining oxygen partial pressure (10^{-3} to 10^{-4} mbar) in surrounding the optics in presence of zero order synchrotron radiation and UV radiation intensity in bending magnet based beamlines limit the technique.

Properties of synchrotron radiation induced carbon contamination layer depend on various factors such as vacuum condition, partial pressure of residual gases, photon energy, exposure time (dose) etc. It is observed that the chemical composition of SR induced carbon layer varies from hydrogenated polymeric carbon to diamond like carbon via hydrogenated graphitic carbon and in some cases mixed phases of carbon. In the present thesis work it is found that the property of synchrotron radiation induced carbon is varying with photon dose. In this study we have not attempted to quantify the role of photon energy in the photo-dissociation of hydrocarbon. Therefore a study on properties of carbon deposits with different energy photons at different partial pressure of different hydrocarbon gases can be carried out in future.

In literature it is mentioned that both primary photons and secondary electrons participate in dissociation of adsorbed hydrocarbons but it is not clear what are their relative contributions. Quantification of role of primary photon and secondary electrons in dissociation is also a good problem for future work.

SUMMARY

Synchrotron radiation induced carbon contamination on optical elements is a serious issue in SR beamlines. The characteristic of carbon deposition in SR beamlines is not well known and still debatable. In order to know characteristics of SR induced carbon layer on optical elements, SR induced carbon contaminated Au coated toroidal mirror of reflectivity beamline and a LiF window of high resolution vacuum ultraviolet beamline of Indus-1 are taken for a case study. A detailed characterization of these two objects is carried out using different surface analysis techniques. Detail analyses of different data taken from carbon contaminated Au mirror surface reveals that nature of carbon growth has direct correlations with synchrotron dose. Red shift in G and D peak positions in Raman Spectra (RS) indicates that number of carbon layer stage increases with photon dose and the carbon layer has mixed phases of sp^3 and sp^2 hybridized carbon contents. Raman Spectroscopy results also reveal that disordering and cluster size in the layer increases with photon dose. The contamination layer has presence of hydrogen (hydrogenated carbon layer) and hydrogen contents decrease with photon dose. Soft X-ray reflectivity results indicate that maximum carbon layer thickness is of the order of 406 \AA and surface roughness $\sim 60 \text{ \AA}$. The density of carbon layer in maximum thickness region is about $\sim 75\%$ of graphitic carbon density. The Raman Spectroscopy and XPS results of carbon layer deposited on LiF window surface also show graphitic carbon nature.

In order to refurbish the contaminated optics, a capacitively coupled RF plasma system is in-housed developed. The system parameters are optimized such that the process does not damage the Au or Pt coating of actual mirror. At optimized

parameters the system was successfully used to clean different mirrors of Indus synchrotron beamlines. Post cleaning characterization using different analytical techniques suggests that the mirror surface and Au coating remains intact after the optimized cleaning process. An in-situ cleaning technique is deployed at Indus-1 reflectivity beamline for post mirror cleaning. After exposure of ~ 40 hrs with zero order synchrotron radiations in presence of oxygen environment the photon intensity in carbon K-edge region increases by 35%. Excimer based UV radiation and Yb:YAG infrared nanoseconds (*ns*) pulsed laser facilities are also setup in laboratory for optics refurbishing applications. All these techniques are used for cleaning various optical components of Indus synchrotron beamlines. In order to find out merits and demerits of cleaning techniques results of all three techniques are compared.

In comparative study of carbon removal from mirror like surfaces using UV radiation, RF plasma and IR laser, it is observed that UV and RF plasma exposures completely removed carbon without affecting the surface roughness whereas the IR laser exposed samples show the presence of carbon in Raman and XPS spectra but not in SXR. These results suggest that after IR laser treatment some carbon particulates resettled on the cleaned surface from the removal debris as the used suction system needs further optimization to remove the carbon debris effectively. Redeposition of carbon particles restricts the efficiency of laser cleaning technique. UV and plasma cleaned samples showed a gain in the soft x-rays reflectivity near carbon K-edge region in comparison to carbon coated Au sample whereas the IR laser treated sample showed reflectivity gain near carbon K-edge region but not upto pristine Au surface reflectivity. In low energy region (100 eV to 200 eV) the sample shows loss in the reflectivity in comparison the pristine sample.

1 Introduction

1.1 Overview

Synchrotron radiation (SR) sources have become a very important tool for the study of matter in physical, biological, chemical and medical sciences. New generation synchrotron radiation sources with high brilliance open new areas for fundamental and applied research. Broadband energy spectrum, high brilliance and coherence properties are salient features of the synchrotron radiation sources. For the optimum utilization of this kind of sources, the brilliance of the source must be maintained up to the experimental station by the use of high quality optical components in the beamlines. In order to reduce scattering, absorption of synchrotron radiation photons by gas molecules and to avoid optic contaminations, pressure of the synchrotron radiation beamlines is maintained in 10^{-9} - 10^{-10} mbar (UHV) range. Even in UHV environment of beamlines, traces of hydrogen and hydrocarbons gases are observed [1-2]. Figure 1.1 shows a typical residual gas spectrum of synchrotron beamline in absence of synchrotron radiation beam. The spectrum clearly shows that partial pressure of hydrocarbon gases lies in 10^{-9} to 10^{-10} mbar range. The partial pressure of hydrocarbon gases in beamline may vary depending on vacuum conditioning of beamline vacuum chamber. In presence of synchrotron radiation photons desorption of adsorbed gases (CO, CO₂, CH₄ and H₂O) from vacuum chamber walls and other components of beamline take place by photon/electron induced desorption (PID/EID) process [3]. These desorbed gas molecules increase the beamline pressure and form

couples of monolayer on optical element surfaces. The time taken to form a monolayer is inversely proportional to the pressure and is given by $t_{ml}(\text{sec}) = 2 \times 10^{-6} / P(\text{torr})$, where t_{ml} is monolayer's formation time and P is the pressure of residual gas in the chamber [4].

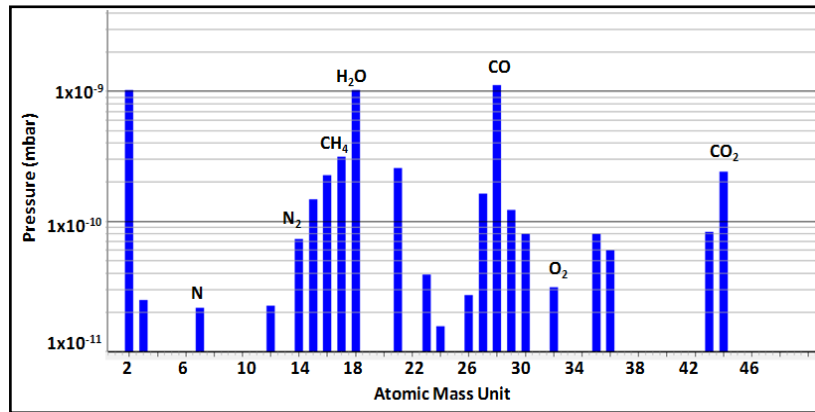


Figure 1.1: Quadrupole mass analyzer spectrum (partial pressure of residual gases) recorded at reflectivity beamline of Indus-1 in absence of synchrotron radiation beam.

The hydrocarbon molecules are attached to the surface with physisorption energies (10-300 meV) and the force between hydrocarbon molecules and surface atoms is Van der Waals type and the interaction among attached gas molecules is also limited [5]. In absence of any source of energy such as photons, electrons etc, it is observed that the buildup of carbon contamination on optical surfaces for a prolonged time period is hardly one or two monolayer's. In order to form thick layer of carbon on the surface the binding of hydrocarbon molecules with surface atoms and binding energy with other hydrocarbon molecules should be of the order of chemisorbs energy. Due to radiations exposure, the adsorbed hydrocarbon gas molecules dissociate into small reactive fragments (known as cracking). The fragmented reactive species react with surface and nearby other fragment molecules and begin to form large chains of

molecules in all directions. The presence of hydrocarbon gases with continuous radiations exposure leads to additional cross-linking resultant carbon layer thickness continues grow up to hundred times more compared to carbon layer grown by physically adsorbed gas molecules without radiation exposure [5-6]. Prolonged use of optical elements in synchrotron radiation beamlines in presence of hydrocarbon gases, a thick layer of carbon is generally formed on the surface of the optical elements. Several groups observed a carbon contamination layer on beamline optical components such as mirror and gratings [1], [2], [7]–[15]. Chauvet et al. have observed that the thickness of the deposited layer increases very rapidly, especially on the first beamline optics where synchrotron radiation intensity is high compare to other optical elements in the beamline. They also observed that when the carbon layer becomes thicker, the photon flux near carbon K-edge region decrease significantly [7]. The carbon contamination layer, not only reduce the photon flux in soft x-ray region near carbon K-edge but also reduce photon flux in hard x-ray region due to interference effect of this layer [8].

The nature of carbon and its growth mechanism is still debatable. Depending on carbon growth conditions the nature of the carbon in the contamination layer is not unique, it may be amorphous, hydrogenated graphitic carbon and/or hydrogenated diamond like carbon [2],[5],[15]. A typical synchrotron radiation induced carbon contaminated mirror in synchrotron radiation beamline is shown in Figure 1.2.

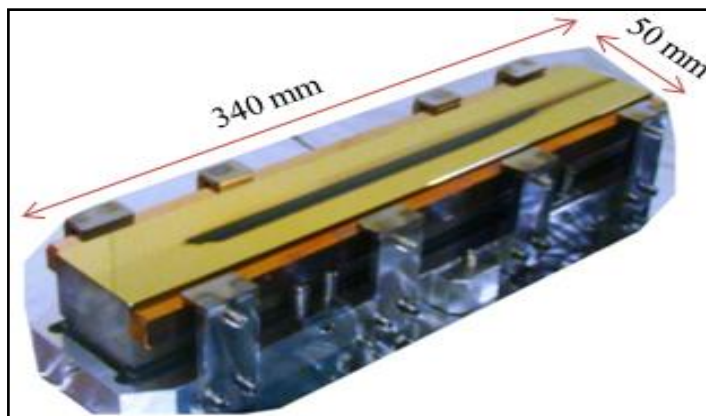


Figure 1.2: Synchrotron radiation induced carbon contaminated spherical gold coated mirror. The black region at mirror surface represents carbon contaminations.

Nature of synchrotron radiation induced carbon contamination layer with variation in photon exposure has not been studied in detail. The present thesis covers structural and optical characterization of synchrotron radiation induced contamination layer, design & development of carbon removal setups (RF plasma, UV and IR laser based), and their successful utilization for removal of contamination layer from actual synchrotron optics and thin film surfaces.

In this chapter nature of synchrotron radiation induced carbon, its growth mechanism on optical elements in the synchrotron radiation beamlines, its consequences on performances of mirror in the beamlines are discussed. In order to refurbish the contaminated optics a short description about *in-situ* and *ex-situ* optics cleaning techniques are also given.

1.2 Nature of Synchrotron Radiation Induced Carbon Layer

The nature (amorphous carbon, graphitic carbon, diamond like carbon or hydrogenated phase of carbon) of synchrotron radiation induced carbon is not well

known and still a matter of discussion [1]. The characteristics of synchrotron radiation induced carbon deposits strongly depend on deposition conditions such as type of hydrocarbon gas and its partial pressure, incident photon energy and exposure time (photon dose) etc. The growth of carbon layer is the result of complex interaction among hydrocarbon gas molecules, photons and/or electrons and the optics surface. In synchrotron radiation beam lines the optical elements such mirrors and gratings are exposed to broad band of photon energy. In case of pre-mirror, it is exposed to high photon flux of all energies start from infrared to hard x-ray, on the other hand post mirror and other optical elements installed after monochromator are exposed to energies allowed by monochromator, resultant the nature of carbon deposited on pre mirror and post mirror may be different. Kanda et al. [16] observed that when hydrogenated carbon layer is irradiated with synchrotron radiations, its hydrogen carbon bond (C-H) breaks and hydrogen concentration in the layer decreases with continuous irradiation, resultant density of the hydrogenated carbon layer increases with exposure time. They also suggested that structural changes of hydrogenated DLC films are associated with hydrogen desorption from the film. The structure of carbon layer deposited on optical elements determines the reflectivity loss in the beamline. Depending on hydrogen contents in carbon layer, its refractive index varies [17]. Takamatsu et al. [18] studied soft x-rays irradiation effect on fluorinated diamond like carbon film. They observed that $sp^2/(sp^2 + sp^3)$ ratio of carbon atoms increased, film thickness, density and composition ratio of fluorine atom in film decreased with synchrotron radiation dose. The characteristics of carbon layer may vary from polymeric like carbon (PLC) to diamond like carbon (DLC) depending on growth conditions. The denser structure of diamond-like carbon (DLC) film leads to more

absorption of soft x-ray and EUV radiations compared to a polymeric like carbon (PLC) layer or soft amorphous carbon layer of the same thickness. Furthermore, because the carbon in DLC form is more tightly bonded, the layers of DLC are likely to be more difficult to remove from optics surface. Dolgov et al. [15] observed hydrogenated diamond-like (DLC: H) and graphitic like (GLC:H) carbon coatings on the collector mirror of an extreme ultra-violet (EUV) source. We also studied the nature of synchrotron radiation induced carbon deposited on LiF window used in high resolution vacuum ultra violet (HRVUV) beamline at Indus-1 synchrotron source [19]. It is observed that carbon layer deposited after ~100 hrs of exposure of VUV radiations have graphitic and carbonado phase of carbon [20]. We also studied the variation in carbon phase deposited on pre-mirror (TM1) of reflectivity beamline of Indus-1 with photon dose [21]. We observed that with increase in dose of irradiating photons the carbon phase vary from hydrogenated amorphous carbon (a-C:H) to hydrogenated graphitic carbon (GC: H). It is also observed that the carbon cluster size, sp^2 hybridizations and disordering in the carbon layer increases with photon dose[2].

1.3 Growth Mechanism of Synchrotron Radiation Induced Carbon Layer

1.3.1 Adsorption of Hydrocarbon Gases

The growth of carbon on the surface of optics is not a single step process; it starts from adsorption of hydrocarbon species on optic surface in the form of monolayer. Depending upon the binding energy between adsorbate and adsorbent the adsorption can be divided into two categories, the physical-adsorption (adsorption energy lies in

10-300 meV range) and the chemical-adsorption (adsorption energy lies in 1-10 eV range) [4]. Adsorption, desorption and reflection of hydrocarbon gas molecules simultaneously occurs on optics surface. The net rate of adsorption can be written as [5]

$$R_{net-ad} = R_a - R_d - R_f \quad (1.1)$$

Where R_a , R_d and R_f are rate of adsorption, desorption and reflection of gas molecules respectively. The detailed expressions for rate of adsorption (R_a), desorption (R_d) and reflection (R_f) are given in Appendix-I. The process of adsorption, desorption and reflection is schematically represented in Figure 1.3.

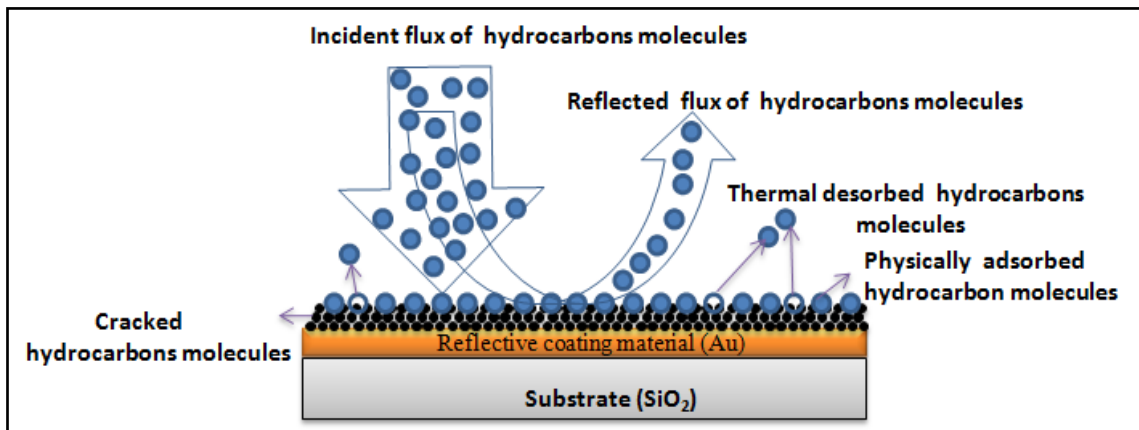


Figure 1.3: Schematic representation of adsorption, desorption and reflection of hydrocarbon molecules on optics surface.

Figure 1.3 pictorially shows that fraction of incident gas molecules are reflected back without any interaction with the surface and some are adsorbed on surface. In adsorbed gas molecules some are thermally desorbs and some cracked by photons and/or photoelectrons and convert into carbon layers.

Cracking of adsorbed hydrocarbons molecules take place by continuous exposure with photons as well as photoelectrons generated on the surface of optics. In such conditions the rate equation (1.1) is modified and one additional term related to the rate of cracking of hydrocarbons also comes in picture.

1.3.2 Cracking of Adsorbed Hydrocarbons

1.3.2.1 Cracking of Hydrocarbons by SR Photons

The optics used in beamlines are continuously exposed to synchrotron radiation photons. When these photons interact with adsorbed hydrocarbon molecules on optics surface, cracking of adsorbed hydrocarbons molecules take place by breaking the chemical bonds (C-C, C-O, C-H, C-OH etc.) of hydrocarbon molecules. When these cracked hydrocarbons crosslink a continuous layer of carbon is formed. For reflecting surfaces such as mirrors and gratings, total number of photons that are responsible for dissociation of adsorbed hydrocarbon layer includes, direct incident photons as well as reflected photons by optics surface (shown in Figure 1.4). The photo induced dissociation or cracking of hydrocarbon molecules is proportional to the incident photon flux ($I_0 - photons/area \times sec$) plus reflected photon flux ($I_0 R$) from optic surface (R is reflection coefficient) and the number density of adsorbed gas molecules ($n_{ad} - molecules/area$) on surface. The expression for photo-induced dissociation rate can be written as [5]

$$R_{photo-diss} = I_0 n_{ad} \sigma_{pho} (1 + R) \quad (1.2)$$

Where σ_{pho} - is photo-induced dissociation cross-section.

1.3.2.2 Cracking of Hydrocarbons by Secondary Electrons

Primary and secondary electrons both are generated on optics surface but dissociation cross section of adsorbed hydrocarbons with respect to secondary electron is higher in comparison to primary electrons resultant contribution of secondary electrons in dissociation of adsorbed hydrocarbons is more in comparison to the primary photoelectrons [22]. The reflecting layer of optics and the growing contamination layer on the reflecting surface both contribute in the number of secondary electrons with different secondary electron yields. The process of cracking of adsorbed hydrocarbon by photons and secondary electrons is schematically represented in Figure 1.4.

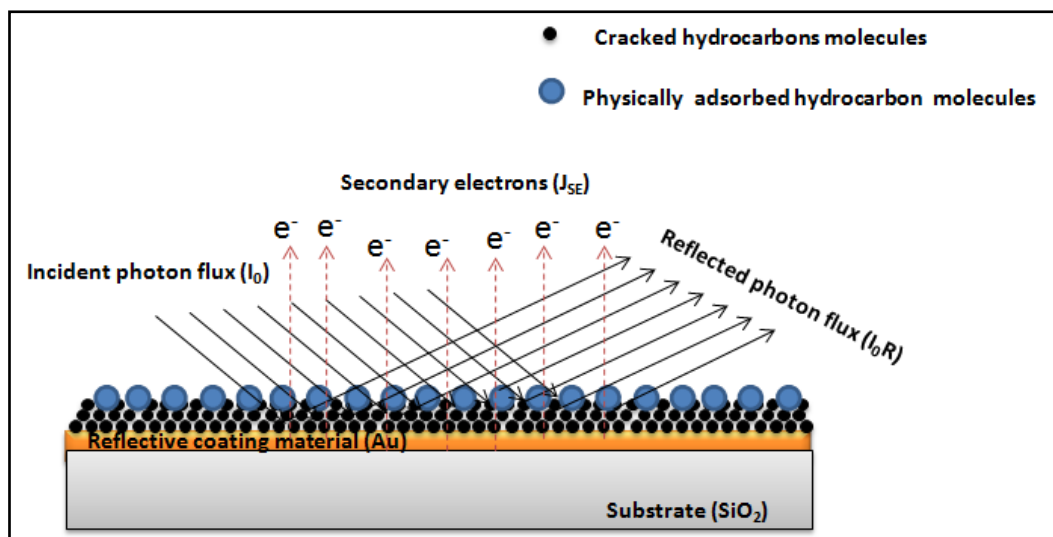


Figure 1.4: Representation of cracking of adsorbed hydrocarbon molecules by incident photons, reflected photons and by secondary electrons on Au surface.

The rate of cracking of adsorbed hydrocarbons by secondary electrons is proportional to secondary electron current, density of adsorbed hydrocarbon molecules and

dissociation cross section of hydrocarbons by secondary electrons. The rate equation can be written as [5]

$$R_{SE}(D) = n_{ad} \sigma_{SE} J_{SE} \quad (1.3)$$

Where n_{ad} , J_{SE} , σ_{SE} and D are numbers density of adsorbed molecules, secondary electron flux on optic surface, dissociation cross section for secondary electron and carbon layer thickness respectively. The expression for secondary electrons leaving the surface as a function of carbon layer thickness is given in Appendix-II.

Combining equation (1.2) and (1.3) total rate of cracking of adsorbed hydrocarbons at optics surface by primary SR photons and secondary electrons can be written as

$$R_{Cracking} = I_0 n_{ad} \sigma_{Pho} (1 + R) + n_{ad} \sigma_{SE} J_{SE}(D) \quad (1.4)$$

With consideration of cracking term, the new adsorption rate equation can be written as

$$R_{ad} = R_a - R_d - R_f - R_{Cracking} \quad (1.5)$$

1.4 Thickness of Carbon Layer

The carbon layer thickness is directly proportional to the rate of cracking of hydrocarbon molecules on optics surface. As number of cracked hydrocarbon molecules increase with respect to time by photon and secondary electron exposure the carbon layer thickness increases. The differential equation describing the thickness (D) of carbon layer can be written as [5]

$$\frac{dD}{dt} = VR_{Cracking} = V \left(I_0 \sigma_{pho} (1 + R) + \sigma_{SE} J_{SE}(D) \right) n_{ad} \quad (1.6)$$

Where V is volume occupied by carbon atom on optics surface

1.5 Consequences of Carbon Deposition on Synchrotron Optics

High brilliance, synchrotron sources have an imperative requirement of high quality optics to preserve wave-fronts while transporting high photon flux (10^{12-13} photons/s) from source point to the experimental station [23]. The important practical requirement is to transport the high flux of SR beam up to the experimental station through different optical elements mounted in the beamline for different applications such as focusing (mirror), monochromatization (grating) and harmonic order separator (HOS). The carbon contamination on optical elements in beamlines is becoming serious issue for achieving high brilliance up to experimental station. The carbon contaminated optics reduces photon flux [24]. The photon intensity reduction mainly occurs due to three main reasons (i) Strong absorption near carbon K-edge (284 eV) region (ii) Destructive interference by carbon layer (iii) Scattering losses due to increase in surface roughness by carbon deposition and Carbon layer thickness also vary p to s polarization ratio, this problem is more serious where polarization based experiments are carried out [8],[24]–[26].

1.5.1 Reflectivity Loss near Carbon K-edge

In soft x-ray region interaction of x-rays with material depends on refractive index $n(\omega)$ of the material. For x-ray mirrors and gratings application, the selection of material is made in such a way it should be chemically stable, its absorption edges should not lie in the chosen x-ray energy range and the critical angle of the material should also be sufficiently high for chosen x-ray energy. When synchrotron radiation induced carbon is deposited on the mirror surface, its properties changes resultant

reflectivity of mirror surface also change from pristine one. Figure 1.5 shows a comparison of soft x-ray reflectivity of carbon contaminated gold mirror with respect to fresh gold mirror in 50 eV to 320 eV energy range at 2 degree incidence angle. Carbon contaminated Au mirror reflectivity is measured at reflectivity beamline at Indus-1, whereas Au mirror reflectivity is simulated at 2 degree incidence angle by considering 1000 Å thick gold layer with surface roughness of 5 Å. The reflectivity spectrum of carbon contaminated mirror clearly show strong reflectivity loss (82% to 25%) near carbon K-edge (284 eV) due to strong absorption of incident photons by carbon atoms whereas without carbon layer mirror show more than 60% reflectivity in carbon K-edge region.

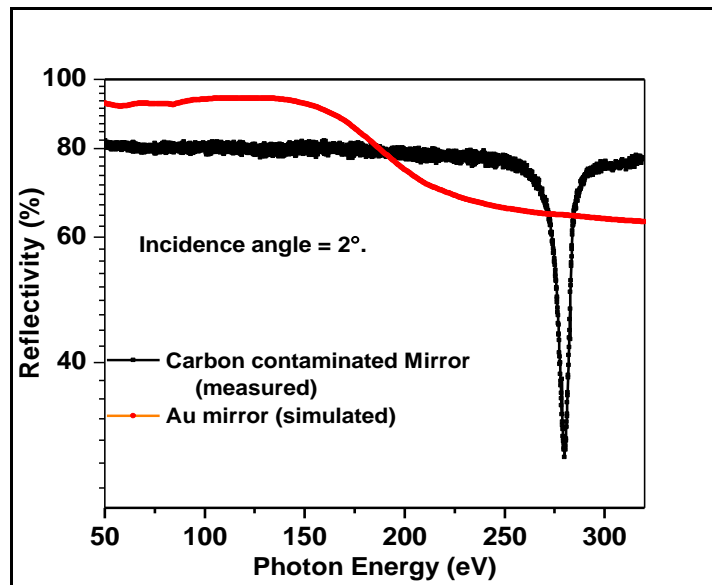


Figure 1.5: Comparison of soft x-ray (50 eV - 320 eV) reflectivity of carbon contaminated Au mirror to pristine Au mirror at 2 degree incidence angle.

1.5.2 Reflectivity Loss due to Destructive Interference in High Energy Region

For synchrotron radiation mirrors are based on principle of total external reflection of x-rays, resultantly there is no interference effect between substrate and the reflecting

layer. When a thin layer of carbon is deposited on mirror surface in synchrotron radiation beamline, it produces an interference effect due to penetration of beam through carbon layer because carbon layer has low critical angle compared to mirror material. The energy of photon and the layer thickness at a fixed incidence angle decide whether the interference is constructive or destructive.

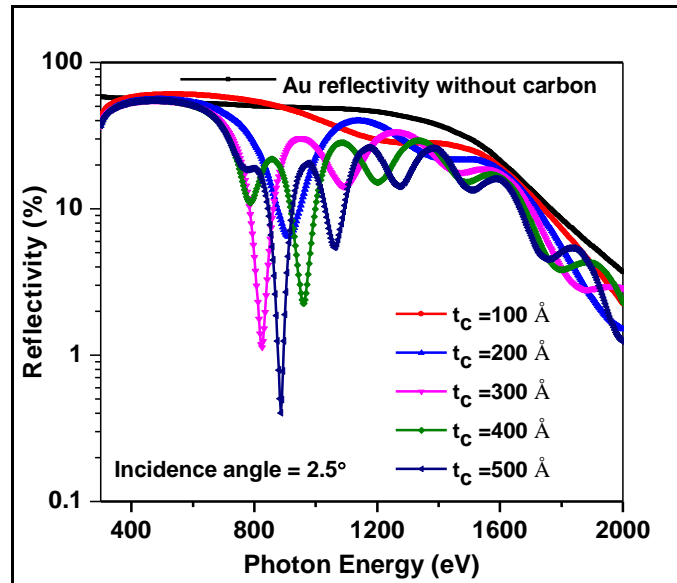


Figure 1.6: Effect of carbon layer thickness on x-ray reflectivity of carbon contaminated Au mirror in 300 eV to 2 keV energy range at 2.5 degree incidence angle (simulated from CXRO website [27]).

The simulated reflectivity spectra in Figure 1.6 show the effect of carbon layer thickness on reflectivity due to interference effect in 300 eV to 2 keV energy region. For reflectivity simulation gold thickness (1000 Å) and roughness (5 Å) are kept constants and carbon layer thickness varying from 0 to 500 Å in step of 100 Å and roughness (5 Å) of carbon layer is kept constants. X-ray reflected from top surface of carbon layer and the x-ray reflected from top surface of Au generate an interference fringe pattern. Depending on carbon layer thickness the interference pattern vary with

energy and incidence angle. Resultant intensity of SR beam pass through the carbon contaminated mirror also varying with carbon layer thickness (carbon layer thickness in the beamline increase with exposure time and incident photon energy).

1.5.3 Effect of Surface Roughness on Reflectivity

Due to non-uniform growth of carbon layer the surface roughness of the mirror increases [8]. During surface characterization of carbon contaminated mirror it is observed that the surface roughness of mirror increases from 16 Å to 60 Å due to carbon contamination deposition [26].

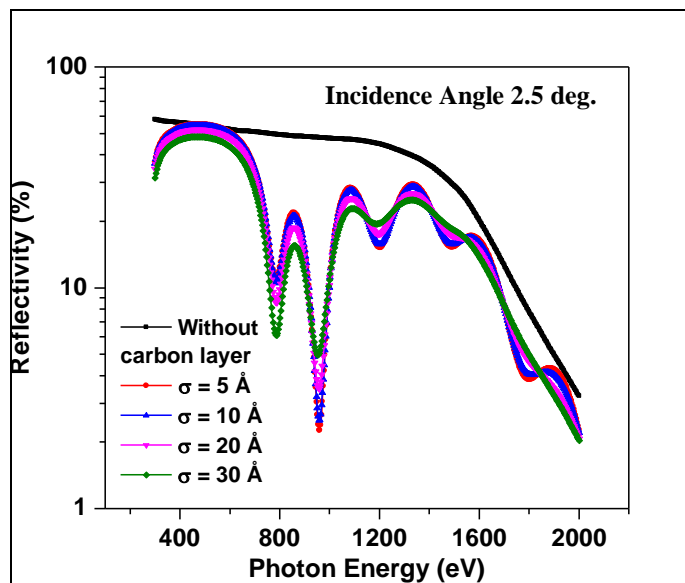


Figure 1.7: X-ray reflectivity of carbon contaminated Au mirror in 300 eV to 2 keV energy range at 2.5 degree incidence angle. Effect of surface roughness of carbon layer on reflectivity is also shown (simulated from CXRO website [27]).

Figure 1.7 shows the effect of surface roughness of carbon layer on reflectivity of carbon coated mirror. The spectra show the simulated reflectivity of Au mirror at 2.5 degree incidence angle in 300 eV to 2 keV energy range without carbon layer and with carbon layer of different roughness. For reflectivity simulation, gold layer thickness

(1000 Å) and roughness (5 Å) and carbon layer thickness (400 Å) are kept constants. Surface roughness of carbon layer varied from 5 Å to 30 Å. The reflectivity pattern clearly reveals that at a fixed energy when surface roughness of carbon layer increase the reflected intensity gradually decreases.

1.5.4 Variation in Reflected Intensity Ratio of P to S Polarizations of SR Beam

The carbon deposits on mirror surface not only reduces photon flux by absorption near absorption edge, scattering due to rough interface and destructive interference effect by carbon layer but the carbon layer also vary the reflected intensity ratios of *p* to *s*-polarization. The magnitude of absorption of polarized light (*p* or *s*) depends on orientation of hydrocarbon molecules adsorbed on optic surface. Depending on polarization direction and orientation of hydrogenated graphitic carbon intensity of reflected *s* or *p* component may decrease. Investigation of polarization change due to carbon contamination of optical elements was carried out by Gaupp et al.[25] at two beamlines PGM-1 and PGM-2 at BESSY II. They measured transmission spectra of horizontally (*s*) and vertically (*p*) polarized radiation. The minima observed at 284 eV and 291 eV are assigned to π^* and σ^* orbitals as C-C and C-H bonds respectively. They correlated the intensity reduction with orientation of hydrogenated graphitic carbon contaminations deposited on mirror surface. In undulator based beamlines, due to change in *p* to *s*- polarization ratio, it is difficult to find the correct undulator settings for a particular polarization state. When carbon contamination layer thickness increases with time due to prolong and continuous operation of beamline, the ratio of the transmitted vertical or horizontal polarization and their relative phases are modified by variation in carbon layer thickness, therefore periodically a tedious

polarimetry calibration of SR beam is required. When the beamline optics heavily contaminate with SR induced carbon, a strongly enhanced contribution of unpolarized light (up to 20%) due to in-homogeneities of the carbon layer over the beam footprint region on optics surface is observed [8].

1.6 Techniques for Carbon Removing from Optical Components

Deposition of carbon contaminations on optical elements cannot be avoided but its duration can be increased by decreasing hydrocarbon concentration in beamline vacuum chamber. Ohashi et al. [28] suggest that reduction of carbonaceous residue adsorbed on the surfaces in the vicinity of optical elements is the key step towards achieving a contamination free optics. Carbon contaminations on optical elements in the synchrotron radiation beamlines dramatically limit the properties of synchrotron radiation beam such as brilliance, coherence and polarization. The synchrotron radiation beam properties can be restored by refurbishing or replacing the carbon contaminated optics by fresh one. The optics used in SR beamlines requires good quality coatings on high quality substrate. These substrates and coatings are very expensive and require long preparation time, so it is better to remove carbon from contaminated optics surface using a suitable technique such as UV and plasma exposure. Several *in-situ* and *ex-situ* cleaning procedures (DC/RF plasma, plasma arc, laser, UV/O₃ etc.) have been suggested so far but several time it is observed that with these cleaning methods, either surface is not completely and uniformly cleaned or in some cases reflecting surface is damaged or modified during carbon cleaning process. In order to refurbishing the optics we have developed and optimized capacitively coupled rf plasma system, UV based *in-situ* and *ex-situ* cleaning technique and

infrared laser based cleaning technique. Detail description about development and optimization of these techniques and basic working principle of experimental techniques used in present study are given in Chapter-2.

The efficiency of cleaning strongly depends on nature of contamination layer and the technique used for cleaning. If contamination layer has diamond-like phase of carbon then it is difficult to clean due to strong bonding between carbon atoms or it may take long time for cleaning. Several studies on interaction between diamond phase of carbon and atomic oxygen suggest that diamond is more stable compared to other carbon based materials [29]–[33]. Hydrogenated amorphous carbon reactivity with energetic (2.5 eV) atomic oxygen was investigated by Bourdon et al. [29], they observed that etch rate of carbon ranging from 1 to 20 ng/cm² sec, which strongly depended on the hydrogen concentration in the film. Temperature-dependent erosion yields study on highly ordered pyrolytic graphitic (HOPG) carbon by hyperthermal atomic and molecular oxygen was carried-out by Nicholson et al. [32] they found that erosion yields vary three times by varying temperature from 298 K to 493 K and etching rate is spatially anisotropic [32]. Joshi et al. [30] studied the interaction of diamond and graphite phase of carbon with oxygen plasma and observed that sp³ hybridized carbon phase is more stable compared to sp² hybridized carbon. These studies indicate that cleaning rate strongly depends on carbon phase. As we have discussed that nature of carbon in beamlines strongly depend upon growth conditions. We have studied the nature of carbon deposited on gold coated mirror with photon dose and LiF window surface. It is observed that the nature of carbon layer vary from tetrahedral hydrogenated (ta-C:H) carbon to graphitic carbon with photon dose.

Carbon deposited on LiF window surface has both graphitic and polycrystalline diamond phases (carbonado) of carbon. Results of characterization of carbon contaminated mirror surface are discussed in chapter-3.

In case of plasma cleaning the uniformity in cleanness and surface damage can be optimize by optimizing process parameters such as power feed to plasma, pressure of process gas, exposure time and geometry of electrodes. In the last few years, at low process gas pressure radio frequency (rf) plasma glow discharge carbon cleaning technique has been considered as a cost effective, fast and suitable method for optics refurbishing. Graham, et al. [34] has used O₂ and H₂ rf plasma for removing carbon layer from Si substrate and Mo/Si multilayer mirror. Pellegrin et al. [35] removed carbon from quartz crystal surface, metallic foils used as harmonic filters and Au, Rh and Ni coated Si substrates using both capacitively and inductively coupled plasma (ICP) sources with an oxygen as process gas and they concluded that carbon cleaning rate increases by increasing rf power and oxygen gas flow rate. They also observed that rf plasma technique is suitable for removing both graphitic and diamond like carbon but they did not compared surface properties of the quartz crystal and other objects after the plasma cleaning. González et al. [36] have used ICP for cleaning of carbon and measured cleaning rates of different carbon allotropes by varying rf power and distance between the source and carbon containing object. Fernández et al. [37] have used ICP source (IBSS-GV 10X) with different combination of feedstock gases such as O₂/Ar, H₂/Ar, and pure O₂ for cleaning the carbon from boron carbide (B₄C) coated optics. They observed that pure O₂ process gas plasma only exhibits the required chemical selectivity for maintaining the integrity of the B₄C optical coating

whereas other process gases mixer change the chemical composition of B₄C film. They also concluded that the technique used for carbon cleaning by activated oxygen is not suitable for oxidizing optical surfaces such as multilayer mirrors made of W/B₄C, C/B₄C, Mo/Si etc. For oxidizing optics surfaces, hydrogen plasma is one of the alternatives to remove the carbon contamination without surface oxidation [38]. In the above discussed studies carbon was removed from small size samples in which carbon was premeditatedly deposited using different deposition techniques. The actual contamination deposited on mirror surface may have slight different characteristics in comparison to graphitic carbon, resultantly the efficiency of carbon removing may vary with applied technique. For rf plasma cleaning we have developed a in-house capacitively coupled RF plasma system and optimized it for carbon removing from optics surfaces. Using this system/technique a carbon contaminated pre-mirror (TM1) of reflectivity beamline (BL-04) of Indus-1 [26] and spherical mirror of reflectivity beamline (BL-03) of Indus-2 are refurbished. Detailed description about technique and surface characterization results of rf plasma cleaned mirror are discussed in chapter-4.

De-polymerizing of photo-resist polymer using UV light was first time reported by Bolon and Kunz [39]. Harada et al. [40] and Hansen et al. [41] used low pressure Hg lamp ($\lambda = 184.9$ and 254.7 nm) for removing carbon from grating monochromator. Several groups used zero order synchrotron radiation as UV source for carbon removing [9],[12],[41]-[42]. Hamamoto et al. [42] used 172 nm radiations and zero order synchrotron radiation as UV source for removing carbon contaminations from Mo/Si multilayer optics. They observed that both the techniques are suitable for carbon removing with certain limitations. We have also used zero order synchrotron

radiation for post mirror (TM2) cleaning of reflectivity beamline at Indus-1. During cleaning process the mirror was exposed in presence of oxygen gas pressure in $2-8 \times 10^{-6}$ mbar range with zero order synchrotron beams for approximately 40 hrs (at different ring current values). The results suggest that after carbon cleaning from mirror surface the intensity of SR beam increased by 35% near the carbon K-edge (284 eV) region [43]. We have also used 172 nm wavelength radiations emitted by Xenon excimer lamp for removing actual synchrotron radiation induced carbon contamination from mirror and grating surface. The results of UV radiation cleaning using zero order synchrotron radiation and 172 nm wavelength radiations are discussed in chapter-5.

In recent days laser surfaces cleaning seems to be one of the solution for selective material removal. The use of laser technology to remove contaminated layers from substrates using different types of lasers, coatings, and substrates have been studied [44]. The current experimental results showed that laser cleaning technique may be real substitute to mechanical and chemical techniques for selective contamination removal from large groups of materials. In laser cleaning, the material is removed by complex mechanisms namely thermal ablation, mechanical effects and combination of thermal and mechanical effect [45]. The laser cleaning mechanism strongly depends on laser beam parameters, its delivery method (pulsed or CW) and physical and chemical properties of coating material. Different organic and inorganic materials can be removed selectively using optimized laser parameters (wavelength, intensity, pulse width, pulse repetition rate and beam size) [46]. Singh et al. removed carbon from gold coated sample surface using 1064 nm wavelength nanoseconds (*ns*) pulsed laser

(Nd: YAG) and observed that at optimized parameters the gold surface did not damage [47]. We also customized an Yb:YAG fiber laser system for cleaning of carbon contamination from synchrotron optics. Before cleaning the actual optics the system is optimized using carbon coated gold thin film surfaces at different laser parameters. At optimized parameters carbon from gold surface is removed and the sample is characterized using different surface analysis techniques. Finally the results of cleaning of carbon from gold surfaces are compared with other rf plasma and UV cleaned surfaces. The results of comparison of cleaning using three cleaning techniques are discussed in chapter-6.

1.7 Scope of Present Work

The structure of carbon layer deposited on optical elements in beamlines varies from hydrogenated amorphous carbon to diamond-like carbon (DLC) depending on deposition parameters such as photon dose and partial gas pressure. The denser structure of DLC film leads to more absorption for soft x-ray photons in comparison to that of less dense carbon layer. DLC films are likely to show more resistance to cleaning process because of strong binding of carbon atoms. Carbon layer deposited on optical elements reduced the SR beam intensity by creating different effects such as absorption, scattering and interference etc. The intensity of SR beam can be regained by removing the carbon layer. A systematic study on the growth characteristics of SR induced carbon layer will help in identifying the phase of carbon in the contamination layer and in turn will help in choosing appropriate cleaning methods for the removal of contamination layer. In Indus synchrotron sources (Indus-1 and Indus-2) more than 20 beamlines are in operation and each beamline has minimum three optical

components. So there is a strong need for development of suitable cleaning techniques to refurbish optical elements as and when it is required. During the course of present thesis work, in-situ and ex-situ synchrotron optics refurbishing techniques are setup and optimized for optics refurbishing. The developed techniques/ processes are applied on actual optical elements to regain their performances by removing the carbon contamination layer. The thesis covers detail study on growth characteristics of SR induced carbon layer and development of three independent setups based on RF plasma, UV and Laser technique and their successful employment for cleaning of actual optics of Indus beamlines.

2 Optics Refurbishing Setups and Experimental Techniques

2.1 Overview

This chapter covers design, development and optimization of optics refurbishing setups (capacitive coupled rf plasma system, *in-situ* and *ex-situ* UV cleaning system and IR laser system) and basic principle of experimental techniques (Soft x-ray reflectivity, X-ray photoelectron spectroscopy, Raman spectroscopy and Atomic force microscopy) used in present study.

2.2 Optics Refurbishing Setups

2.2.1 Inductively Coupled RF Plasma Source

Various plasma discharge techniques in different geometry are commonly used for surface treatments such as sputtering, etching etc. The selection of the technique depends on nature of surface treatment required.

Inductively and capacitively coupled plasma both are glow discharges produced by rf sources and are used for surface cleaning applications. Inductively coupled plasma (ICP) is excited by time varying magnetic field produced by rf current flowing in a current conducting induction coil. Typically the frequency used for plasma generation is 13.56 or 27.12 MHz. The time varying magnetic field induces electric field, which generate and sustain plasma in vacuum chamber. ICP sources are usually operated at lower pressure, thus at lower pressure rf plasma is strongly non- equilibrium and cold. Different antenna's geometries (cylindrical, planar and half-toroidal) are used to

produce ICP. The power is delivered in terms of electromagnetic waves by an rf power source through a matching box inserted between the power source and antenna. Most of the power is coupled to electrons in gas filled chamber other particles are too heavy to respond to the rf field. The ICP plasma source gives high plasma density in localized region which affect the uniformity of surface cleaning. In order to avoid non-uniform cleaning commercially available inductively coupled rf source (GV10X, ibss) is used as a downstream asher by several groups for surface treatment applications [36], [37], [48]. Downstream asher rf plasma source produce plasma in a separate volume upstream the chamber with the object to be cleaned. This allows for an operation of the plasma chamber at higher pressure (10^{-1} to 10^{-3} mbar) with the cleaning chamber at lower pressure. Schematic diagram of downstream ICP source used for synchrotron optics is shown in Figure 2.1.

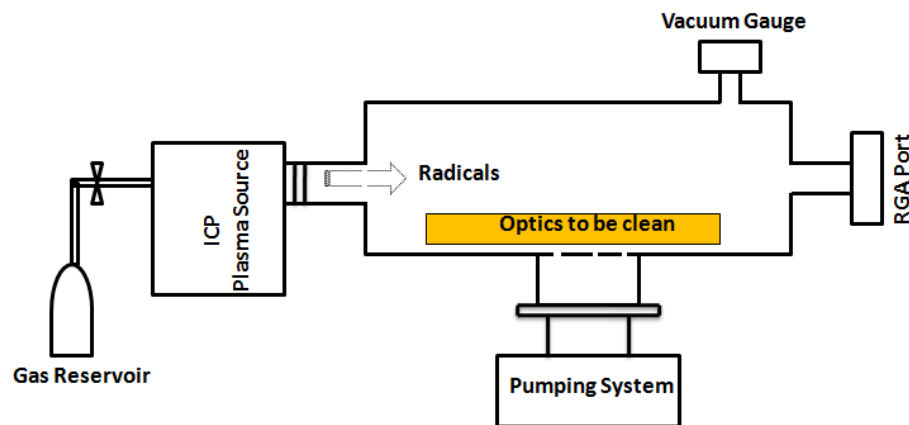


Figure 2.1: Schematic diagram for optics cleaning using inductively coupled plasma source.

Geometry of Capacitively coupled plasma (CCP) is simple in which plasma is excited by applying rf voltage between two parallel electrodes. With previous experience of capacitive coupled plasma (CCP) system for carbon removal from Au and Pt sample

surfaces in present study we have used CCP source (detail is given in section 2.2.2). Due to simple geometry the large size optics can be easily accommodates between parallel plates electrodes.

2.2.2 Capacitive Coupled RF Plasma Cleaning Setup

For the application of x-ray optics refurbishing we have developed a capacitively coupled rf plasma system. The system description and optimization of the parameters for carbon cleaning are discussed below.

2.2.2.1 Electrode Assembly and Vacuum Chamber

The capacitively coupled rf plasma system is designed for removing carbon from x-ray optics surfaces. The system can accommodate the optics of the size of 350 mm × 60 mm × 40 mm. For the vacuum chamber SS304 material was selected because specific outgassing of SS304 is of the order of 10^{-12} mbar liter/sec.cm². The vacuum chamber is cylindrical in shape with dimensions 450 mm height and 400 mm diameter. Different size ports are provided for mounting vacuum pump, pressure gauge and viewing window. For vacuum generation a turbomolecular pump of 250 liter/sec pumping capacity with a dry backing pump is used to obtain vacuum in $\sim 10^{-7}$ mbar range. For pressure measurement a full range vacuum gauge is used. For gas injection a 0 to 30 sccm flow rate mass flow controller is used. The required process gas pressure in the chamber can be achieved by adjusting gas flow rate (gas inlet) and the pumping port valve (gas outlet). The viewing quartz window is mounted in such a way that the optics to be clean can easily seen during plasma exposure. An optical emission spectrometer (OES) is also used for monitoring optical emission lines from plasma.

The material and the relative ratio of electrode area have special importance in rf plasma systems. The electrode material should be good conductor of electricity and heat so that localized heating and unwanted impedance of circuit can be avoided. For plasma generation two aluminum metal electrodes (parallel plates) of dimension $150\text{ mm} \times 75\text{ mm} \times 5\text{ mm}$ are used. In order to isolate the electrode from rest of the chamber, the electrodes are mounted on one end of rectangular teflon rod and second end of the rod is mounted on a base plate for vertical mounting. The base plate has rectangular grooves by which the separation between parallel plates (electrodes) can be adjusted. Both the electrodes are perfectly isolated from rest of the vacuum chamber. The schematic diagram of the electrode assembly is shown in Figure 2.2.

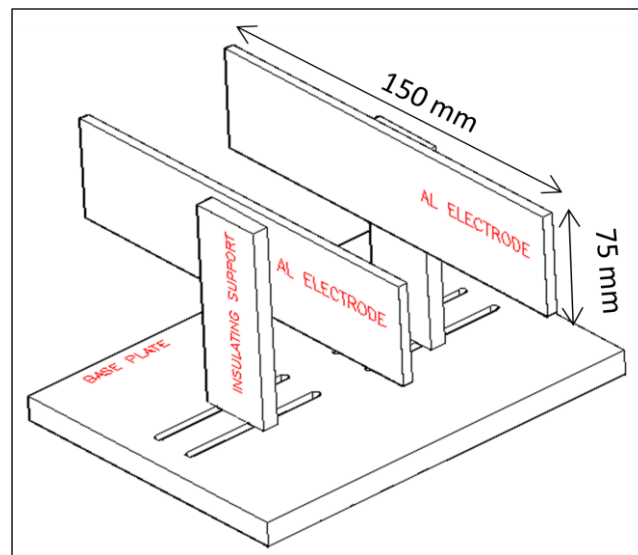


Figure 2.2: Schematic diagram of symmetric electrode assembly used for generating capacitively coupled rf plasma.

The rf power at 13.56 MHz frequency is feed to the one of the electrode and the second electrode is kept at the ground potential. The distance between power and ground electrode can be vary according to the size of optics to be clean. For

impedance matching an automatic tuning network between rf amplifier and electrode assembly is used. The schematic diagram of the plasma cleaning system is shown in Figure 2.3.

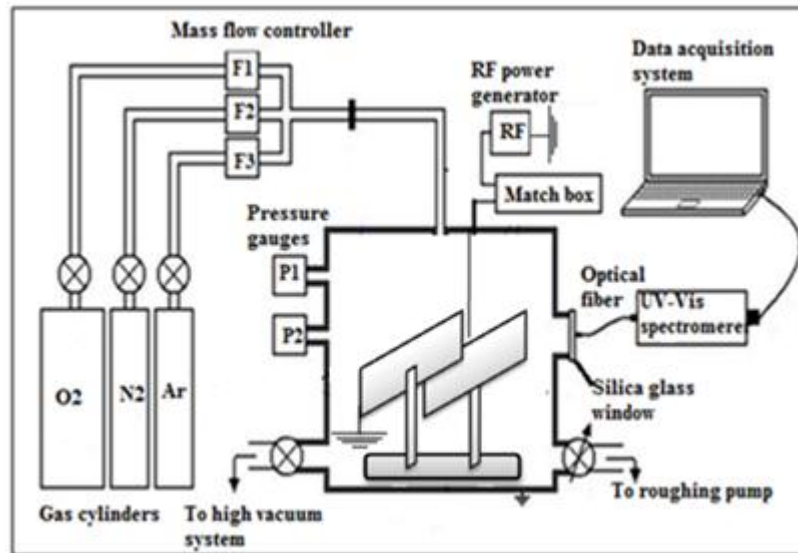


Figure 2.3: In-house developed capacitively coupled rf (13.56 MHz) plasma cleaning system.

2.2.2.2 Importance of rf Frequency

To sustain a discharge in capacitively coupled rf plasma systems, frequency, gas pressure and power are important parameters and these parameters are correlated to each other. Radio frequencies lies in 30 Hz to 300 GHz range but all frequencies are not suitable for plasma generation. In plasma at low frequencies electrons and ions both are able to respond the applied field and they hit the chamber wall and they lost from system, resultantly plasma discharge cannot be sustained in low frequency region. On the other hand in high frequency regime the response of ions to the applied field is very sluggish, consequently ion current to cathode and secondary electrons production decreases. To compensate the reduced secondary electron production at

higher frequencies the breakdown field has to rise. The absorption of power and amplitude of electrons and ions oscillations is strongly depend on applied rf frequency and molecule/atom collision frequency. The absorbed power (P_{abs}) and amplitude ($x_{i,e}$) of oscillation of ions or electrons are given by [49]

$$P_{abs} = \frac{e^2 \nu E^2}{2m_e (\omega^2 + \nu^2)} \quad (2.1)$$

$$x_{i,e} = \frac{eE}{m_{i,e} \omega \sqrt{\omega^2 + \nu^2}} \quad (2.2)$$

Where $x_{i,e}$, and $m_{i,e}$ are amplitude and mass of ion or electron respectively, ω – frequency of applied field E , ν – collision frequency of electrons or ions and e - is charge of electron.

In low pressures regime ($\nu \ll \omega$), the number of collisions between gas molecules and electrodes are very less resultant many cycles of the wave have to go before a collision to occurs between molecules. Due to fewer collisions (ionizations) the power absorption from source is not sufficient for sustaining plasma discharge. At low pressure to sustain plasma the field strength again has to rises. On the other hand in high pressure regime ($\nu \gg \omega$) within single wave period large number of molecular collisions take place, so that the electrons are unable to build-up their steady-state oscillation thus to sustain plasma in high pressure regime electric field strength again has to rises. We thus see that the breakdown field has to raise both in the high and low-pressure regimes to sustain plasma. In capacitively coupled rf discharges frequency range is lies between 1 to 100 MHz. For plasma generation in 10^{-2} mbar pressure region, we used a 13.56 MHz rf generator with impedance matching network.

At 10 watt power ($V_{pp}= 170$ volt) and 5×10^{-2} mbar pressure the amplitude of oscillation of electrons and ions are ~ 3 mm and ~ 1 μ m respectively that is well below the separation distance (70 mm) of rf electrodes and chamber dimensions.

2.2.2.3 Effect of Electrodes Dimensions

In rf plasma discharges the self biased voltage (V_{sb}) developed on powered electrodes is strongly depends upon dimensions of electrodes $V_1/V_2 = (A_2/A_1)^\alpha$ [50] and the process parameters such as applied power, gas pressure and type of gas. In conventional rf plasma systems (asymmetric configuration) the powered electrode is smaller than the ground electrode (shown in Figure 2.4a). The sheath capacitance ($C = \epsilon A/d$) near electrodes surface is proportional to the area of electrode and the voltage developed on electrodes is inversely proportional to the sheath capacitance ($V = Q/C$), where ϵ and d are dielectric constant and thickness of sheath region and A is area of electrode. Resultant self bias voltage (V_{sb}) developed at large size electrode will be less compared to smaller electrode. So, in asymmetric configuration the self biased voltage developed across small size electrode will be much large compare to large size or ground electrode. Due to this bias voltage ions gain energy in the system and sputtered the powered electrode material. For carbon cleaning applications especially for x-ray optics surface where surface / interface roughnesses are important parameter and it should remain less than 5 Å. The sputtering of electrode material by ion bombardment may contaminate the optics surface or lead to increase in surface roughness. In order to avoid such situations symmetric configuration assembly of electrodes was chosen, in which both electrodes have same dimensions resultantly the V_{sb} on electrodes is less than the plasma potential (10-20V)

in the system. In this type of systems maximum energy gain by ions in the system is of the order of 10 eV to 20 eV. Schematic diagrams representing self bias voltage (V_{sb}) in asymmetric and symmetric configurations are shown in Figure 2.4. That is less than the threshold value for sputtering of any material. The energy gain by ions due to instantaneous rf voltage is not too much because polarity of field changes with applied rf frequency.

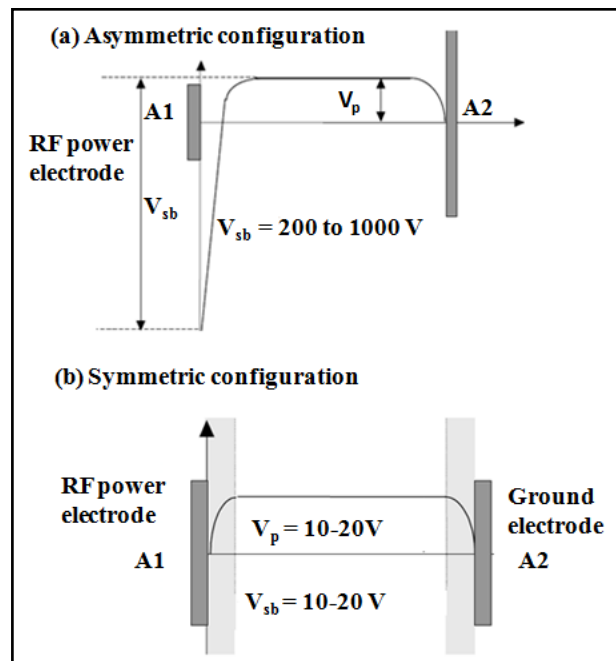


Figure 2.4: Schematic representation of self bias voltage (V_{sb}) developed on powered electrode (a) Asymmetric configuration (b) Symmetric configuration

The self bias voltage developed on the electrodes also depends on gas pressure, applied power and the frequency of the field. All these parameters affect electron/ions oscillation amplitude and power absorption in the system. For carbon cleaning application the self bias voltage should be below the threshold value of sputtering of any material. Here by varying power and the gas pressure in the system the self bias voltage is set at minimum value. The self bias voltage at 10 watt power by varying

oxygen gas pressure from 1 mbar to 1×10^{-3} mbar and by varying applied power from 1 to 20 watt at 5×10^{-2} mbar pressure is measured. The measured self biased voltages are shown in Figure 2.5.

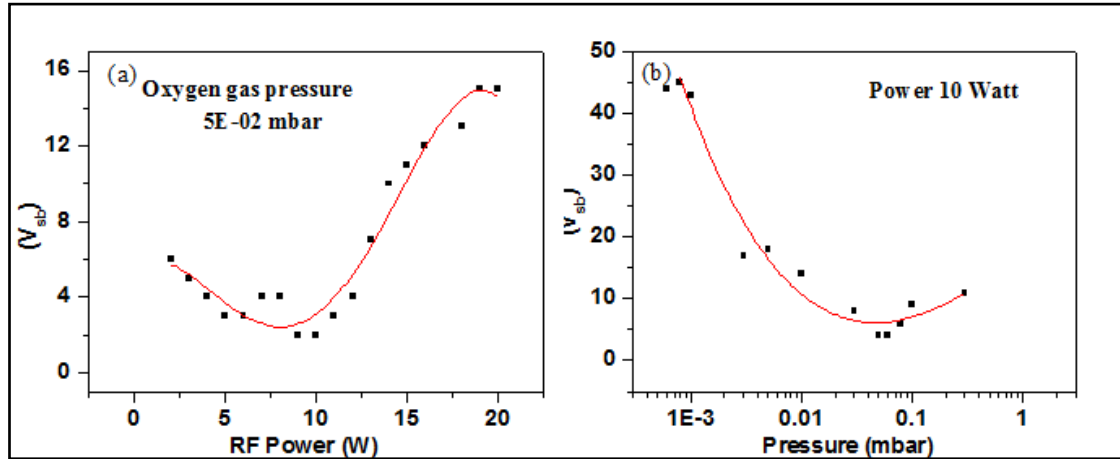


Figure 2.5: Self bias voltages (V_{sb}) on power electrode (a) by varying applied RF power (b) by varying oxygen gas pressure.

From plots of Figure 2.5a it is observed that at constant oxygen pressure ($\sim 5 \times 10^{-2}$ mbar) the self bias voltage vary from 6 V to 15 V with a variation of rf power from 1 watt to 20 watt and the minima value of self bias voltage (2 V) is at 10 watt, Figure 2.5b shows variation in self bias voltage with oxygen gas pressure at constant power. The plots indicate that in $4-6 \times 10^{-2}$ mbar pressure the self bias voltage is at minimum value (5 V). These values of pressure and applied power values are selected for carbon cleaning experiments.

2.2.2.4 Optimization of rf Power and Exposure Time

In order to see the effect of exposure time and rf power on optic surface, carbon coated Pt thin film surfaces (Si-substrate/Pt-500Å/C-300Å) are exposed to oxygen gas plasma at constant power (10 W) for 10, 20 and 30 minutes. After plasma exposure

the hard x-ray reflectivity of the sample surfaces are compared with pristine Pt thin film surface reflectivity of same thickness. Figure 2.6a show x-ray reflectivity versus momentum transfer (q_z) curves of carbon cleaned Pt thin film surface at three different exposure times and pristine Pt thin film surface. Details of x-ray reflectivity dependence upon momentum transfer vector given in section - 2.3.1. The reflectivity graphs clearly reveals that the reflectivity of sample exposed for 30 minutes is closely matches with the reflectivity of the pristine Pt sample reflectivity.

For rf power optimization similar samples (Si-substrate/Pt-500Å/C-300Å) are exposed at 5, 10 and 20 watt power for 30 minutes. After plasma exposure the x-ray reflectivity of the sample surfaces are compared with pristine Pt thin film surface of same thickness. Figure 2.6b show x-ray reflectivity versus momentum transfer (q_z) curves of pristine Pt and after carbon removal at three different power levels. The reflectivity graphs clearly reveal that the reflectivity of sample exposed at 10 watt power closely matches with the reflectivity of the pristine Pt sample reflectivity. These results reveal that 10 watt rf power and $4-6 \times 10^{-2}$ mbar pressure is sufficient for carbon cleaning application. At these parameters (10 watt and $4-6 \times 10^{-2}$ mbar) the carbon cleaning rate ~ 10 Å per minute was observed.

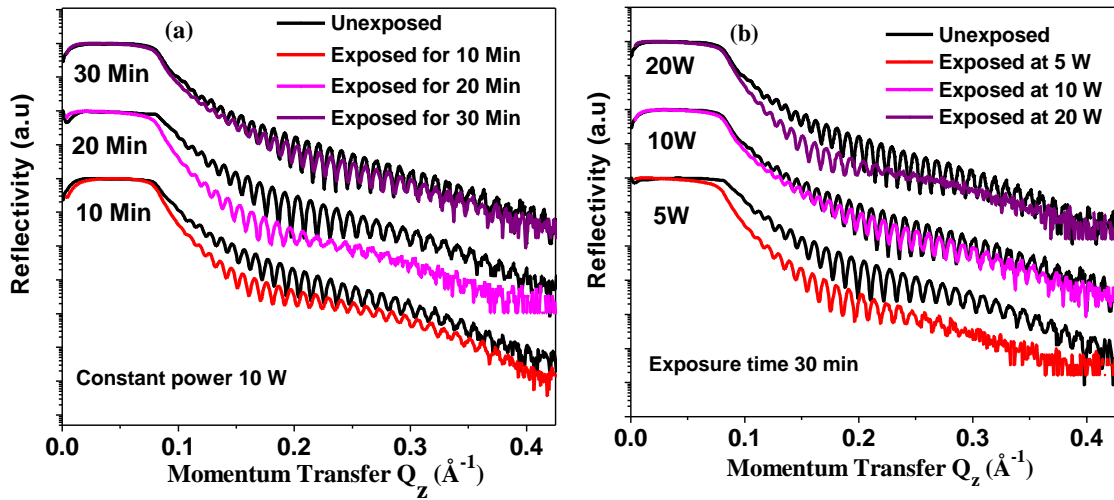


Figure 2.6: X-ray reflectivity of Pt surface before and after plasma exposure (a) Different exposure time at 10 watts power (b) Different power at 30 minutes exposure time.

In order to see surface contamination of electrode material after cleaning on optics surface, a carbon coated Au thin film sample (Si-substrate/Au-730Å/C-180Å) was also exposed to rf plasma at same experimental parameters. After plasma exposure at 10 W rf power and 5×10^{-2} mbar oxygen pressure for 20 minutes the sample was analyzed by X-ray photoelectron spectroscopy (XPS) measurement and compared with XPS spectrum of pristine Au sample. Figure 2.7 shows XPS spectrum of pristine Au and after carbon cleaning from Au surface. The XPS spectrum show different peaks of Au with C (1s) and O (1s) peak in both the samples no other peaks are observed after plasma exposure. These observations reveal that at these parameters the electrode and chamber material is not sputter and not deposited on sample surface.

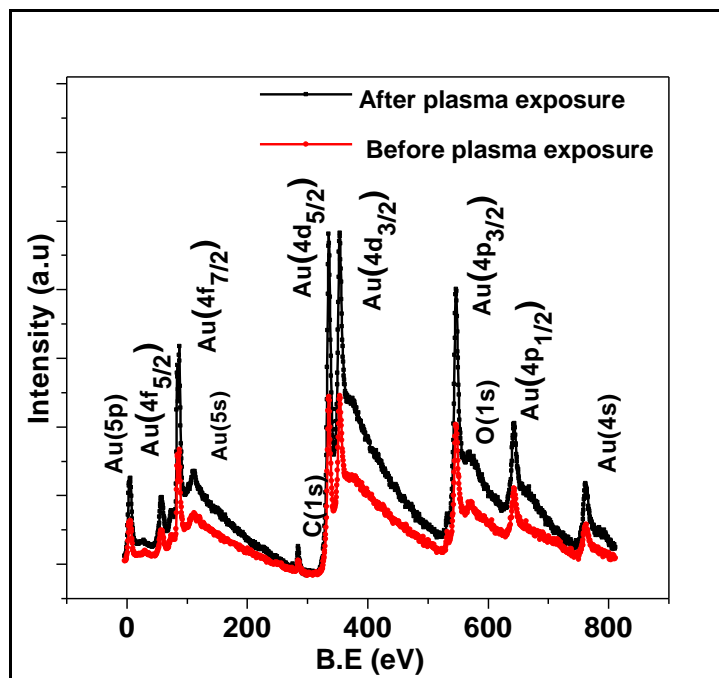


Figure 2.7: X-ray photoelectron spectra of Au surface before and after plasma exposure at 10 W rf power and at 5×10^{-2} mbar oxygen pressure for 20 minutes of exposure.

2.2.3 UV Cleaning Setup

Ultra violet (UV) radiations are part of electromagnetic radiations, which typically cover energy range from 3.1 to 31 eV and are suitable for breaking the hydrocarbon bonds. Dissociation of hydrocarbon and oxygen molecules easily occurs by Ultra violet radiation. In the present work both *in-situ* and *ex-situ* carbon cleaning techniques with UV sources are used for optics refurbishing. In *in-situ* cleaning technique zero order synchrotron radiation is used as UV source at reflectivity beamline of Indus-1, where zero order beam covers significant portion of UV photons. On the other hand for *ex-situ* cleaning, a 172 nm wavelength Xenon excimer lamp (EX-mini L12530-01, Make: Hamamatsu) in ambient environment is used as UV source. Here *in-situ* and *ex-situ* optics cleaning setups are discussed.

2.2.3.1 Description of In-situ Cleaning at Reflectivity Beamline of Indus-1

Brief description of Reflectivity beamline: In-situ cleaning of toroidal mirror (TM2) of reflectivity beamline (BL-04) at Indus-1 was carried out with zero order synchrotron radiation in presence of O₂ gas environment. The reflectivity beamline at Indus-1 synchrotron radiation source is installed on a 50 degree port of the bending magnet (BM-2). The toroidal shape pre mirror (TM1) is mounted at 4.5 degree from horizontal plane which accept 10 mrad × 5.9 mrad (H×V) synchrotron radiations beam from source. The beamline covers 10 eV to 300 eV energy range. The whole beamline is subdivided into five major sections. Pre mirror sections, Monochromator section, Post mirror section, Differential pumping section and the Experimental station. All the sections except experimental station are maintained under ultra high vacuum by the use of sputter ion pumps. The toroidal grating monochromator (TGM) section comprised of two slits assemblies (S1 at focus point of TM1 and S2 at focus point of TGM). The differential pumping section is used to connect high vacuum reflectometer operating in 10⁻⁷ mbar region with beamline operating in UHV environment by maintaining a pressure difference of two orders (10⁻⁹ to 10⁻⁷ mbar). In post mirror section TM2 is also mounted at 4.5 degree which accepts photon beam from monochromator and focus it at experimental station. The experimental station is equipped with two axes (θ-2θ) high vacuum compatible goniometer. Silicon photo diode detector (AXUV100G: IRD) is used for photon beam intensity measurement. Mechanical layout of reflectivity beamline with different sections is shown in Figure 2.8. In order to carry out in-situ carbon cleaning experiment on TM2 additional gas inlet line with regulated gas supply and vacuum pump was installed in post mirror

section. Schematic diagram of post mirror section with regulated gas supply and orifice positions are shown in Figure 2.9.

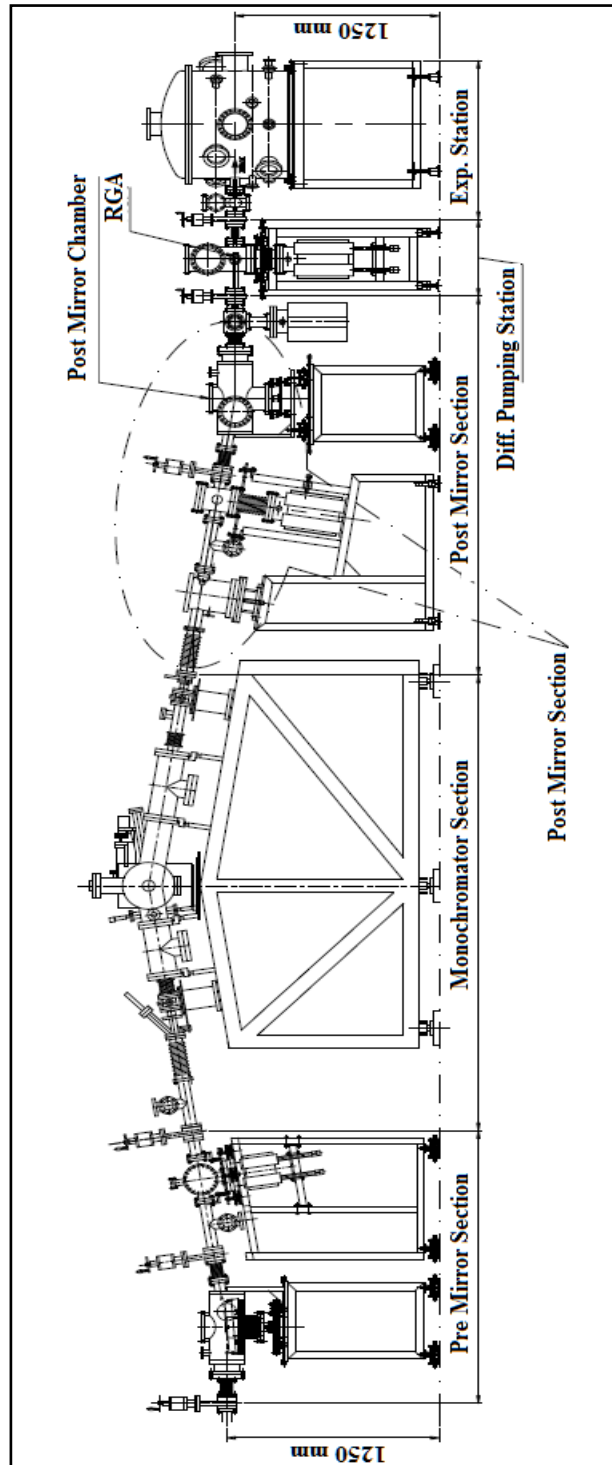


Figure 2.8: Mechanical layout of reflectivity beamline (BL-04) at Indus-1 SR source

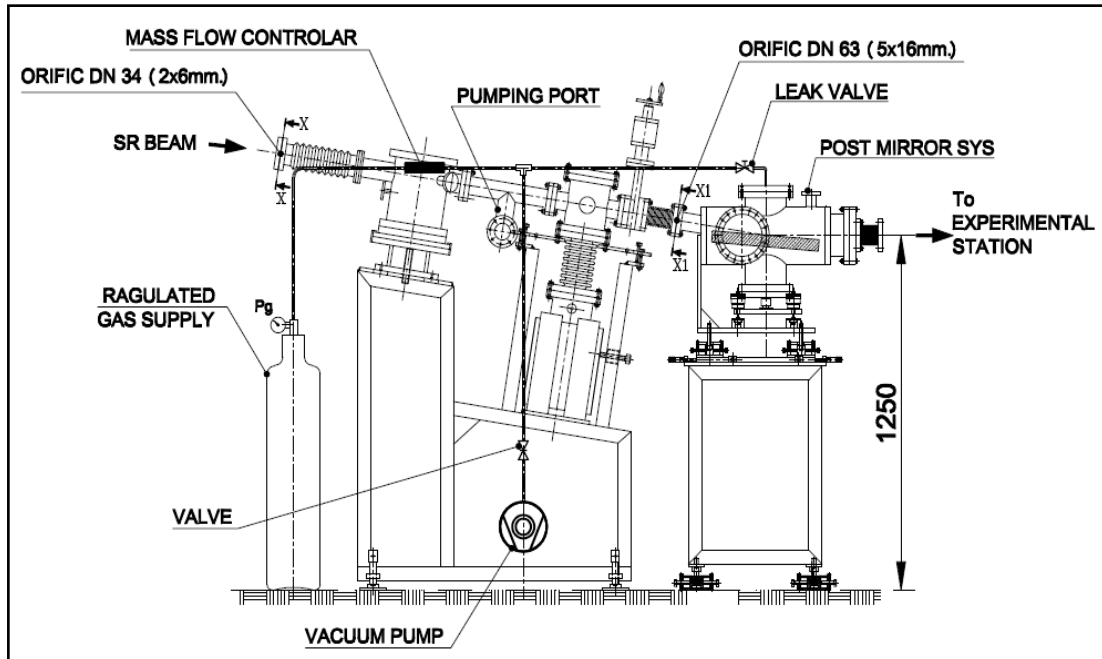


Figure 2.9: Schematic diagram of post mirror section with gas inlet system for *in-situ* cleaning of post mirror (TM2) at reflectivity beamline of Indus-1.

Pressurizing post mirror section for *in-situ* cleaning experiment: The basic requirement of *in-situ* cleaning is a high oxygen gas pressure (10^{-4} to 10^{-6} mbar) in presence of zero order synchrotron radiation in the vicinity of optics to be clean. To maintain high pressure in a localized region of beamline in presence of SR beam is a challenging task. The oxygen gas was introduced in post mirror section to raise pressure in 10^{-6} mbar region by gas inlet system which consists of regulated gas supply, mass flow controller and leak valve. In order to restrict the pressure buildup in rest of the sections of beamline, two orifices are designed in such a way that they allow SR beam without affecting intensity of the beam with a minimum pressure change in rest of the beamline. The size of orifices aperture are decided by beam size near the exit slit (S2) and just before the entrance of post mirror chamber as indicated in Figure 2.9. The orifice mounted near S2 has $2 \times 6 \text{ mm}^2$ size aperture with gas

conductance of 1.4 liter/sec, which gives a gas load order of 10^{-7} mbar liter/sec at pressure of 10^{-7} mbar in monochromator section, this gas load is well compensated by sputter ion pumps installed in this section. The orifice mounted near entrance of post mirror chamber has $6 \times 16 \text{ mm}^2$ size aperture with conductance of 11 liter/sec, which gives a leak rate of the order of 10^{-6} mbar liter/sec at pressure of 10^{-6} mbar in the section between post mirror and exit slit (S2). In this section to maintain additional gas load, a turbo-molecular pump with effective pumping speed of 15 liter/sec was mounted. In order to avoid any risk, vacuum safety interlock scheme was implemented in which monochromator vacuum gauge was interlocked with gate valve (GV1) (GV1 is an isolation valve that separates storage ring to beamline). After raising oxygen pressure in $2-8 \times 10^{-6}$ mbar range the TM2 was exposed by zero order synchrotron radiations in four steps at different ring current values for ~ 40 hrs. The detail process of cleaning mechanism and their results are discussed in chapter-5.

2.2.3.2 Xenon Excimer UV Radiation Setup for Carbon Cleaning

Low pressure mercury lamp gives a discrete energy spectrum in which radiations of wavelengths below 253.7 nm are useful for carbon removal. Radiations of wavelengths 253.7 nm break the bonds of organic molecules and 184.9 nm wavelength radiations dissociate the oxygen molecule into oxygen radicals. Oxygen radicals combines with molecular oxygen O_2 and produce ozone (O_3) gas [51]. Ozone has large absorption cross section at 253.7 nm. Absorption of 253.7 nm wavelength by O_3 reduces its intensity, resultant cracking of contaminant molecule decrease consequently cleaning efficiency decrease [52]. For avoiding such limitations, we have selected a Xenon excimer lamp that emits 172 nm wavelength radiations.

Radiations of wavelength 172 nm (~ 7.2 eV) dissociate both organic molecule as well as oxygen molecule simultaneously [53]. The carbon cleaning mechanism using UV radiations is discussed in chapter-5. The Xenon excimer lamp setup used for removing carbon contamination is shown in Figure 2.10. The lamp gives 172 nm wavelength radiations with spectral half width of 17 nm. The intensity of lamp at the surface of lamp in $75 \text{ mm} \times 30 \text{ mm}$ area is 50 mW/cm^2 . In order to avoid any health hazards by O_3 production, the system is equipped with an O_3 decomposer unit which reduces the O_3 spread in the surrounding environment.

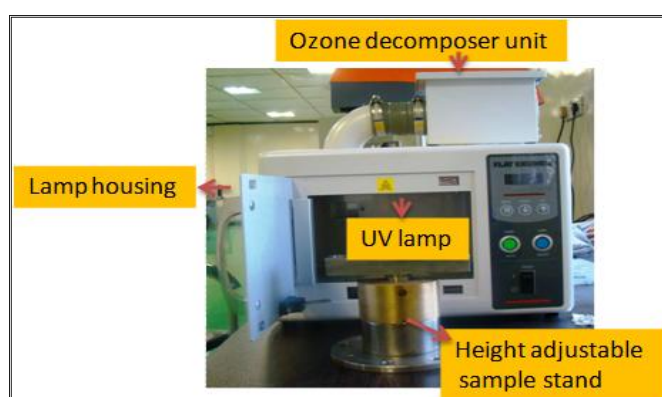


Figure 2.10: Xenon lamp (EX-mini L12530-01) used for cleaning of mirror and grating.

In order to see the carbon cleaning efficiency of excimer UV source, carbon coated Pt thin film samples ($\text{Pt/C-280\text{\AA}}$) were exposed for 2 hrs, 4 hrs, 6 hrs, 10 hrs and 12 hrs. During exposure sample was kept at minimum allowable distance of ~ 5 mm from source. At 5 mm distance UV radiation intensity reduced to $\sim 22\%$ of the intensity at the surface of lamp (the extinction coefficient for 172 nm wavelength is $0.3/\text{mm}$ at 1 atm pressure in air [52]). So it is expected that at 5 mm distance the UV radiation

intensity is about 11 mW/cm^2 . The confocal microscopic surface images ($355 \mu\text{m} \times 473 \mu\text{m}$) of exposed samples (shown in Figure 2.11) are compared with the pristine Pt thin film surface image. The carbon removal rate was estimated by soft x-ray ($\lambda = 80 \text{ \AA}$) reflectivity measurements (measured and fitted reflectivity spectra are shown in Figure 2.12 of 6 hrs and 12 hrs exposed samples and from reflectivity data fittings it is observed that after 12 hrs of UV exposure at $\sim 5 \text{ mm}$ distance from source 280 \AA carbon layer completely removes with a rate of $\sim 24 \text{ \AA/hr}$ and soft x-ray reflectivity of UV radiation exposed sample surface well matches with pristine Pt surface reflectivity. Thickness and roughness of Pt and C layer before and after carbon removal is tabulated in table-2.1.

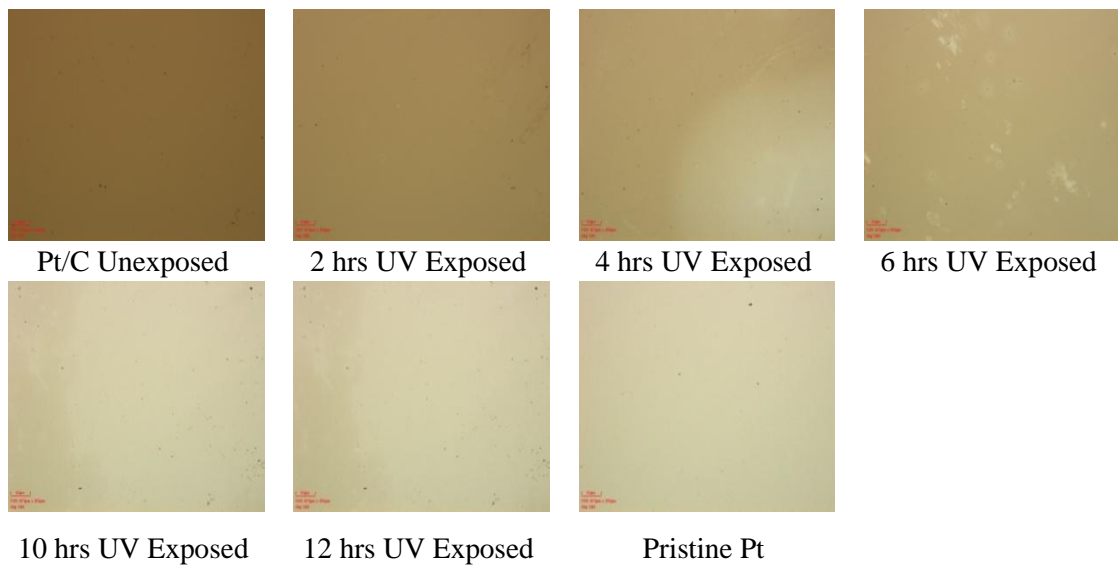


Figure 2.11: Confocal microscopy images ($355 \mu\text{m} \times 473 \mu\text{m}$) of Pt/C samples after different exposure time by excimer UV radiations at 5 mm distance from source.

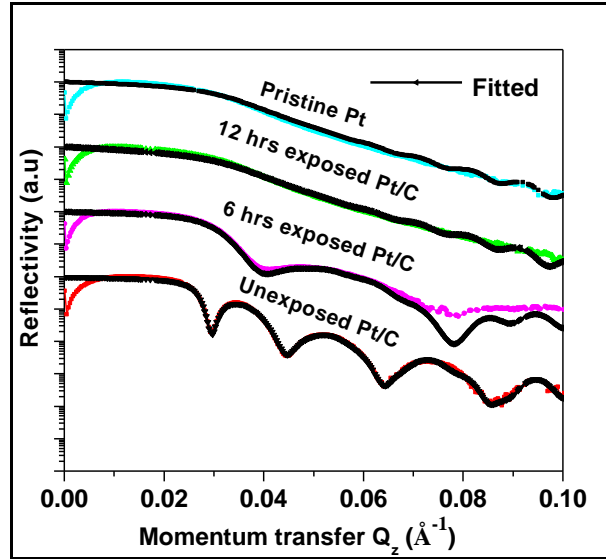


Figure 2.12: Soft x-ray reflectivity of Pt/C samples after different exposure time by UV radiations at 5 mm distance from source.

Table-2.1 Structural parameters (thickness (t), roughness (σ)) of Pt/C sample determined by soft x-ray reflectivity curves fitting after different time of UV exposure.

Sample	Pt layer		C layer		Ambient layer	
	t (Å)	σ (Å)	t (Å)	σ (Å)	t (Å)	σ (Å)
Pt/C	531	10.7	280	12.3	---	---
Pt/C 6 hrs exposed	530	10.7	140	12.2	---	---
Pt/C 12 hrs exposed	530	10.7	---	---	32	12.8
Pt	531	10.7	---	---	32	12.8

2.2.4 IR Laser Cleaning Setup

For carbon cleaning applications an infrared (IR) laser based system is customized as per requirement of carbon cleaning applications from optics surfaces. The system consist of nanosecond (ns) pulsed Yb:YAG fiber laser ($\lambda=1064$ nm) which give variable power in 0 to 30 watts, galvanometer based laser beam scanner, F-theta lens and a motorized Z-stage for vertical movement of scanner for adjusting beam focus on sample surface. The system is fully controlled by computer software program. Descriptions of subcomponents of the laser system are given below.

Fiber Laser: The fiber laser configuration is shown in Figure 2.13. The laser cavity is formed by inter core fiber Bragg grating (FBG) and combined pumps are launched through FBG into both ends of the Yb doped fiber (YDF). The one end FBG is highly reflecting (HR) for lased wavelength (1064 nm) and at second end FBG is low reflecting (LR) which passes the lased wavelength. The maximum laser power is 30 watts. The laser pulse frequency can be varied from 20 to 200 kHz using Q-switching method and it emits laser pulses in hundreds of nanosecond range.

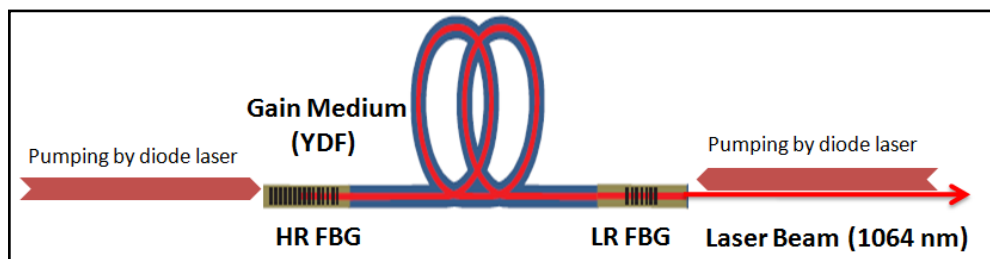


Figure 2.13: Yb:YAG fiber laser configuration, showing cavity formed by inter core fiber Bragg gratings.

Scanner: The system used a 2D galvanometer scanner for scanning the laser beam on the sample surface in x-y plane. The deflection in laser beam is performed by galvanometer drives for deriving mirrors. The scanner can move the both mirrors in $\pm 6.5^\circ$ resultant the focused laser beam can scan 160 mm distance in both x- and y-directions. The scan speed can be varied from 0.1 to 10 m/sec. with the help of x- and y-galvanometer drivers. The schematic of assembly of customized laser system with beam collimator, galvanometer drives and F-Theta lens are shown Figure 2.14.

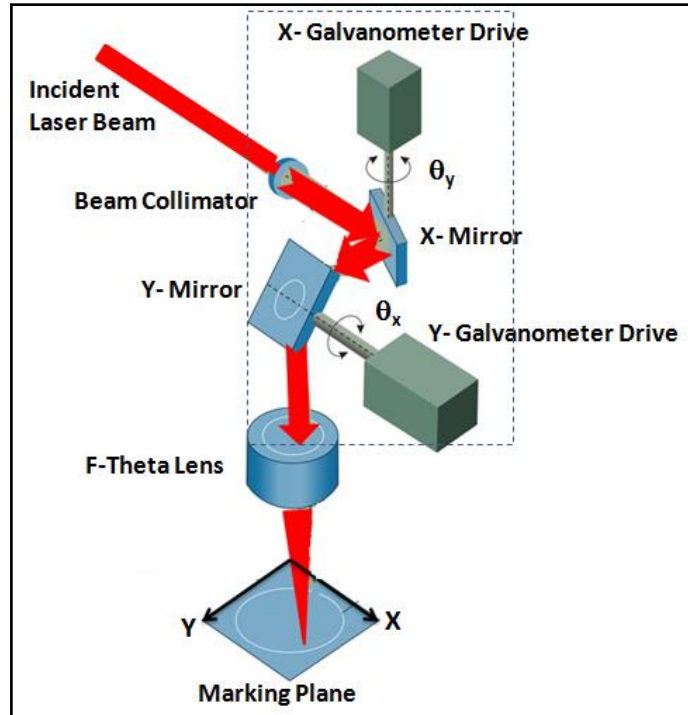


Figure 2.14: Schematic diagram of laser beam steering with x- and y-galvanometer mirror drives.

F-Theta Lens: The F-theta lens [make: JENOPTIK Optical Systems GmbH] is used for focusing the laser beam in x-y plane. F-theta lens are designed with a barrel distortion that yields the output beam displacement, that is linear with the product of f and θ ($f * \theta$), where θ is the angle of incidence of the input beam. The focal length (f) of lens is 255 mm and the maximum scan angle that can be covered by the lens is $\pm 18^\circ$, which gives a flat field in a circular area of 160 mm diameter. The lens can accept a laser beam of diameter 20 mm and after focusing the minimum beam diameter at focus point is $\sim 150 \mu\text{m}$. The focal plane position can be moved up and down (movement in vertical direction) with the help of motorized Z-stage.

2.2.4.1 Optimization of Laser System for Carbon Cleaning

For selective material removal using nanosecond pulsed IR laser, at constant pulse width there are two important parameters that affect the laser cleaning, the first one is fluence (energy/area) of laser beam on sample surface and second one is the overlapping of laser beam spots. At constant power the fluence value strongly depends on laser beam spot area. In focal plane the laser beam is strongly focused and has minimum beam diameter resultant laser fluence value is maximum in focal plane. For surface cleaning applications the sample should not kept at the focal plane otherwise the laser beam damage the sample surface. The laser spot diameter increases in beam propagation direction (above and below the focal plane) with relation $d_z = d_0 \sqrt{1 + z/z_R}$, where d_0 and d_z are beam diameter at focus plane and at z distance from the focus plane respectively and z_R is known as Rayleigh range of laser and given by $Z_R = \pi \cdot d_0^2 / \lambda$. The laser beam spot diameter also varies with pulse frequency, laser beam scan speed and laser power. So before using the IR laser for carbon cleaning the beam spot diameter was measured at 5.5 mm above the focal plane by marking the laser beam on a dye coated Aluminum (Al) sheet by varying laser power, frequency and the laser scan speed. Using these beam spot diameter values, fluence values on sample surface and overlapping (D), $D = \left(1 - \frac{v}{s \cdot f}\right)$ (where v is scan speed, S is spot diameter, and f is pulse frequency) of beam spot diameter are calculated and plotted in Figure 2.15. Overlapping of laser beam spots also increases the effective power deposition on sample surface.

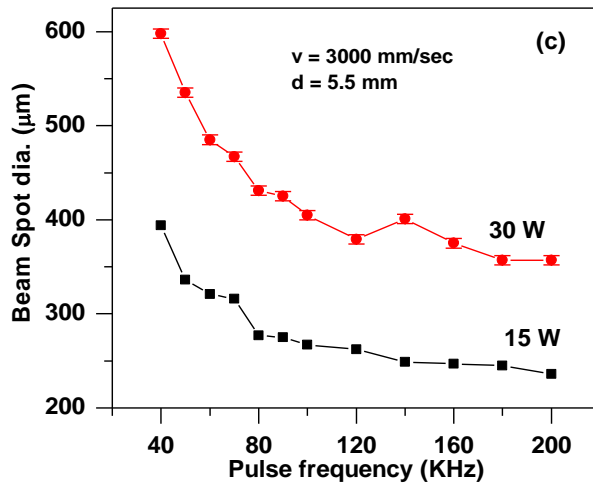
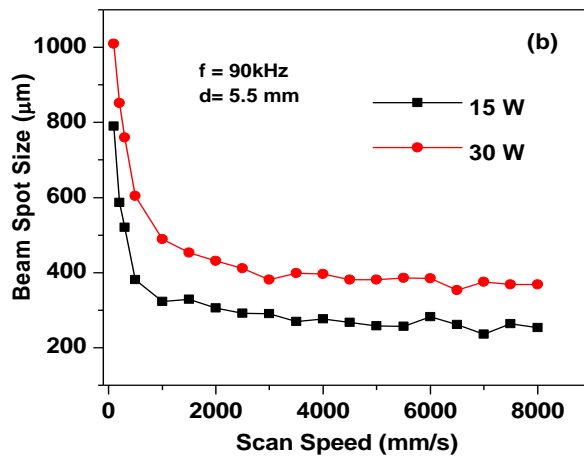
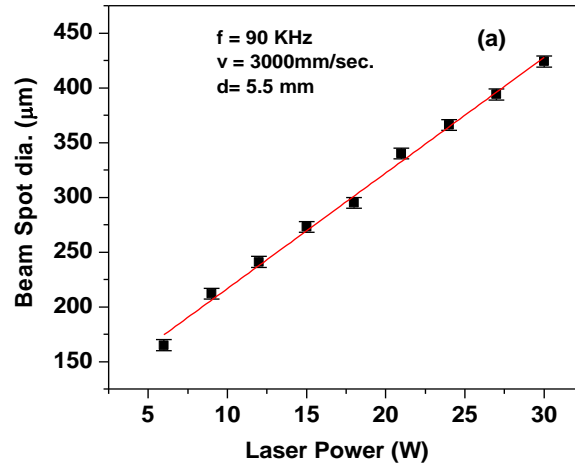


Figure 2.15: Laser beam spot diameter with (a) laser power (b) scan speed and (c) pulse frequency.

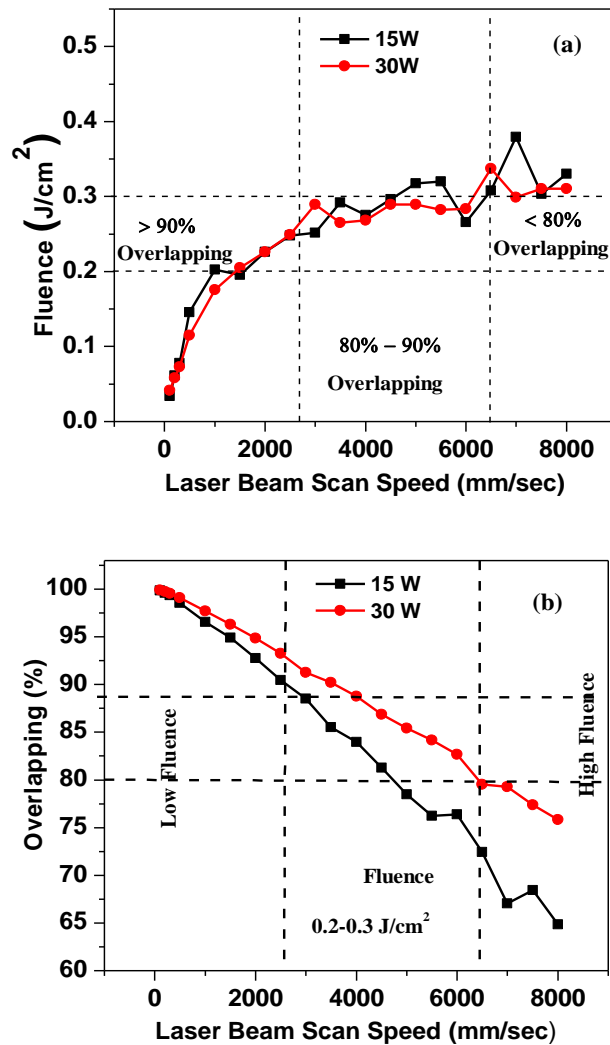


Figure 2.16: Calculated values of (a) laser fluence and (b) beam spot overlapping with laser scan speed

Figure 2.16a reveals that laser fluence at a distance of 5.5 mm above from the focus plane vary from ~ 0.25 mJ/cm^2 to ~ 0.3 J/cm^2 by varying scan speed from 0.1 m/sec to 8 m/sec but laser fluence value not vary significantly by varying laser power because as laser power increases the beam spot diameter also increases (Figure 2.15a.) resultant fluence value remains nearly same. Figure 2.16b reveals that the overlapping of beam spot vary from 99% to 65% when laser beam scan speed vary from 8 to 0.1 m/sec because by increasing the scanning speed the beam diameter decrease resultant

overlapping decreases. For organic contamination removal, the fluence on sample surface should be of the order of 0.1 to 1 J/cm² [54]. It is experimentally observed that for good cleaning efficiency the overlapping should be in the range of 80% to 90%. Overlapping more than 90% may damage the optical surface due huge energy deposition in beam spot region. Here we observed that at constant frequency 90 kHz overlapping of laser beam spot lies in 80% to 90% when laser beam scan speed vary from 2.5 to 6 m/sec. With a coverage of 80% to 90% overlapping region parameters we have removed carbon from Au thin film surface with several trails at different scan speed, power levels and number of passes of laser beam on sample surface. The confocal microscopic images (475 μm × 355 μm) of carbon removed surface at different laser power levels, scan speeds (v) and hatching separation are shown in Figure 2.17. Figure 2.17 (a-c) indicates that when scan speed is 0.8 m/sec. and laser fluence on sample surface is less (~ 0.18 J/cm²) the carbon from sample surface not remove completely even with increasing power and the number of passes of beam on sample surface. When we increase fluence (~0.25 J/cm²) by varying laser beam scan speed (3 m/sec) and power (30 W) most of the carbon removed in single beam pass and in 20 passes all the carbon removed completely. Further increase in scan speed from 3 m/sec to 10 m/sec (Figure 2.17 (d-i)) the fluence value increases from 0.25 to 0.3 J/cm² but increase of fluence value not give significant variation on carbon cleaning process. Figure 2.17 (i-l) indicates that increase in hatching separation also not affect the cleaning process. From these observations it is concluded that 0.25 to 0.3 J/cm² fluence is sufficient for carbon removing from Au surface without damaging the Au surface.

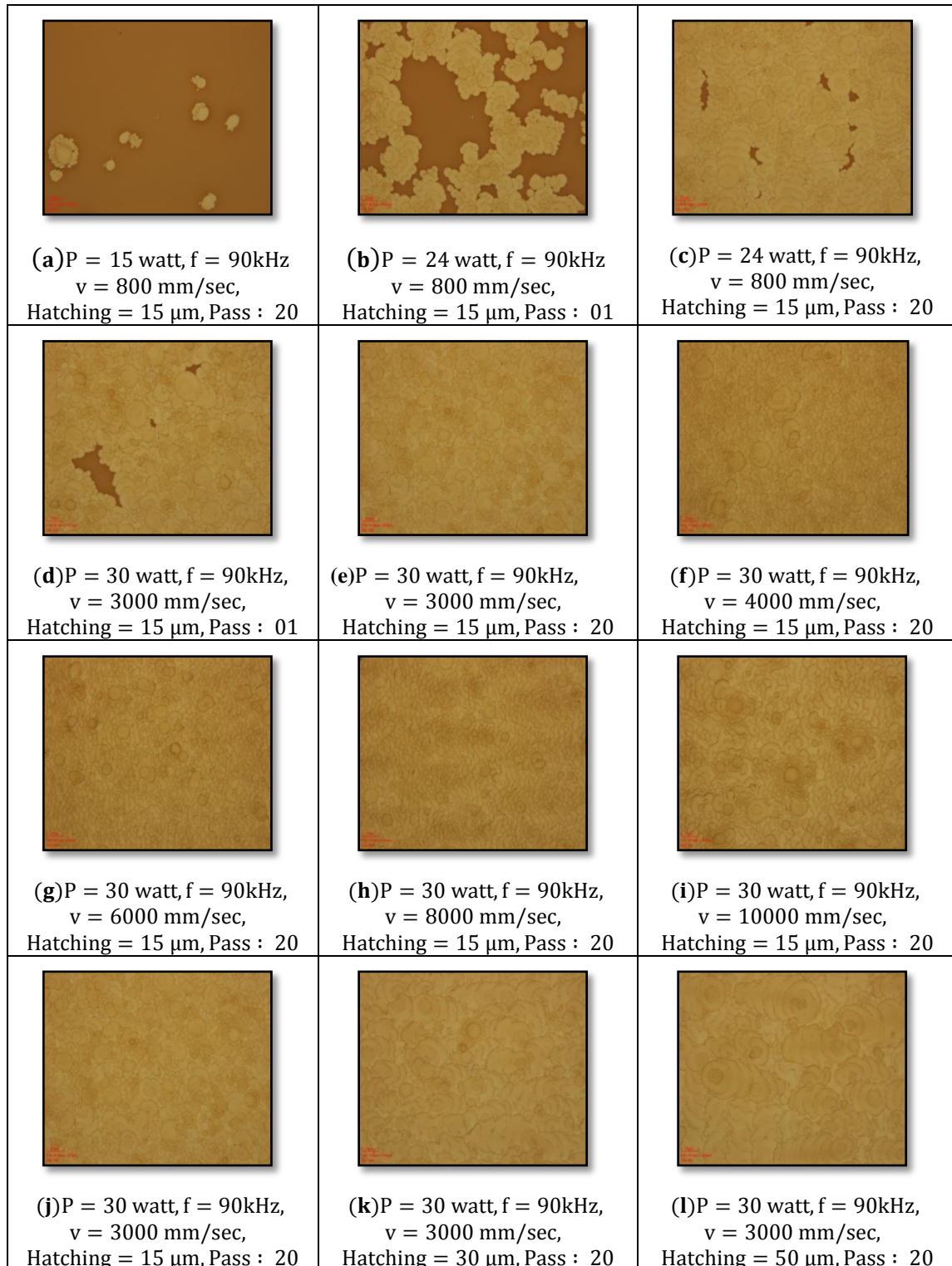


Figure 2.17: The confocal microscopic images ($473 \mu\text{m} \times 355 \mu\text{m}$) after carbon cleaning from Au thin film surfaces at different scanning parameters: power, scan speed (v), number of passes and hatching separation.

2.3 Surface Analysis Techniques

Different surface analysis techniques are used to see physical and chemical changes on optics and thin films surfaces before and after surface treatments for carbon removal. Descriptions of surface analysis techniques used in present studies are given below.

2.3.1 Soft X-ray Reflectivity (SXR)

In 1923, first time Compton reported the phenomena of total external reflection of x-ray from smooth surfaces [55]. Nowadays, due to significant development of synchrotron sources, instrumentation, detector technology and advancement in theoretical modeling and data analysis techniques, x-ray reflectivity becomes a powerful tool for characterization of thin film and multilayer structures. The technique gives information about electron density profile perpendicular to the sample surface and thereby obtain information about the thin film material density, its surface/interface and thickness [56]–[59]. When an interface is not perfectly sharp, but has average electron density profile $\rho_e(z)$ along the surface normal then the theoretical expression for the reflectivity can be written as [60], [61]

$$R(Q_z) = R_F(Q_z) \left| \frac{1}{\rho_\infty} \int_{-\infty}^{+\infty} \left\langle \frac{\partial \rho_e(z)}{\partial z} \right\rangle e^{iQ_z z} dz \right|^2 \quad (2.3)$$

Where ρ_∞ is average electron density deep inside the material, $R_F(Q_z) = \frac{(4\pi r_e \rho_\infty)^2}{Q_z^4}$ is Fresnel reflectivity of ideal surface. The reflectivity technique involves measuring the reflected x-ray intensity as a function of momentum transfer (Q_z) perpendicular to the sample surface, where $Q_z = \frac{2\pi}{\lambda} (\sin \theta_i + \sin \theta_r)$, θ_i and θ_r are incident and reflected

angles respectively and λ is wavelength of incident x-ray. In specular geometry incident and reflected angles are equal in magnitude resultant momentum transfer vector can be written as: $Q_z = \frac{4\pi \sin \theta}{\lambda}$. Typical geometry of reflectometry is shown in Figure 2.18. When x-rays are incident at grazing incidence angle on a flat material surface, the total external reflection occurs below a certain angle. This angle is known as critical angle (θ_c) of material for a given wavelength. The critical angle gives the information about material density ($\theta_c = \sqrt{2\delta}$), δ is dispersive part of refractive index that is proportional to the material density [61]. When incident angle of x-rays increases with respect to critical angle the penetration depth of x-ray increase and reflectivity decreases as fourth power of momentum transfer ($1/Q_z^4$)

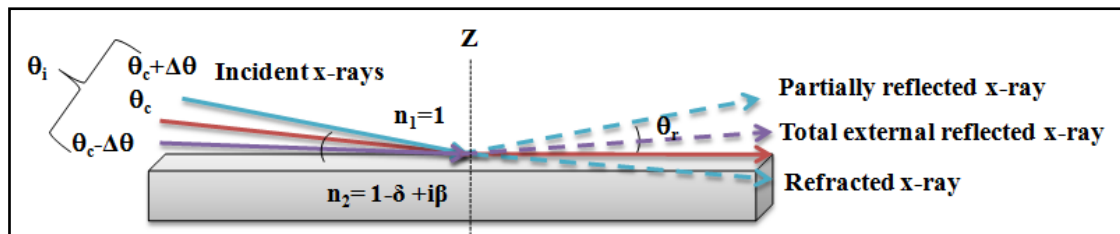


Figure 2.18: Representation of x-ray reflection at an interface of two different refractive index (n_1 and n_2) materials.

If a material is uniformly coated on another material having different refractive index (different electron density), then the reflected x-rays from the interface between the two materials and reflected x-rays from vacuum/air to the coating material interface produce interference pattern. The interference pattern gives information about thickness, density and roughness of coated material. The thickness of the film can be

determined by taking the difference between two consecutive maxima or minima of interference pattern.

$$t = \frac{\lambda}{2} \left(\frac{1}{\theta_{m+1}^2 + \theta_m^2} \right) \approx \frac{\lambda}{2\Delta\theta} \quad (2.4)$$

The resonant soft x-ray reflectivity is more sensitive compare to hard x-ray reflectivity because near the absorption edge of material the refractive index varies rapidly as a function of incident wavelength of the photon. Due to high sensitivity of soft x-ray technique the reflectivity experiments are carried out in soft x-ray energy region at Indus-1 and Indu-2 reflectivity beamlines.

2.3.1.1 Soft X-ray Reflectivity Beamline at Indus-2

The soft x-ray reflectivity beamline (BL-03) at Indus-2 is installed at a 5 degree port of bending magnet. The optical layout of reflectivity beamline at Indus-2 is shown in the Figure 2.19. The first optical element of the beamline is vertically mounted toroidal mirror (TM1) which deflect the incident beam in horizontal direction. The acceptance of mirror is 2 mrad in horizontal direction and 3 mrad in vertical direction. TM1 focuses the SR beam in both vertical and horizontal direction. Vertically it focuses the beam on to the entrance slit (S1) and horizontally on to the exit slit (S2). The second optical element is a spherical mirror (SM), which vertically deflects the beam and forms a convergent beam on the plane grating (shown in Figure 2.19). After spherical mirror, the beam is diffracted by the plane grating and by varying the angle of grating desired wavelength is focused on the slit S2. Three gratings G1, G2 and G3 of line densities 1200, 400 and 150 lines/mm are used to efficiently cover the whole energy region of 100 eV-1500 eV. The beamline provides moderate spectral

resolution ($E/\Delta E= 1-6 \times 10^3$) and high photon flux (ph/sec) in 10^9-10^{11} range with the use of three gratings. The gratings can be selected *in-situ* without breaking the vacuum for wavelength selection. In order to suppress higher harmonics coming from the monochromator, a high order harmonic suppressor (HOS) based on reflection principle is also installed between monochromator and TM2 in the beamline. The monochromatized light is focused on to the sample by TM2. The whole beamline operates in ultrahigh vacuum (UHV) environment of pressure less than 3×10^{-9} mbar.

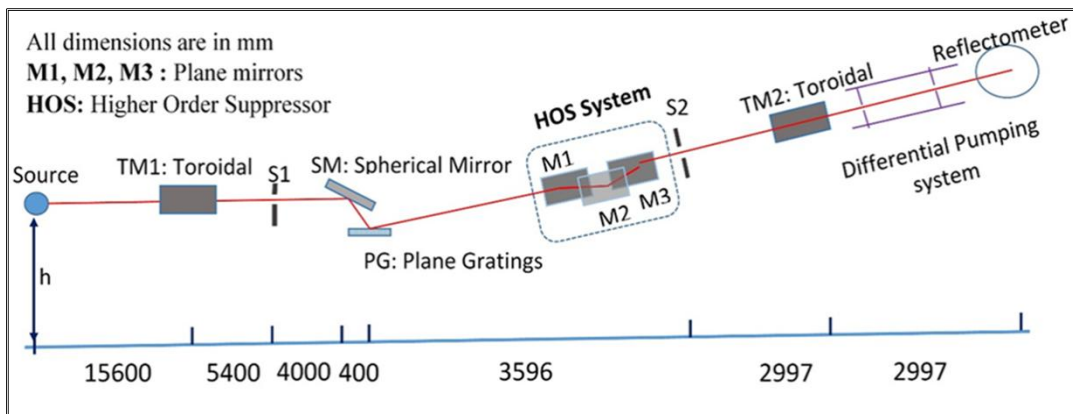


Figure 2.19: Optical layout of reflectivity beamline at Indus-2 synchrotron radiation source. Various optical elements of the beamline are indicated in figure.

The experimental station of beamline consists of x-y-z sample manipulation stages with a two axes high-vacuum (10^{-7} mbar) compatible goniometer. The scattering geometry is in the vertical plane which is suitable for s-polarized reflectivity measurements as synchrotron light is plane polarized in the horizontal plane. The sample and the detector are mounted on θ and 2θ axes of goniometer respectively. A high vacuum compatible linear translation stage is mounted on sample rotation stage for moving the sample in and out of the beam path. The present sample holder can accommodate a sample of size ($L \times W \times D$) up to $300 \text{ mm} \times 100 \text{ mm} \times 50 \text{ mm}$ and it

can bear load of 5 Kg. Detector arm is designed to mount multi detectors and therefore different detectors can be used for reflectivity measurements. Detector distance from the axis of rotation is about 200 mm. Two silicon photodiodes are mounted on detector arm, in which one is uncoated and other one is Aluminum (Al) coated. Al coating on detector reduce the background noise. Using these detectors, reflectance can be measured over five orders of dynamic ranges. The silicon photodiode detector (AXUV100G: IRD, USA) has 100 % internal quantum efficiency. The detector signal is measured in terms of current using a Keithley electrometer (6514). Inside view of the goniometer and the sample mounting stage are shown in the Figure 2.20. The reflectometer has a capability of positioning the sample within 2 μm and the angular position of the detector and sample can be set within 0.001° [62].

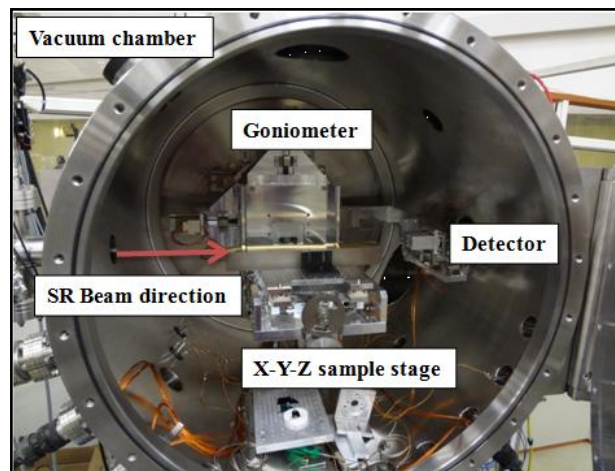


Figure 2.20: Inside view of experimental chamber with goniometer, x-y-z sample scanning stages and detector at reflectivity beamline of Indus-2.

2.3.2 Grazing Incidence X-ray Diffraction (GIXRD)

Grazing angle X-ray diffraction (GIXRD) technique is invented by Eisenberger and Cho in 1979. Due to low penetration into bulk material this techniques is more

sensitive surface of sample and Nowadays it is very common for characterizing nano size particles and thin film structures. The technique is based on Bragg diffraction principle ($2d\sin\theta = n\lambda$) but slightly different from conventional x-ray diffraction technique [63], [64]. At grazing incidence, x-rays interact with material within 50 nm to 100 nm range. In conventional x-ray diffraction method (θ - 2θ scan), due to high incidence angle interaction of x-ray with bulk is higher compare to the top surface layer, resultant weak signal from top layer and strong signal from the bulk (substrate) material is generated. In grazing x-ray diffraction in order to get the strong signal from top layer and to reduce the signal from the substrate material only 2θ angle scan is performed at constant grazing incidence angle (θ).

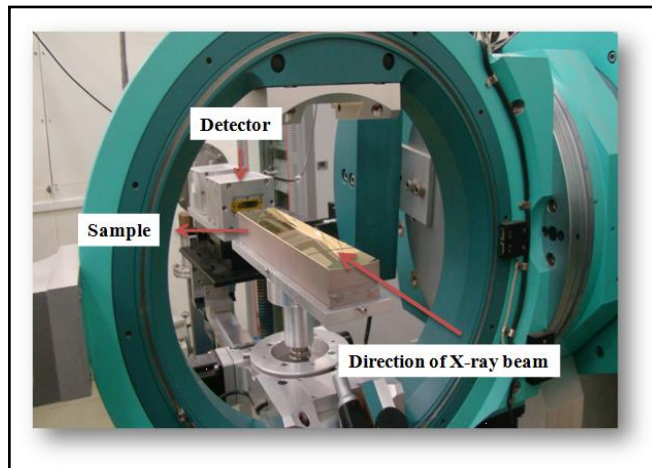


Figure 2.21: Experimental station for diffraction measurement at angle dispersive X-ray diffraction beamline (BL-12) of Indus-2 SR source.

In present studies, we are dealing with thin layer of carbon on gold and platinum coated mirrors, for thin layers GIXRD measurements are very useful for structural characterization of carbon layer. X-ray diffraction beamline of Indus-2 synchrotron radiation source is used in GIXRD mode for characterization of synchrotron radiation

induced carbon deposited on gold mirror surface [65]. The experimental setup at x-ray diffraction beamline of Indus-2 is shown in Figure 2.21. The energy of x-ray was chosen 11.4 keV using the double-crystal monochromator (DCM), at this energy the photon flux in the beamline is maximum ($\sim 10^{10}$ ph/sec). The incidence angle (θ) of beam was kept at 1 degree with respect to the sample surface and the detector (2θ) was moved from 10 to 45 degree in steps size of 0.04 degree.

For characterization of carbon deposited on lithium fluoride (LiF) window laboratory source (Bruker AXSD-8 advance x-ray diffractometer with $\lambda=1.54$ Å monochromatic radiation source (Cu $K\alpha$)) was used. The diffraction measurement was carried out by keeping fixed incidence angle at 0.6 degree and detector rotates from 15 to 90 degree with step size of 0.01 degree.

2.3.3 X-ray Photoelectron Spectroscopy (XPS)

Photoelectron spectroscopy (XPS) is very popular technique for study of chemical composition, chemical state and empirical formula of elements present into material [66]–[68]. The technique is based on principle of photoelectron emission described by Einstein in 1905 [69]. In XPS measurement, x-ray beam continuously irradiate the sample surface, simultaneously numbers of photoelectrons generated from the top surface (≤ 100 Å) of material with different kinetic energy. The kinetic energies of emitted electrons are measured by energy analyzer. The photoelectrons generated at depth d from the surface, increase the signal intensity by $I_d = I_0 e^{-\frac{d \cdot \cos \theta}{\lambda}}$. Where I_0 - initial intensity of electrons at depth (d), θ and λ are the detection angle with respect to the sample normal and the inelastic mean free path of electrons respectively. The electrons generated above the escape depth did not contribute to the intensity;

consequently the information about material is obtained only up to couples of nanometers. The kinetic energy of the photoelectrons is given by

$$E_{K.E} = E_{I.E} - (E_{B.E} + \phi) \quad (2.5)$$

Where $E_{K.E}$ and $E_{B.E}$ are kinetic and binding energies of electrons respectively, $E_{I.E}$ is incident photon energy and ϕ is the work function of material. The photo-electrons emitted from the sample surface are differentiated according to their kinetic energies. The kinetic energy of ejected electrons is measured by concentric hemispherical analyzer. In order to filter out the electrons of energies E_0 , the hemispheres are charged to maintain a potential difference

$$V_1 - V_2 = \frac{E_0}{e} \left(\frac{R_2}{R_1} - \frac{R_1}{R_2} \right) \quad (2.6)$$

Where V_1 and V_2 are the potentials applied to the inner and the outer hemisphere respectively, E_0 is the electron pass energy, e is the elementary charge of electron, R_1 and R_2 are the radii of the inner and outer hemispheres respectively.

The schematic of concentric hemispherical analyzer is shown in Figure 2.22. Electrons of different kinetic energy are selected by analyzer by varying the potential between the concentric spheres. The detector measures electron current that are passed through the analyzer at different applied voltage with different kinetic energy. The spectrum of kinetic energy or binding energies of electrons versus electron current (intensity) is recorded by the use of computer program.

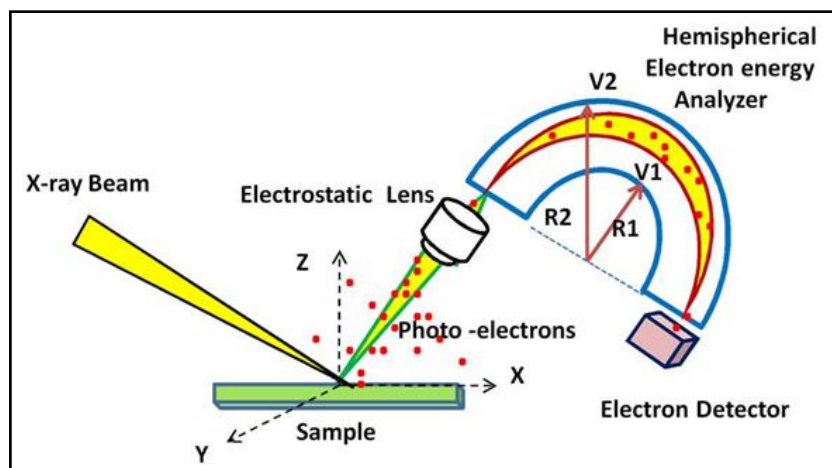


Figure 2.22: Schematic diagram of X-ray Photoelectron Spectroscopy experimental setup.

The binding energies of elements are elemental specific and unique those are used for elemental identification with the help of available database in literature. The qualitative analysis of spectra is usually done by comparing the measured photoelectron intensity lines with reference spectrum lines [70]. The concentration of the element x in an homogeneous sample can be calculated by the relation $C_x = \frac{I_x/S_x}{\sum I/S}$.

Where I_x is the intensity of element x , S_x is the sensitivity factor for the measured line of the element x , and $\sum I/S$ is the sum of normalized intensities of all the detected elements. Usually the XPS spectrum has large background so, for accurate intensity determination from XPS spectrum a suitable background subtraction method are used [71].

2.3.4 Atomic Force Microscopy (AFM)

Due to synchrotron radiation induced carbon deposition on mirror surface the surface topography of the mirror changes. The carbon cleaning techniques used for removing carbon from optic surface may also vary surface roughness of mirror. The surface

topography of samples used in the study is measured by atomic force microscopy using Agilent 5600LS machine. In order to avoid any surface damage all the measurements are carried out in non contact mode.

Atomic force microscopic technique was developed by G. Binnig and H. Rohrer in the early 1980s, the first experiment was made by Binnig, Quate and Gerber in 1986 and earned Nobel prize in physics [72]. Due to high vertical resolution ($\approx 1 \text{ \AA}$) it is a powerful tool for the study of surface morphology. The AFM machine consists of four important sub systems that's work together. The first one is the laser, second one is piezoelectric based sample stage, the third one is a flexible cantilever, ended with a sharp tip on its free end and the fourth and important component is the position sensitive detector. The laser beam shine on a mirror and directed on the tip mounted cantilever where its reflection take place. After reflection the laser beam is detected by a position sensitive photodiode detector. The schematic diagram of atomic force microscopy (AFM) is shown in Figure 2.23. When the tip is well above the sample surface, the angle of the mirror is adjusted in such a way that the reflected beam from sample surface directly hits the center position of the detector. When tip and sample are brought closer to each other, the piezoelectric stage scans the sample under the cantilever tip. When sample move under tip the cantilever feel force due to atomic interaction (Vander Waal force type), depending on magnitude of force tilting or bending of cantilever take place. The tip and surface interaction is sensed by monitoring the deflection of cantilever. The reflected beam from cantilever surface hit the four-quadrant position sensitive photo-detector (PSPD). The bending of cantilever change the position of laser spot on the detector results in change in output voltage of

the photo-detector. The small variation in cantilever position results in large variation in position of beam spot at detector because the distance between cantilever and the detector is large compare to the cantilever length. If we know the sensitivity of detector and the force constants of cantilever than the force acting on the cantilever can be easily measured by measuring the change of output voltage of PSPD. The normal deflection generates intensity difference between the upper and lower segments of the four-quadrant photo-detector, which is proportional to height variation and gives surface topography. The deflection in left and right segments is proportional to the torsion of the cantilever. By this method displacement of tip about 10 \AA can be easily detectable [73]. The fine positioning of AFM tip with respect to the sample surface is done by piezoelectric stage.

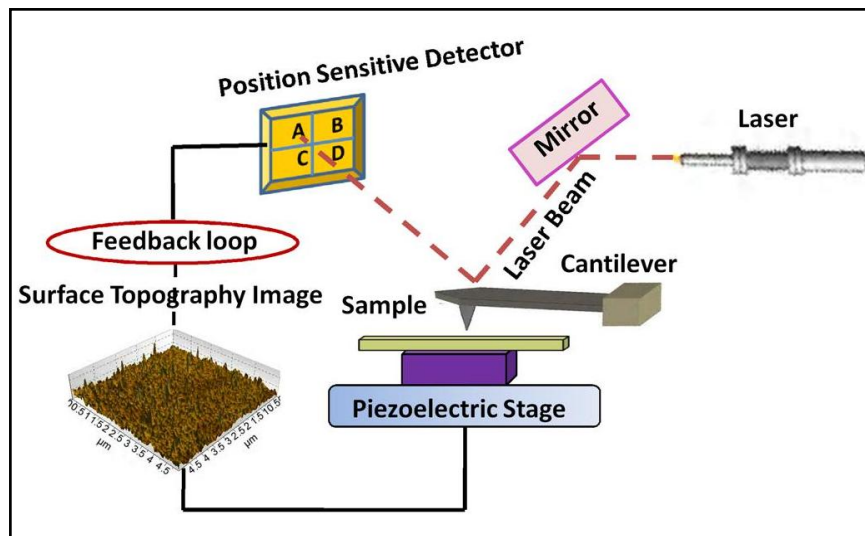


Figure 2.23: Schematic diagram of atomic force microscope (AFM) apparatus and related basic components.

2.3.4.1 Modes of AFM Operation

When cantilever tip came close the sample surface it experiences attractive and repulsive forces. These forces define two modes of operation (i) Contact mode and (ii) Non contact mode. In between Contact and Non contact modes is one more mode generally known as (iii) Intermediate contact mode. In this section, we discuss the two main operating modes of AFM that are commonly used for measurement. For soft and sensitive surfaces the non contact mode is used whereas for hard surfaces a contact mode can be used.

Contact Mode: In contact mode surface of the sample and the tip of AFM have close contact. For avoiding the damage of tip this mode is restricted to flat surfaces only. In this mode the feedback loop allows the scan in two ways the first one is constant force and the second one is the constant separation distance. In constant force mode a feedback loop is used to control of separation between tip and sample surface. Thus, the scanner responds instantaneously via feedback loop to topographical changes by keeping the constant cantilever deflection and the surface topography is deducted from the voltage applied to the piezoelectric stage.

Non-Contact Mode: There are two ways of non-contact mode, one is known as intermediate contact mode and second one is known as non contact mode. In intermediate mode the cantilever oscillates perpendicular to the sample surface with a free space resonant frequency of cantilever at a distance of about 100 Å to 1000 Å, so its oscillation covers both the regions of attractive and repulsive force between the tip and the surface. When tip scan over the sample surface, the tip resonance frequency varies with the separation between surface and tip. The separation between tip and

surface is controlled by tracking the change in oscillating frequency. The cantilever displacement normal to the surface is controlled by a feedback loop keeping the resonance frequency constant. The information about surface topography comes from the changes in oscillation amplitude and the phase. In non contact mode the cantilever oscillates about 100 Å to 150 Å away from surface in attraction force region with slightly higher frequency compare to cantilever free space resonance frequency. When cantilever brought closer to the sample surface the vibration amplitude decreases significantly. The amplitude of oscillations is directly related to the separation between tip and surface.

2.3.5 Raman Spectroscopy

The Raman spectroscopy is also known as vibrational spectroscopy in which the Raman bands are arises due to change in polarizability of molecules by incident light and molecule interactions. When a beam of light impinges on molecules, some amount of light is absorbed and some amount is scattered. The majority of scattered photons have same wavelength as the incident one and the process is known Rayleigh scattering (elastic scattering). In addition to Rayleigh scattering, certain discrete wavelengths higher and lower than the incident one are also observed (inelastic scattering). Inelastic scattering of light was first observed experimentally by C.V Raman in 1928 and theoretically described by Adolf Smekal in 1923 and [74] .

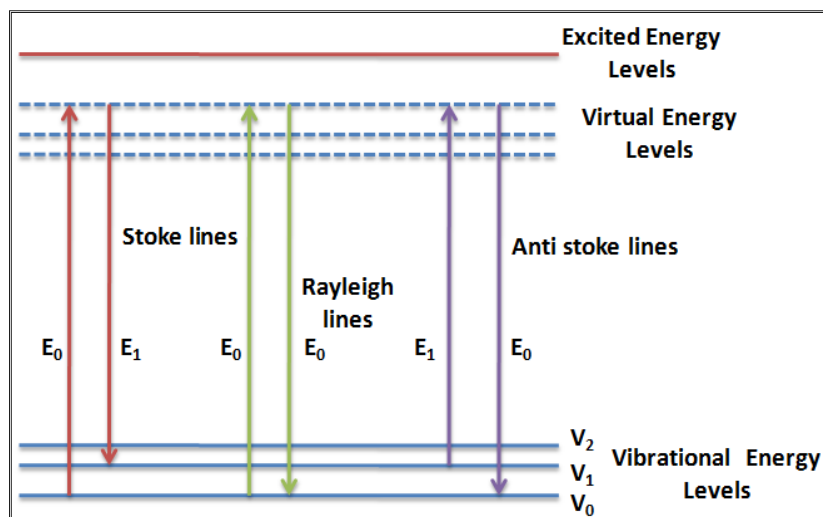


Figure 2.24: Energy level diagram of Raman scattering indicating Stokes, Anti-stokes and Rayleigh lines.

Energy level diagram of Raman process indicating stokes, anti-stokes and Rayleigh lines are shown in Figure 2.24. To understand the Raman phenomena, consider a molecule placed in oscillatory field ($E = E_0 \sin\omega t$) with frequency ω_0 . The oscillating field produces oscillating dipole moment $\mu = \alpha E_0 \sin\omega_0 t$ [75]. The magnitude of dipole moment (μ) depends on the intensity of applied electric field (E) and the polarizability (α) of the molecule. Such oscillating dipoles emit radiations of its own oscillating frequency, this is the case of Rayleigh scattering. During applied oscillating field if the molecule vibrate or rotate than its polarizability not remains constant but it changes periodically with vibrational or rotational frequency (ω_1).

$$\alpha = \alpha_0 + A \sin\omega_1 t \quad (2.7)$$

Where α_0 - is equilibrium polarizability and A - represents rate of change of polarizability with vibrations. In presence of rotational or vibrational motion the induced dipole moment is given by

$$\mu = (\alpha_0 + A \sin \omega_1 t) E_0 \sin \omega_0 t \quad (2.8)$$

$$\mu = \alpha_0 E_0 \sin \omega_0 t + \frac{1}{2} A E_0 [(\cos(\omega_0 - \omega_1) t - \cos(\omega_0 + \omega_1) t)] \quad (2.9)$$

In above equation, the first term of right hand side represents Rayleigh scattering in which oscillating dipole radiates with incident radiation frequency. The second term represents stoke Raman scattering in which radiated field frequency decreased by the vibration frequency and the third term represent anti-stoke Raman scattering in which radiated field frequency increased by the vibration frequency. If the rotational or vibrational motion not change the polarizability of molecule, then $A = 0$, dipole oscillate and radiate with same incident frequency of field. From this statement it is clear that to be Raman active molecule, that rotational or vibrational motion must generates some change in polarizability. The Raman scattering cross section depends on how many vibrational energy levels are occupied. The occupancy of the vibrational levels is determined by Boltzmann statistics and strongly depends on the temperature, at low temperatures, only the ground state vibrational states are occupied and the probability of transition from ground to virtual states is high enough compare to transition from excited vibrational state to virtual states, thus the anti-stokes scattering almost goes to zero. The intensity ratio of anti–stokes (I_{AS}) to stokes (I_S) lines is given by [76].

$$\frac{I_{AS}}{I_S} \propto \exp\left(\frac{-h\omega_1}{k_B T}\right) \quad (2.10)$$

Where ω_1 - vibrational frequency, h - Planck's constant and k_B - Boltzmann's constant.

2.3.6 Optical Emission Spectroscopy

Optical Emission Spectroscopy (OES) is a well known and widely used analytical technique for the analysis of broad class of elemental compositions. Schematic diagram of optical emission spectrometry is shown in Figure 2.25.

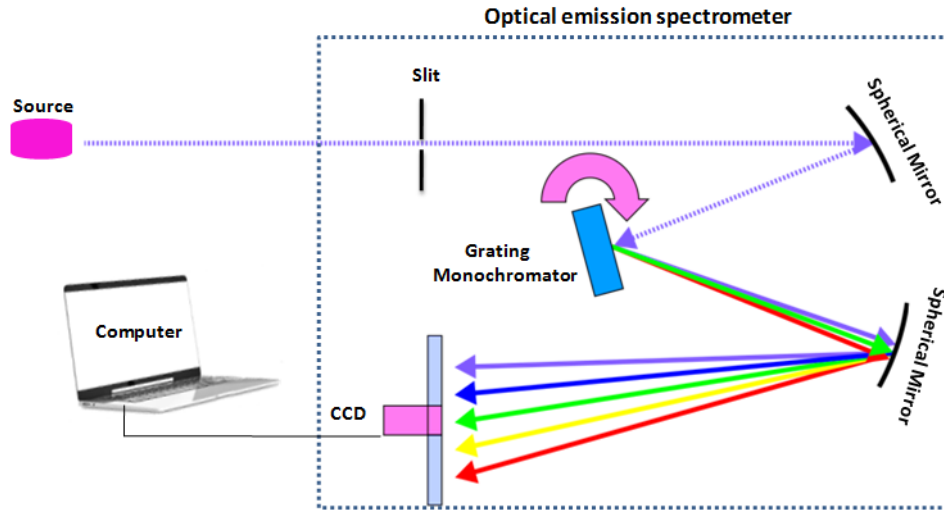


Figure 2.25: Schematic diagram of optical emission spectrometer used for measuring optical emission lines CO and O in rf plasma chamber during optics cleaning.

In present work this technique is used to see relative change in CO and O optical emission line intensities in rf plasma. The presence /absence of CO in plasma give indication of presence/absence of carbon on mirror surface during plasma exposure. The intensity of emission lines is directly proportional to the concentration of the originating element in the sample. The intensity of a transition I_{ul} from a higher $|u\rangle$ energy state to a lower $|l\rangle$ energy state in a given plasma volume can be written as[77]

$$I_{ul} = A_{ul} (h\nu)_{ul} V N_u \quad 2.11$$

where A_{ul} is the Einstein transition probability of spontaneous emission (s^{-1}), h the Planck constant, ν the frequency of the emitted photon (s^{-1}). V is the emitting volume and N_u is the volume number density of emitting species (m^{-3}) in upper energy state.

2.4 Summary

Carbon contamination removal without affecting optic surface properties is a challenging task. In order to remove carbon from optics surface development of optics refurbishing techniques and their optimization process are discussed in this chapter. During process optimization in case of CCP plasma 10 watt rf power at 5×10^{-2} mbar oxygen pressure is found suitable for carbon removal without affecting surface properties of optics. In case of UV exposure it is observed that at 4-5 mm distance from source the carbon cleaning rate is nearly 25 Å/hr and in IR laser cleaning technique it is observed that fluence in 0.25 to 0.3 J/cm² range is good for carbon removal from Au coated surface. Different surface analysis techniques used to see the effect of surface treatments for carbon cleaning on optics surface are discussed in detail. Soft x-ray reflectivity is used for surface analysis before and after surface treatment for carbon removal, with this technique change in layer thickness, surface roughness and density of material is determined. AFM technique is used as a supplementary technique for surface morphology measurement. Grazing incidence x-ray diffraction technique is used to see the bulk structural changes after surface treatments. XPS is used for chemical analysis of optics surface before and after surface treatments. Raman Spectroscopy technique is used to see the variation in carbon phase by synchrotron radiation dose, Raman spectroscopy technique is more sensitive different hybridization state of carbon. Finally optical emission spectroscopy

technique is used for determination of carboneous gases concentration in rf plasma during carbon cleaning process using capacitively coupled rf plasma.

3 Characteristics of Synchrotron Radiation Induced Carbon Layer

3.1 Overview

Carbon is a versatile element in the nature which exists in different allotropic forms. The well-known allotropes of carbon are diamond, graphite and amorphous carbon. Characteristics of these allotropes are significantly different from each other. Diamond is highly transparent and hardest naturally occurring material whereas graphite is opaque (black) and is relatively soft material. The carbon growth on optical elements occurs by interaction between synchrotron radiation, photoelectrons and adsorbed hydrocarbons on the surface of optics. The growth mechanism and characteristics of synchrotron radiation induced carbon layer deposited on optical elements are not well known and still debatable. The properties of the carbon contamination layer vary with presence of hydrogen contents and hybridization states of carbon. Hydrogen contents in the contamination layer depend on irradiation time and partial pressure of hydrocarbon gases. Contamination layer with 40-60% hydrogen contents are soft in nature and known as polymer-like a-C: H (PLCH) films. The films, with 20-40% hydrogen contents have relatively higher sp^3 hybridized carbon bonding than polymer-like a-C:H films, resultantly they have better mechanical properties and known as hydrogenated diamond-like carbon (DLC:H). Higher percentage of sp^3 hybridize carbon bonding (~70%) with 25–30% hydrogen content make special class of hydrogenated DLC films known as tetrahedral hydrogenated amorphous carbon films (ta-C: H) [78]. The films with low hydrogen contents and higher sp^2 hybridized carbon

bonding with aromatic structure are known as hydrogenated graphite-like amorphous carbon (GLCH) films [79]. Tetrahedral hydrogenated amorphous carbon (ta-C:H) films have lower hardness as well as lower density compare to tetrahedral amorphous carbon (ta-C) films because sp^3 bonds of C–H are weaker than sp^3 C–C bonds. Using ternary phase diagram (hydrogen, sp^2 and sp^3 hybridized carbon contents) Ferrari & Robertson explained the different phases of carbon [80]. Micro-crystalline graphitic carbon to glassy carbon have significant amount of sp^2 hybridized carbon contents. Diamond-like carbon (DLC) is an amorphous carbon with a significant fraction of sp^3 hybridized carbon contents with other carbon contents. Amorphous carbon is also known as intermediate structure between diamond and graphitic carbon and exhibit character of both types of carbons, depending on sp^2/sp^3 hybridized carbon fractions. The carbon layer with the same sp^3 hybridized carbon content and hydrogen concentration but different sp^2 hybridized carbon clustering and its orientation may have different optical, electronic and mechanical properties [81]. In synchrotron radiation beamlines, due to continuous exposure by photons, secondary electron and ions clustering of carbon atoms, sp^2 to sp^3 hybridized carbon ratio and hydrogen contents in hydrogenated carbon layer deposited on optical elements may vary. Faradzhev et al. [82] studied, carbonaceous layer induced by EUV radiation on TiO_2 thin film surface by x-ray excited valence-band spectra and gas Chromatography/Mass Spectroscopy (GC/MS). They concluded that due to continuing EUV irradiation, cross-linking and hydrogen abstraction in polycyclic aromatic hydrocarbon (PAH) occurs. Due to hydrogen abstraction and subsequent cross-linking in alkane fragments form a complex network of carbon bonds, resultant sp^2 hybridized carbon-rich film is formed. Dolgov et al. [15] characterized EUV induced carbon layer, they observed

that the film have a tough structure with the significant part of the carbon being in sp^3 hybridization state (DLC). The carbon in the layer have C-C, C-H, C-OH and C(O)OH chemical groups. From these studies it is observed that radiation induced carbon layer properties strongly depends on photon dose (exposure time) and photon energy. In this chapter, we characterized synchrotron radiation induced carbon contamination layer deposited on surface of gold coated pre-mirror (TM1) of soft x-ray reflectivity (SXR) beamline (BL-04) [21] and surface of LiF window used in high resolution vacuum ultraviolet (HRVUV) beamline (BL-01) [19] at Indus-1 synchrotron radiation source.

3.2 Samples for Study

3.2.1 Toroidal Mirror of Reflectivity Beamline

Soft x-ray reflectivity beamline at Indus-1 SR source consists of two gold coated toroidal mirrors and three gratings in monochromator [21]. The beamline is in operation since the year 2001. Vacuum of the beamline is maintained in $\sim 10^{-9}$ mbar range. Due to prolonged use of optical elements in the beamline, these optical elements has got thick carbon contamination layer on top of reflective gold surface. The pre-mirror (TM1) of the beamline is exposed to high photon flux of wavelengths covering from infrared to soft x-ray region. The pre mirror accepts SR beam 10 mrad in horizontal direction and 5.9 mrad in vertical direction. At 450 MeV electron energy and 100 mA current the maximum radiated SR beam power in 10 mrad acceptance of mirror is about 577 mW, which is received by the pre- mirror of the beamline making it more prone to carbon contamination. Due to Gaussian profile of synchrotron radiation beam intensity, the photon intensity is maximum at the center and it

decreases in both directions along the length from center resultantly the thickness of the carbon layer also decreases from mirror center to outwards direction along the length of the mirror. The beamline optical layout and position of TM1 is shown in Figure 3.1. This carbon contaminated mirror was taken out from the beamline and used for detailed characterization of carbon contamination layer.

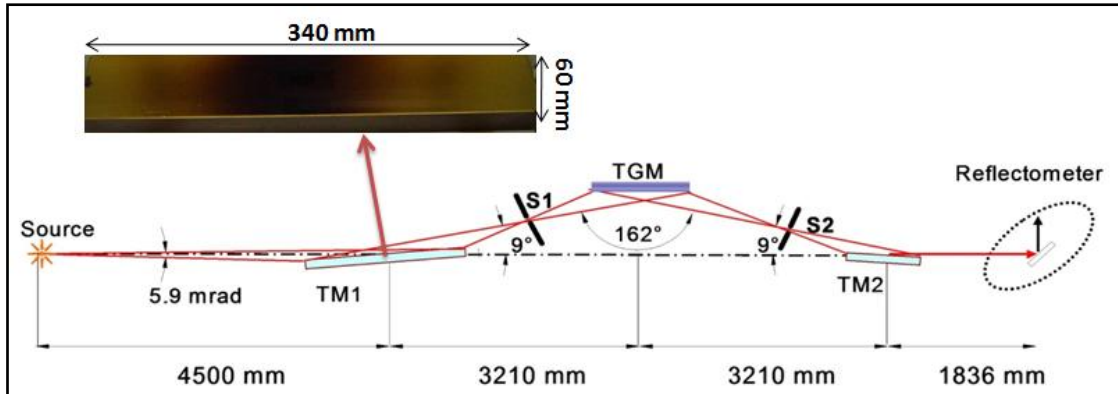


Figure 3.1: Indus-1 reflectivity beamline (BL-4) optical layout with carbon contaminated Au coated pre-mirror. TM1 and TM2 represent pre and post toroidal mirrors, S1 and S2 represents entrance and exit slits.

3.2.2 LiF Window of HRVUV Beamline

A LiF window used as low pass filter in high resolution vacuum ultraviolet (HRVUV) beamline [19] of Indus-1 synchrotron radiation source also got deposited a thick carbon contamination layer in the beamline environment and therefore was considered as an another sample for the study of characteristics of SR induced carbon layer. In this sample, carbon contamination layer was deposited in slightly different environment compared to previous one. In the previous case the mirror was irradiated for more than a decade with all kind of photon energy coming from bending magnet source whereas in this case the carbon contamination layer was deposited in a short time exposure of about 100 hrs with photons of 3 eV to 11.5 eV energy that are

transmitted through the LiF window. This window was basically used to isolate the experimental station from rest of the beam line. Pressure in the beamline towards experimental station was $\sim 10^{-6}$ mbar and towards the storage ring side it was $\sim 10^{-9}$ mbar. In high pressure regime hydrocarbon concentration is supposed to be high, resultant carbon contamination layer deposited on the face of high pressure side. The contamination layer deposited on LiF window is shown in the Figure 3.2.

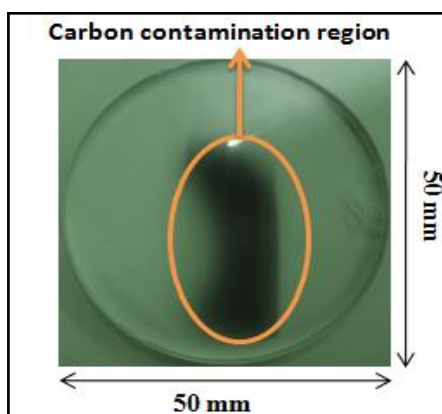


Figure 3.2: Carbon contaminated LiF window of 50 mm diameter. Marked area in photograph indicates contamination region as well as SR beam foot print.

3.3 Contamination Layer Thickness and Density

Carbon contamination layer thickness and its density from gold mirror and the LiF window surfaces were determined by soft x-ray reflectivity measurements. The specular reflectivity (θ - 2θ scan) probes the contamination layer along the depth (z-direction) of sample by measuring the reflected intensity as a function of momentum transfer (Q_z) along the surface normal. Three different wavelengths (80 Å, 90 Å and 100 Å) were chosen for soft x-ray reflectivity measurements of carbon contaminated gold mirror and 60 Å, 70 Å and 80 Å were chosen for LiF window case. The detail about the SXR beamline (BL-04) at Indus-1 is given in chapter-2. Critical

angle, slope of reflectivity curve and interference fringe pattern are the key features of specular reflectivity by which density of layer, surface/interface roughness and thickness of layer can be estimated. The focused SR beam was targeted on dense carbon contaminated region for reflectivity measurements. Experimentally measured specular reflectivity spectra at different wavelengths are shown in Figure 3.3a. and Figure 3.3b for carbon layer on Au mirror surface and LiF window respectively. The measured reflectivity spectra are fitted using Parratt recursive formalism that is based on Fresnel reflection equations [83]-[84].

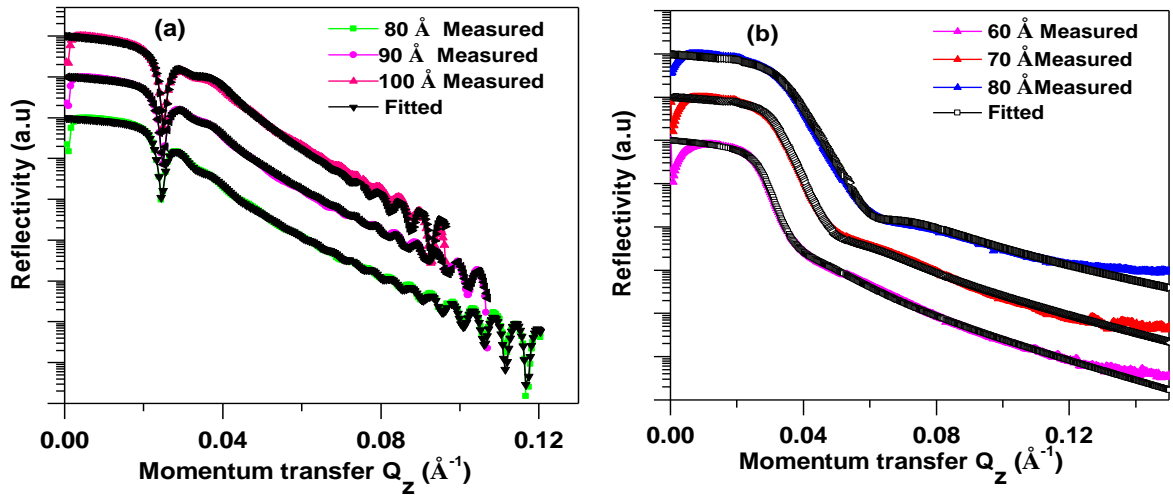


Figure 3.3: Experimentally measured and fitted reflectivity spectra of (a) carbon-contaminated Au mirror surface (b) carbon contaminated LiF window surface.

From the reflectivity spectra fittings, optical constants (δ and β) and structural parameters (thickness, roughness and optical density) of the carbon contamination layers are determined. Optical constants are related with refractive index $n(\omega)$ of material with relation $n(\omega) = 1 - \delta + i\beta$, where $\delta = \frac{n_a r_e \lambda^2}{2\pi} f_1^0(\omega)$ and

$$\beta = \frac{n_a r_e \lambda^2}{2\pi} f_2^0(\omega). \quad n_a, r_e \text{ and } \lambda \text{ are atomic density, classical electron radius and}$$

incident radiation wavelength respectively. $f_1^0(\omega)$ and $f_2^0(\omega)$ are real and imaginary part of atomic structure factor. From best fitting results it is observed that the carbon layer deposited on Au mirror surface has thickness (t) ≈ 406 Å surface roughness (σ) ≈ 60 Å and optical density (O.D) $\approx 73\%$ of graphitic carbon density whereas carbon layer deposited on LiF window surface has thickness (t) ≈ 100 Å surface roughness (σ) ≈ 60 Å and optical density $\approx 94\%$ of graphitic carbon density. In soft x-ray regime dispersive part (δ) of frequency dependent refractive index $n(\omega)$ of material represent optical density. The optical constants values of contamination layer are close to the optical constants of graphitic carbon (shown in table-3.1 and table-3.2). The slight difference in optical constants from graphitic carbon may be due to presence of hydrogen contents in the contamination layer. The variation in carbon layer thickness, roughness and optical density indicate that the growth of carbon strongly depends on exposure time, incident energy and the residual gases in vicinity of optics.

Table 3.1: Structural (t - thickness, σ - roughness and O.D- optical density) and optical (δ and β) parameters of carbon contamination layer deposited on Au coated mirror surface measured at three different wavelengths of incident radiation.

λ (Å)	t (Å) Carbon	O.D w.r.t GC (%)	δ_c $\times 10^{-3}$	β_c $\times 10^{-3}$	σ_c (Å)	t (Å) Gold	δ_{Au} $\times 10^{-2}$	β_{Au} $\times 10^{-3}$	σ_{Au} (Å)
80	406	72	9.2	1.0	60	504	2.2	8.76	18
90	406	72	12.0	1.5	62	505	3.3	10.9	19
100	406	75	15.1	2.2	63	504	4.8	12.1	21

Table 3.2: Structural (t - thickness, σ - roughness and O.D- optical density) and optical (δ and β) parameters of carbon contamination layer deposited on LiF window surface measured at three different wavelengths of incident radiation.

λ (Å)	t (Å) Carbon	O.D w.r.t GC (%)	δ_c $\times 10^{-3}$	β_c $\times 10^{-4}$	δ_{LiF} $\times 10^{-3}$	β_{LiF} $\times 10^{-3}$	σ_c (Å)	σ_{LiF} (Å)
60	101	95	6.36	9.05	9.22	2.44	55	9
70	101	96	9.52	12.8	11.2	3.64	55	9
80	101	93	12.1	20.9	14.3	5.14	51	8

3.4 Crystallinity of Synchrotron Radiation Induced Carbon Layer

The degree of crystallinity of a material strongly affects its hardness, density, optical and electrical properties. X-ray diffraction is a powerful technique for the study of crystallinity of a material. For the study of carbon contamination layer crystallinity, grazing incidence X-ray diffraction measurement was carried out. For carbon layer deposited on Au mirror the diffraction measurement was carried out at angle dispersive X-ray diffraction (ADXRD) beamline of Indus-2 SR source [65] and for carbon layer deposited on LiF window diffraction measurement was carried out by Bruker diffractometer (AXSD-8). The details of X-ray diffraction technique are discussed in chapter-2. The diffraction pattern recorded from carbon contaminated Au mirror surface is shown in Figure 3.4. In the diffraction pattern, a broad peak centered at 14.8° (2θ) shows the presence of carbon and this broad peak reveals that carbon on mirror surface is not in crystalline form but it is deposited in the form of amorphous carbon (a-c) or in the form of small carbon clusters. The two additional peaks at 26.7° and 30.9° represents diffraction from (111) and (200) planes of face centered cubic (*fcc*) structure of Au. In order to calculate cluster size, the broad peak is fitted considering Gaussian shape function.

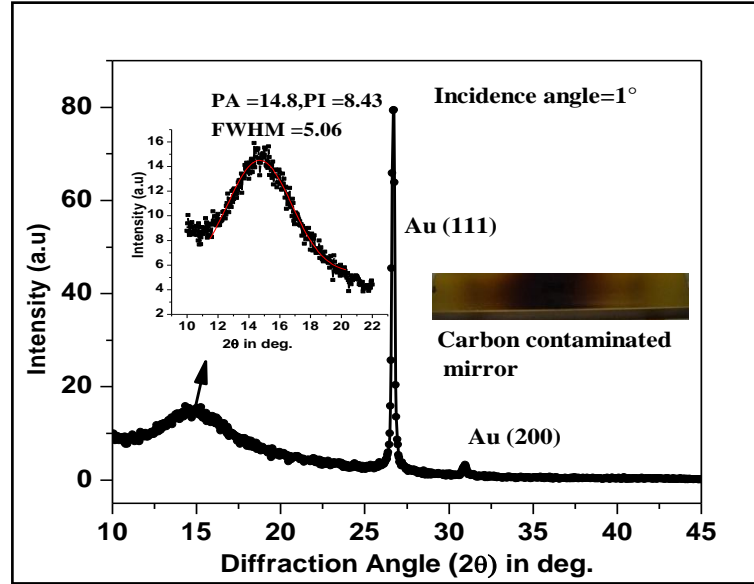


Figure 3.4: Grazing incidence X-ray diffraction pattern of SR induced carbon contamination layer from Au mirror surface.

Out of plane cluster size of carbon deposits was estimated by well-known Scherrer equation [63].

$$t = \frac{K\lambda}{B \cos \theta} \quad (3.1)$$

$$t = \frac{0.9 \times 1.08}{0.088 \times 0.99} = 11.6 \text{ \AA} \quad (3.2)$$

Where, t represents mean cluster size, λ is the wavelength used for measurement, B is the line broadening at half the maximum intensity ($\Delta 2\theta$ in radian) and θ is the Bragg angle and K is a dimensionless shape factor, its typical value is about 0.9, but it varies with the actual shape of the crystallite in sample.

The diffraction experiment from carbon contaminated LiF window surface was carried out on Bruker AXSD-8 Advance X-ray diffractometer. The diffractometer consist of CuK_{α} , monochromatic radiations ($\lambda = 1.54 \text{ \AA}$) source. In order to make comparison

with graphitic carbon, diffraction spectrum from commercial graphitic carbon sample was also recorded in same experimental conditions (see Figure 3.5).

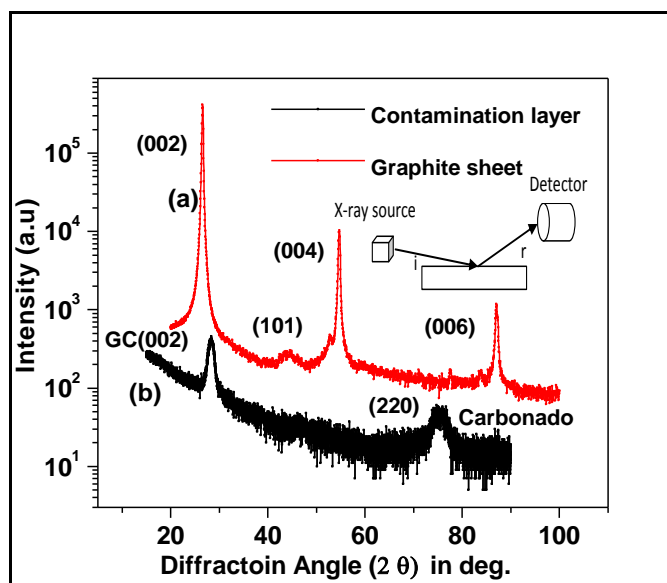


Figure 3.5: Grazing incidence X-ray diffraction pattern measured by $\text{Cu K}\alpha$ radiation ($\lambda=1.54\text{\AA}$) source (a) carbon contamination layer deposited on LiF window (b) commercial graphitic carbon sample.

In commercial graphitic carbon sample four diffraction peaks from (002), (101), (004) and (006) planes of graphitic carbon structure were observed, whereas only two distinct diffraction peaks at $2\theta = 28.3^\circ$ and 75.8° , from carbon contamination layer were identified as reflections from (002) planes of graphitic carbon and from (220) planes of carbonado phase of carbon respectively. The magnified GIXRD spectra with Gaussian fitting in peaks region are shown in Figure 3.6. The diffraction pattern clearly indicates that carbon in the contamination layer has crystalline structure with graphite and carbonado phases of carbon. The spacing in (002) planes is determined 3.14 \AA and for (220) planes is 1.26 \AA . The interlayer spacing of (002) planes of graphite and semi-graphite carbons normally lies within a value of $3.54\text{ \AA} - 3.37\text{ \AA}$. In

SR induced carbon contamination layer the observed interlayer spacing is very near to the value of graphite interlayer spacing reported in various studies [85]–[87].

The out of plane grain size (t_{out}) using Debye Scherrer equation for graphitic carbon and carbonado phase is determined $\sim 60 \text{ \AA}$ and $\sim 29 \text{ \AA}$ respectively.

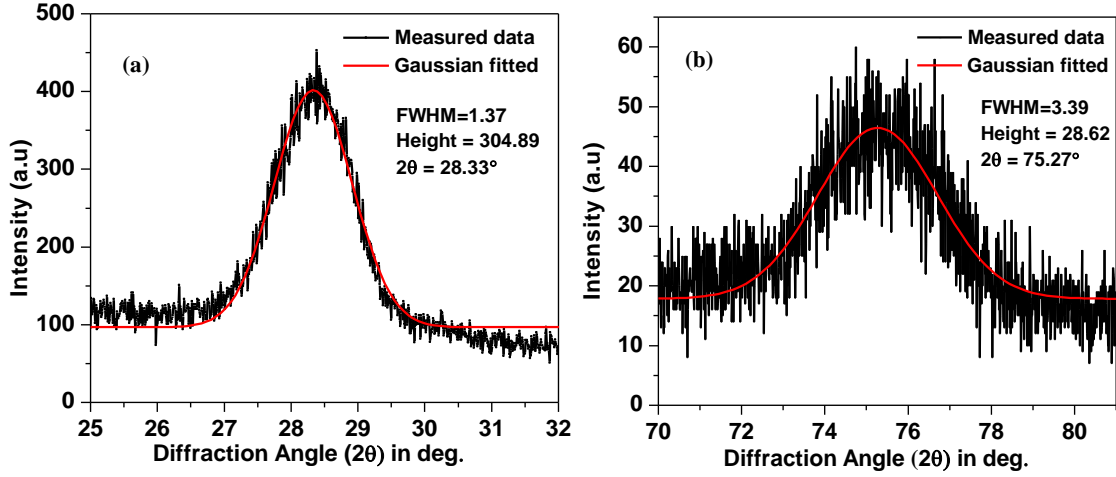


Figure 3.6: Magnified image of diffraction spectra of contaminated layer at (a) $2\theta = 28.3^\circ$ (b) $2\theta = 75.3^\circ$.

The aromaticity of the carbon layer also calculated by diffraction intensities of aromatic and aliphatic carbon peaks. The ratio of carbon atoms in aliphatic chains versus aromatic rings indicates aromaticity (f_a) of carbon layer [85]

$$f_a = \frac{A_{002}}{A_{002} + A_\gamma} \quad (3.3)$$

Where A_{002} and A_γ are the integrated intensities under (002) peak and peak due to aliphatic carbon which is generally present at $2\theta = 20^\circ$ in aliphatic carbon layer [85].

In synchrotron radiation induced layer deposited on LiF window $2\theta = 20^\circ$ peak is not observed. From this observation it is concluded that the aromaticity (f_a) of SR induced

carbon is close to one, it reveals that most of the carbon in the contamination layer is in the form of aromatic rings not in the form of aliphatic chains.

3.5 Chemical Analysis of Synchrotron Radiation Induced Carbon Layer

3.5.1 X-ray Photoelectron Spectroscopy:

Chemical analysis of synchrotron radiation induced carbon deposited on LiF window was done by X-ray photoelectron spectroscopy (XPS) using Al K_{α} (1486.6 eV) monochromatic X-ray source. XPS spectrum near carbon K-edge region (280 eV to 300 eV) was recorded by EA125 omicron analyzer with an energy resolution of 0.8eV. In order to compare chemical composites in contamination layer with respect to graphitic carbon, XPS spectrum of commercial graphitic carbon also recorded in same experimental conditions (shown in Figure 3.7). The surveys scan of XPS shows presence of carbon (1s) at 291 eV and oxygen (1s) at 532 eV in the contamination layer. Two broad peaks at 291 eV and 282.3 eV are observed in C (1s) binding energy region. XPS peak fit program [XPS PEAK 4.1] [88] was used for deconvolution of 291 eV peak. For data fitting the linear background was considered and peak fitting is carried with a mixture of Gaussian (80%) – Lorentzian (20%) functions. The 291 eV peak in the spectrum is deconvoluted into two sub component peaks at 291.6 and 290.6 eV.

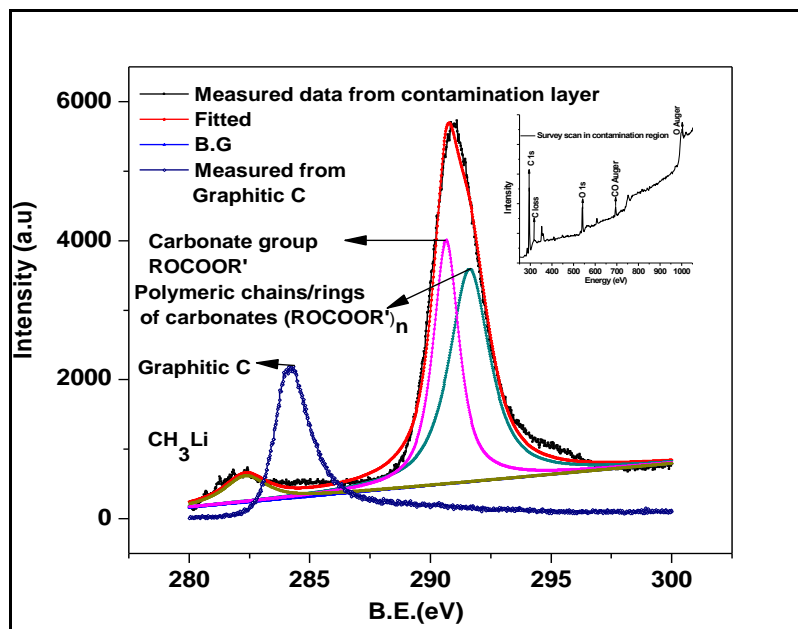


Figure 3.7: Carbon (1s) XPS spectra recorded using Al K_{α} (1486.6 eV) radiation source from carbon contaminated LiF surface and commercial graphitic carbon samples. Inset shows survey scan in 200 eV -1100 eV energy range.

The peak at 290.6 eV and 291.6 eV shows presence of oxygen and hydrogen in carbon layer. In separation studies of polymer bend of PMMA and polycarbonate Lhoest et al. [89] also observed similar photoelectron peak at 290.6 eV. They interpreted this 290.6 eV peak as C (1s) peak in bisphenol-A polycarbonate. In study of charging phenomena of polymeric film on gold surface Barth et al. [90] and Clark et al. [91] also interpreted the 290.7 eV peak as carboxylic form of carbon and diphenyl carbonate $(C_6H_5)OC(O)O(C_6H_5)$. The second peak at 291.6 eV was interpreted by several groups [92]–[94] as polymeric form of hydrogenated carbon that is dispersed in form of polymeric chains or rings (sp^2 hybridized carbon). Faradzhev et al. [82] studied carbonaceous layer deposited on TiO_2 thin film in presence of EUV radiation and n-tetradecane gas environment. They concluded that due to continuous EUV irradiation exposure alkane fragments form complex network by crosslinking of

dangling bonds of carbon and they observed that the film formed by EUV irradiation exposure of alkane have high content of sp^2 hybridized carbon. The peak at 282.3 eV indicates formation of methyllithium (CH_3Li) at the surface of LiF window. In methyllithium (CH_3Li) Meyer et al. [95] reported similar shift in C (1s) binding energy from 284.4 eV to 282.3 eV. Rajumon et al. [96] and Ocal et al. [97] also show slight shifts in C (1s) energy at different metallic surfaces, they observed carbidic state of Ti at 282.2 and 282.3 eV at Ti surface.

3.5.2 Raman Analysis of Synchrotron Radiation Induced Carbon Layer

Raman spectroscopy is very sensitive tool for carbon based materials. This technique is non-destructive technique and does not require any special specimen preparation for measurement. Raman spectra of synchrotron radiation induced carbon were recorded using $\lambda=441.6$ nm wavelength of Helium Cadmium (He–Cd) laser by Alpha 300SR Witec Instruments (GmbH Germany).

Raman spectrum of contamination layer deposited on LiF window was recorded and compare with commercial graphitic carbon (shown in Figure 3.8). The G (1556 cm^{-1}) and D (1350 cm^{-1}) bands of graphitic carbon and a broad hump in 2500 cm^{-1} to 3300 cm^{-1} region due to combination of overtones of G and D bands and stretching vibrations of CH_x ($x = 2, 3$) bond are observed [98]. The G and D peak positions are observed towards lower side compare to commercial graphitic carbon. As we have discussed G-and D-peaks positions depend on the sp^2 and sp^3 hybridized carbon contents, grain size, hydrogen contents and ta-C:H, a-C:H, nC-graphite phases of carbon in the sample, such as etc. The I(D)/I(G) ratio about 0.94, indicates highly disordered graphitic carbon phase. Full width half maxima (FWHM) of G peak of

contamination layer $\sim 123 \text{ cm}^{-1}$, the highly oriented graphitic carbon films have FWHM in $15\text{--}23 \text{ cm}^{-1}$ range. High value of FWHM of G peak reveals that the carbon layer is highly disordered or has nano-crystalline nature.

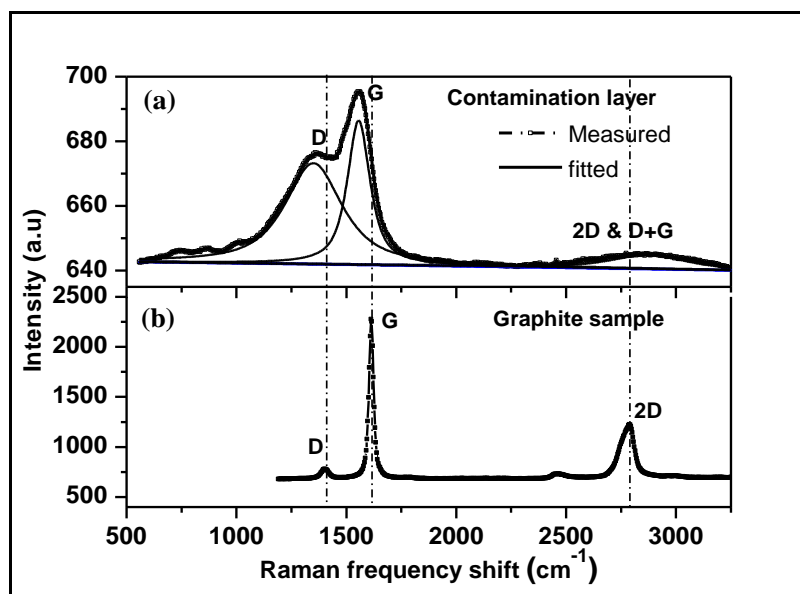


Figure 3.8: Measured and fitted Raman spectrum of (a) Synchrotron radiation induced carbon deposited on LiF window (b) Raman spectrum taken from commercial graphitic carbon.

Casiraghi et al. [99] observed that the hydrogenated carbon films that have G peak position at 1556 cm^{-1} and hydrogen contents about 15% are GLC:H type and the films that have D peak intensity to G peak intensity ratio ~ 0.94 are a-C:H type. The results of X-ray diffraction and Raman spectroscopy reveals that the contamination layer on LiF surface might be present in the form of rings of hydrogenated amorphous or nano-crystalline phase of carbon a-C:H (GLCH) with both sp^2 and sp^3 hybridization states.

In order to see the change in carbon layer characteristic with photon dose and energy twelve Raman spectra in 25 mm intervals from different locations along the length of the carbon contaminated mirror were acquired in the spectral region of $175\text{--}3600 \text{ cm}^{-1}$

with 4 cm^{-1} resolution. The measurement points on mirror surface and corresponding Raman spectra are shown in Figure 3.9 and Figure 3.10a respectively. Spectrum P-7 is recorded from the central region of mirror whereas P-1 and P-12 are recorded from near both the edges (along length direction). In order to analyze the spectra quantitatively, Raman spectra were fitted by convoluting two Lorentzian functions in the $900 - 2000\text{ cm}^{-1}$ Raman shift region. The spectra clearly show the G ($1575\text{--}1590\text{ cm}^{-1}$) and D ($1362\text{--}1380\text{ cm}^{-1}$) bands of graphitic carbon. These bands are generally present in most of hydrogenated graphitic carbon materials.

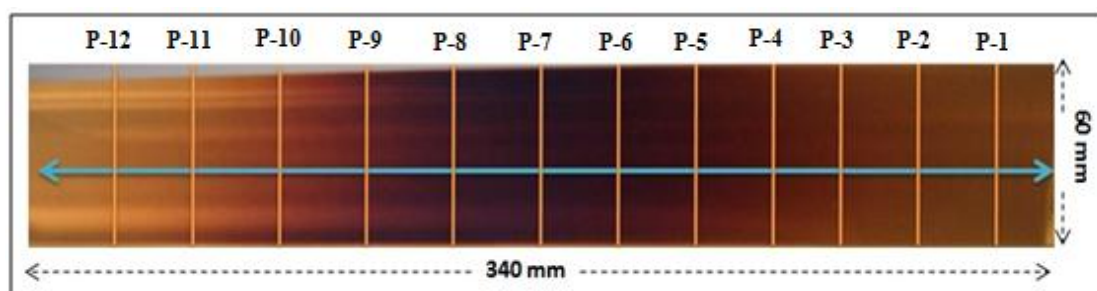


Figure 3.9: Carbon contaminated mirror, intersection point of vertical lines (orange color) and horizontal line (blue) indicates the Raman measurement point. The distance between the points is 25 mm.

Nano-crystalline graphite carbon Raman spectra generally shows G and D modes of vibrations. D mode is inactive in highly oriented graphite (HOG) and only becomes active in the presence of disorder [100]. The disorder mode at 1360 cm^{-1} (D-peak) is due to the A_{1g} symmetry mode at the K-point and caused by the disordered structure of graphene. At $\sim 1580\text{ cm}^{-1}$ the G-mode, is due to the E_{2g} symmetry mode at the Γ -point. The G-band originate from the stretching vibrations of the C-C bonds (sp^2) in graphitic carbon materials and is common to all sp^2 hybridized carbon structures whether they are arranged in rings (aromatic) or chains (aliphatic)); this mode does not

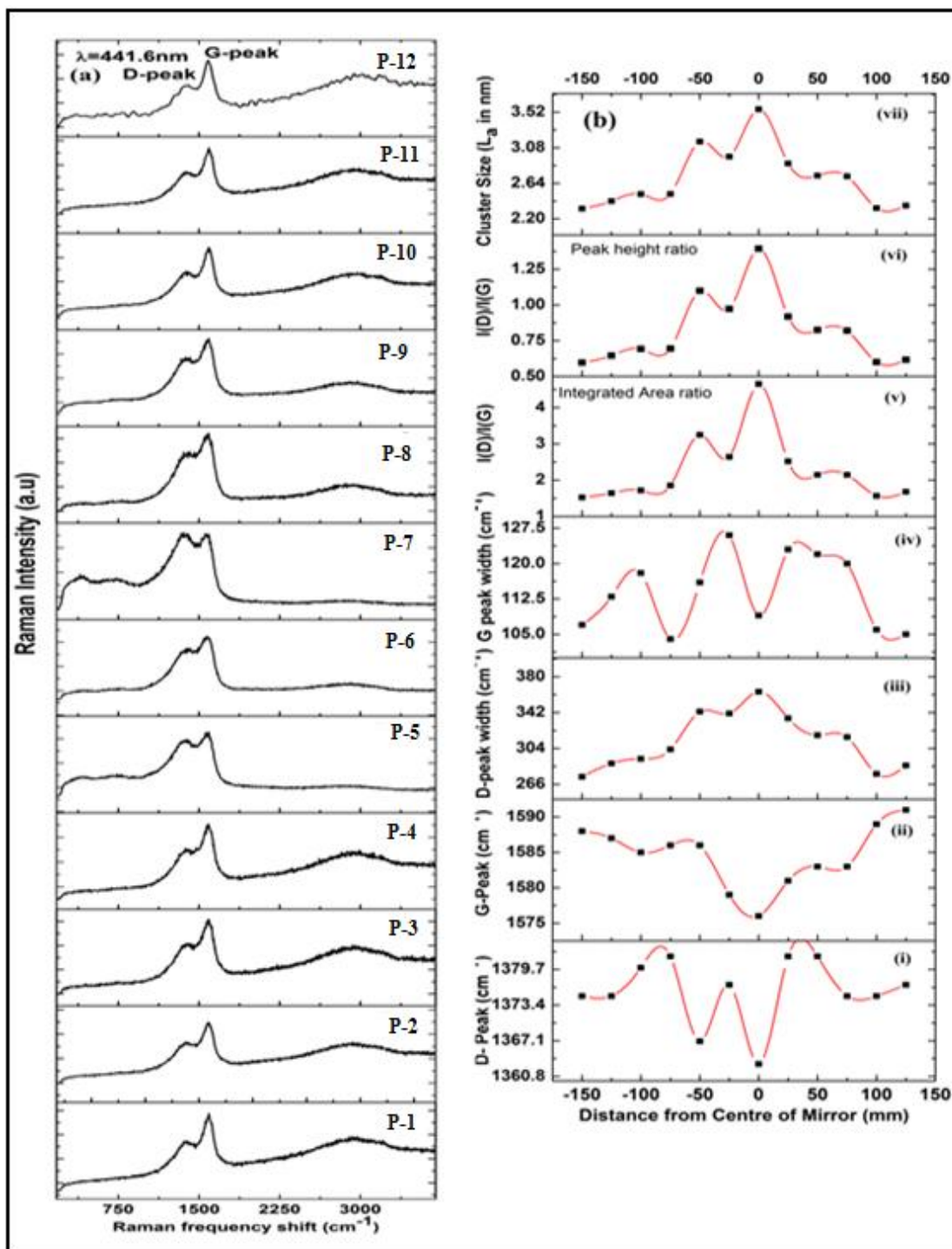


Figure 3.10: (a) Raman spectra (P-1 to P-12) from the surface of contaminated mirror, measurement points are shown in Figure 3.9. (b) corresponding D and G-peak positions (i-ii), D and G-peak width (iii-iv), I(D)/I(G) ratios (v-vi) cluster size (nm) (vii), calculated from Lorentzian fittings.

require the presence of six-fold rings. In UV excitation a peak at around 1060 cm^{-1} (T-peak) is seen in amorphous carbon. For visible excitation the cross section for amorphous sp^3 hybridized C-C vibrations is very less for visible excitation, thus its Raman signal can only be seen by UV excitation source [101]. The sp^3 hybridized carbon peak can be observed at 1332 cm^{-1} for significant amount of diamond phase in the samples. The Raman scattering cross section is 50 to 230 time higher for graphite (sp^2) and hydrogenated amorphous carbon (a-C: H) in compared to diamond carbon (sp^3) [100], [101]. Consequently, visible Raman spectroscopy can only probe the configuration of sp^2 sites. In a-C: H films where sp^2 and sp^3 hybridized carbon contents both are present and sp^2 clustering is affected by the sp^3 fraction, the sp^3 hybridized carbon fraction can be estimated by an indirect way. In synchrotron radiation induced carbon it is expected that the carbon layer deposited on optical elements may has mixer of sp^2 and sp^3 hybridized carbon atoms. It is also expected that sp^3 and sp^2 hybridized carbon fraction in contamination layer may vary by the interaction of photons and photoelectrons. The D and G peaks intensity ratio $I(\text{D})/I(\text{G})$, give qualitative estimation of sp^2 and sp^3 carbon bonding in the sample. The intensity of the disordered peak is directly connected to the presence of aromatic rings in the sample. For small grain/cluster size (L_a), the D-mode strength is proportional to the probability of finding a hexagonal ring in the cluster and that is also proportional to the cluster size. Thus, in amorphous carbon atoms the development of a D-peak intensity indicates ordering in graphitic carbon the layers, that is exactly opposite of the case of crystalline graphite. For nano-crystalline materials the D and G peak intensity ratio is inversely proportional to the in-plane cluster size:

$$L_a \text{ (nm)} = \frac{C}{E^4} [I(G)/I(D)]$$
 [102], [103] this relation is no longer valid for amorphous and hydrogenated amorphous carbon atoms. The modified relation $[I(D)/I(G)] \propto L_a^2$ for cluster size in amorphous carbon materials was proposed by Ferrari & Robertson [101], [102]. The height of D-peak has information about the ordered aromatic rings and the width has information about disorder aromatic rings. So, with the increase of sp^2 -C sites in hydrogenated amorphous carbons (a-C: H), the D-peak height increases on the other hand peak width increases/decreases it depend on the ordering/disordering of the sp^2 sites in the layer. Thus, the peak height is more sensitive to a change in disorder compared to peak area. From data fittings of measured spectra in $900\text{--}2000 \text{ cm}^{-1}$ region, we calculated the G and D peak positions, its widths and intensity ratios from both peak heights and integrated area under the peaks. Using $I(D)/I(G)$ ratio, in-plane cluster size of carbon atoms is also estimated. The distance from center point (P-7) versus estimated quantities (G and D peak positions and width, $I(D)/I(G)$ ratio, cluster size) are plotted in Figure 3.10b. The distribution of photon dose follows Gaussian distribution law. The graphs in Figure 3.10b (v) and Figure 3.10b (vi) reveals that as measuring position move on mirror surface from P-1 to P-7 (lower to higher photon dose) the peak height ratio increases from 0.6 to 1.4 and the integrated peak areas ratio $I(D)/I(G)$ increase from 1.5 to 4.5. The $I(D)/I(G)$ ratio is an important parameter by which ordering and disordering in amorphous carbon and crystalline or nano-crystalline carbon material can be estimated. The integrated area intensity ratios and peak height ratios of D and G peaks increases with same trend with different magnitude. The $I(D)/I(G)$ ratio mainly increases by formation of new sp^2 sites in the layer or it can say that sp^3 sites are

convert into sp^2 sites by interaction with photon/photoelectron and arrange in the form of hexagonal rings in the layer. The process can be understood as follows: when hydrocarbon molecules are adsorbed on mirror the surface they probably form large chains of hydrocarbon molecules, with the carbon atoms in both sp^3 and sp^2 hybridization states (ta-C:H and a-C:H) in adsorbed layer with less number of sp^2 sites in aromatic rings. When SR photons interact with these adsorbed hydrocarbon molecules the C-H, C-C and C-O bonds break and dangling bonds are formed by abstraction of oxygen and hydrogen gases. The dangling bond containing carbon atoms are highly reactive and they crosslinks to each other and form long chains and hexagonal rings with sp^2 hybridized carbon. From edge of mirror to central region on mirror surface, the photon dose increases, the probability of bond breaking and formation of new dangling bonds is more in the central region (P-7), and resultant the probability of the formation of hexagonal rings (sp^2 sites) increases, resultantly D to G peak intensity ratio increases. The increase in D-band width indicates that the hexagonal rings are not perfectly ordered in the cluster, this indicates that with increase in photon dose disordering in the carbon layer increases. The in-plane cluster size at all twelve measurement points is calculated by use of the modified Tuinstra & Koenig relation [100]. Increment in the cluster size (23 Å to 35 Å) is observed by increase in the photon dose. From these observations it can be concluded that, with increase in photon dose, disordering, sp^2 sites or hexagonal rings, and inplane cluster size in the deposited carbon layer increase. Faradzhev et al. [82] also proposed a similar carbonaceous product reaction deduced from valence-band and GC-MS (Gas Chromatography-Mass Spectrometry) spectroscopic measurements made after EUV irradiation of adsorbed n-tetradecane on TiO_2 thin film.

Figure 3.10b (i) and (ii) show red shift in the G- and D-peaks from the off-center region (P-1 and P-12) to the central region (P-7). G- peak position vary from 1590 to 1576 cm^{-1} and D-peak positions vary from 1375 cm^{-1} to 1363 cm^{-1} . The dispersion in the G- and D-peaks depends on various parameters such as the sp^2 and sp^3 hybridized carbon concentration, hydrogen concentration and cluster size. Different phases of carbon, such as ta-C:H, a-C:H, nC-graphite etc. also show different peak positions in Raman spectra. In the edge region where the photon dose is lesser, there may be the co-existence of hydrogenated tetrahedral amorphous carbon (ta-C:H) and hydrogenated amorphous carbon (a-C:H) with high concentration of hydrogen. In the central region, due to the high photon dose, more hydrogen abstraction occurs, resultantly the concentration of hydrogen decreases and the nature of the layer vary from ta-C:H to a-C:H or a-C with the formation of hexagonal rings, resultantly the G and D-peaks positions shift towards the lower side. When the nature of the film changed from ta-C (85% sp^3 -C) to a-C (20% sp^3 -C) Ferrari & Robertson [102] also observed red shift in the G-peak position. Red shift in G-peak position from 1587 to 1581 cm^{-1} also observed by Gupta et al. [104] by increasing the number of graphene layers from 1 to 20 layers. Due to the conversion of C-H bonds into C-C bonds by hydrogen abstraction in higher dose region (P-7) the carbon layer thickness is expected to be higher in comparison to edge region (P-1 and P-12). In central region the thickness of the carbon layer is about 400 Å (discussed in section- 3.3). In 2500 cm^{-1} to 3300 cm^{-1} region second-order Raman effect in all twelve locations is also observed. The source of this broad peak is the combined effect of overtone of G, D and G+D modes and CH_x stretching vibrations modes. In polymeric a-C:H film Ferrari & Robertson [102] detected CH_x stretching modes at 2920 cm^{-1} by UV Raman

spectroscopy. This broad peak (2500 to 3300 cm^{-1}) gives an indication of the presence of C-H bonds in the layer.

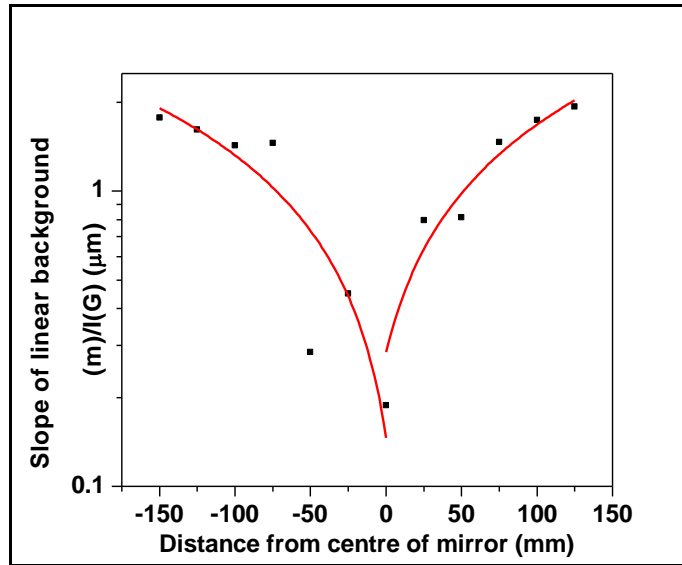


Figure 3.11: Plot of ratio of the slope (m) of the linear background of Raman spectrum to the G-peak intensity as a function of distance from the mirror center.

However, photoluminescence background in visible Raman spectroscopy is also give signature of hydrogen contents. The photoluminescence background increases with increasing hydrogen contents. This is due to hydrogen saturation of non radiative recombination centers. For hydrogen contents over 40–50% usually screen the Raman signal of hydrogenated amorphous carbon (a-C: H) samples [99], [105]. Casiraghi et al. [99] studied presence of hydrogen in a-C: H thin films deposited by different thin film deposition techniques such as distributed electron cyclotron resonance (DECR), plasma-enhanced chemical vapor deposition (PECVD) and electron cyclotron wave resonance (ECWR) with different process gases such as methane, ethane etc. They estimated hydrogen contents by the ratio of the slope (m) of the fitted linear background to the intensity of the G-peak [$m/I(G)$]. They reported that, when $m/I(G)$

ratio increases from 0.6 mm to 15 mm the hydrogen content in the film increases from approximately 15% to 45%. For carbon contamination layer the m/I(G) ratios for all Raman spectra from P-1 to P-12 is shown in Figure 3.11. The m/I(G) ratio, which is an indication of presence of hydrogen contents in carbon layer continuously increases from central region (P-7) to outer region (P-1 and P-12). If we compare these results with results of Casiraghi et al. [99], it is observed that the carbon contamination layer shows a deviation in atomic H content from 25% to 15%. Hydrogen contents in the central region decreases due to high photon dose in this region. High number of photons breaks high number of C-H bond resultant concentration of hydrogen in central region decreases.

In both the samples it is observed that carbon is present in the form of graphitic carbon but X-ray diffraction pattern of carbon layer deposited on LiF show an extra phase of carbon (poly diamond) that is may be due to different exposure energy and the different hydrocarbon environment in vicinity of mirror and LiF window. In case of carbon deposited on LiF window surface the cracking of hydrocarbons occurs by 3 eV to 11 eV photons energy in 10^{-6} mbar pressure environment whereas carbon deposition on Au mirror surface occurs in 10^{-9} mbar pressure with photon energies starts from IR to soft x-ray.

3.6 Summary

In summary we can say that carbon in the contamination layer present in both sp^3 and sp^2 hybridized states and its properties vary with incident photon dose and energy. In low photon dose region the numbers of aromatic rings (sp^2 -C) are less, and in high photon region sp^3 hybridized carbon sites converting into sp^2 hybridized carbon sites

and more aromatic rings are formed. The carbon on the mirror surface is in the form of small clusters, the size of the clusters increases with photon dose. In high photon dose region, $I(D)/I(G)$ ratio and D- peak width is high which indicates that the number of rings in the cluster and disordering in the cluster increases. The ratio of the slope (m) of the linear background of Raman spectrum to the intensity of the G-peak [$m/I(G)$] reveals that in the layer hydrogen contents decreases with photon dose. In central region (P-7) hydrogen content are lower in comparison to outer region (P-1 and P-12) of mirror.

4 Refurbishment of X-ray Optics by Capacitive Coupled RF Plasma

4.1 Overview

Reflective optics used in synchrotron beamlines requires precise coatings on premium quality substrate. Substrate preparation and precise coating are expensive and time consuming process. Prolonged use of optics in beamlines under high photon intensity results in deposition of carbon contaminations on optics surface. Carbon contaminations on optics surface reduce photon flux pass through the optics. To regain optics performance, optic refurbishment is a cost effective and efficient solution. The selection of refurbishing technique should be such that after refurbishment the reflective layer should not get damaged and optics regains the desired performance after the cleaning process. For optics refurbishing several techniques such as capacitively coupled rf plasma, UV and IR laser are generally used (discussed in chapter-2). In this chapter results of mirror cleaning experiments using the capacitive coupled rf plasma are discussed. Plasma technology is relatively new emerging field in surface science and is matter of intense research. The plasma based technologies offers distinct advantages over other conventional technologies. The most important use of plasma in the domain of surface treatment is surface activation/ modifications (etching), deposition and polymerization etc. Depending on type of plasma and its parameters the plasma can modify surfaces in various ways. In plasma etching, material from the surface of object is removed either by physical or chemical means [106], [107]. In etching applications, material selectivity, uniformity and anisotropy

are important parameters [108], [109]. Depending on end use of plasma, different types of discharge configurations such as dc discharge, rf discharge (capacitive or inductively coupled), electron cyclotron resonance discharge etc. are commonly used. Because of low cost and uniformity over a large surface area, low frequencies (13.56 MHz) capacitive coupled plasma (CCP) discharges are popular for surface treatment and surface cleaning applications. We have used this technique for removing carbon from Au coated thin film and finally the technique is applied to the actual optics. Capacitively coupled rf plasma cleaning procedure and results of cleaning using this technique are discussed in this chapter.

4.2 Refurbishment of Carbon Contaminated X-ray Mirrors

Two carbon contaminated mirrors were taken from synchrotron beamlines for refurbishing using rf plasma, one mirror (toroidal) was removed from reflectivity beamline (BL-04) of Indus-1, that is in used in the beamline since 2001 and the second mirror (spherical) was removed from reflectivity beamline (BL-04) of Indus-2, that is in used in the beamline since 2013.

4.2.1 Cleaning of Carbon Contaminated Toroidal Mirror using RF Plasma

Synchrotron radiation induced carbon contaminated gold mirror was refurbished by capacitively coupled rf plasma exposure. The detail description about the system used for plasma exposure and its optimization results are given in chapter-2. The carbon contaminated toroidal shape mirror has a $\sim 406 \text{ \AA}$ thick layer of carbon in central region and layer thickness reduces gradually towards both ends of the mirror (shown in Figure 4.1). The characteristics of this carbon layer are discussed in chapter-3 and it is concluded that the carbon in contamination layer present in both sp^3 and sp^2 phases

and layer properties vary from ta-aC:H to GC:H. Several groups used different kinds of plasma for removing carbon contamination from different surfaces. It is observed that capacitively coupled rf plasma and downstream inductively coupled plasma sources are suitable for removing graphitic carbon from optics surface without any surface damage [34], [35], [110], [111].

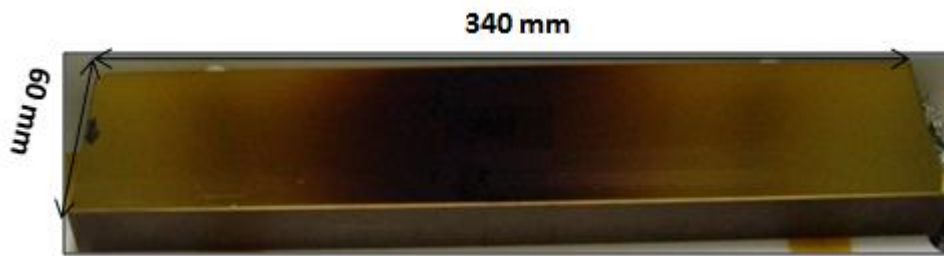


Figure 4.1: Carbon contaminated toroidal gold mirror taken from reflectivity beamline (BL-04) of Indus-1 for carbon cleaning experiments.

For carbon cleaning the contaminated mirror was kept on the ground electrode which is separated by a distance of 70 mm from powered electrode. The dimensions of electrodes are 300 mm \times 100 mm \times 5 mm. The electrodes assembly housed in a vacuum chamber and electrically isolated from rest of the chamber. Before starting the cleaning process ultimate vacuum of 10^{-7} mbar was achieved using turbo-molecular pump. In symmetric configuration of capacitively coupled plasma systems the ions have energy of the order of plasma potential (10 V- 20 V), which is below the sputtering threshold energy for most of the metals [112]. In atmospheric pressure plasma jet (APPJ) cleaning technique Kim et al. [113] observed increase in surface roughness by particle aggregations and by direct hitting of ions on a metal surface. For avoiding any direct collisions of ions to mirror surface which may lead to surface increase in surface roughness, the reflecting surface of mirror is kept perpendicular to

the surface of electrodes. For plasma generation a mixer of argon and oxygen gases (1:1) is used. The process pressure in $3\text{-}5 \times 10^{-2}$ mbar range was set by adjusting the pumping valve and inlet gas flow. The flow of gases was controlled by mass flow controllers and flow rate is kept at ~ 20 sccm for both the gases. A 10 W (33.3 mW/cm^2) rf power was fed to electrode using an impedance matching network. Similar optimized parameters was also obtained by Wang et al. [114] while studying the effect of rf plasma cleaning on GaAs substrate.

During cleaning process optical emission lines of carbon monoxide (CO) and oxygen (O) from plasma are recorded by optical emission spectrometer (Make Avantes Inc.). The estimation of time taken for carbon cleaning from the contaminated mirror surface was judged by observation of optical emission spectral (OES) intensities of CO and O lines/bands and visual inspection of mirror surface during plasma exposure.

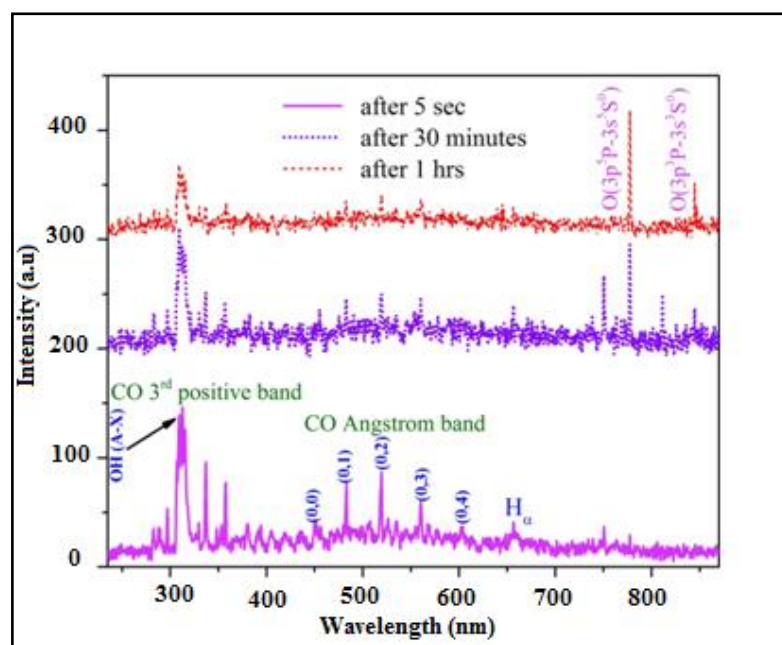


Figure 4.2: Optical emission spectrum recorded at different time during cleaning of carbon contaminated mirror by rf plasma exposure.

Figure 4.2 shows the intensity spectrum in the wavelength span of 250 nm to 900 nm recorded by OES during rf plasma exposure, the spectrum contains both Angstrom and third positive band of CO and band of oxygen atomic transitions. The reduction in the intensity of vibrational transition of second and third positive molecular band of CO with plasma exposure time indicates the decrease in concentration of CO molecule from plasma volume. The emission spectrum recorded in the beginning of cleaning experiment shows high intensities of CO third positive band (380 nm - 260 nm) and Angstrom band (660 nm - 410 nm) and low intensity of oxygen atomic transitions at ~778 nm and ~842 nm for $3p^5P$ to $3s^5S$ and $3p^3P$ to $3s^3S$ transitions respectively, because most of the oxygen is consumed in reaction with carbon which results in CO molecule formation. When exposure time increases to half an hour intensity of atomic oxygen transitions increases and CO Angstrom band intensities decrease to nearly background level but CO third positive band intensities are still present. Spectrum recorded after one hour exposure clearly indicates that emission line intensities of both the bands of CO are decreased to background level and oxygen intensities increased due to decrease of formation of CO molecule after complete removal of the carbon contamination layer. When emission lines of CO decreases to background the mirror visually inspected and the process was stopped and mirror was removed from the system. Photograph of refurbished mirror after plasma exposure is shown in Figure 4.3. Krstulovi et al. [115] observed similar decrement in intensities of CO 3rd positive band and Angstrom band and increment in intensity of oxygen atomic transitions during 50 sec to 140 sec of inductively coupled rf plasma exposure of 23 μm thick polyethylene terephthalate (PET) film.

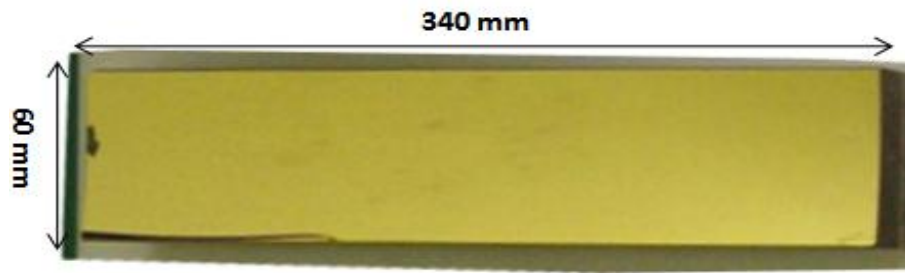


Figure 4.3: Refurbished gold coated toroidal mirror after rf plasma exposure for one hour.

In plasma cleaning technique carbon from optics surface is removed by synergetic effect of electrons, ions and UV light. The plasma cleaning/etching is a three steps process, in first step when a contaminated surface immersed into plasma, the plasma species such as photons, electrons and ions interacts with contaminant molecules adsorbed on surface and transfer energy to the adsorbed molecules, resultant chemical bonds (C-H, C=C, C-C, C=O etc.) of organic molecules breaks. Due to bond breaking the complex molecules convert into low molecular weight molecules with formation of new dangling bonds (the process is known as surface activation). In second step, reaction among activated contamination molecules and reactive species present in plasma (in case of oxygen plasma O_2^+ , O_2^- , O_3 , O , O^+ , O^- , ionized ozone, meta-stable excited oxygen etc.) take place at the surface of the object and turned them into volatile compounds like CO, CO_2 and CH_4 , etc. In third step the gaseous product are swept out from the plasma chamber by evacuation system. The resulting surface has ultra clean quality. After cleaning the mirror surface was characterized by surface analysis techniques and their results are discussed below.

4.2.2 Cleaning of Carbon Contaminated Spherical Mirror using RF Plasma

For removing carbon from spherical mirror surface the contaminated mirror was kept between the electrodes, here the electrode assembly is kept horizontal and mirror surface is kept perpendicular to the electrodes surface the other parameters were kept nearly same as previous case. In order to avoid heating effect on mirror surface the mirror was exposed to rf plasma in four successive stages for more than four hours. Images of mirror before and after cleaning are shown in Figure 4.4.

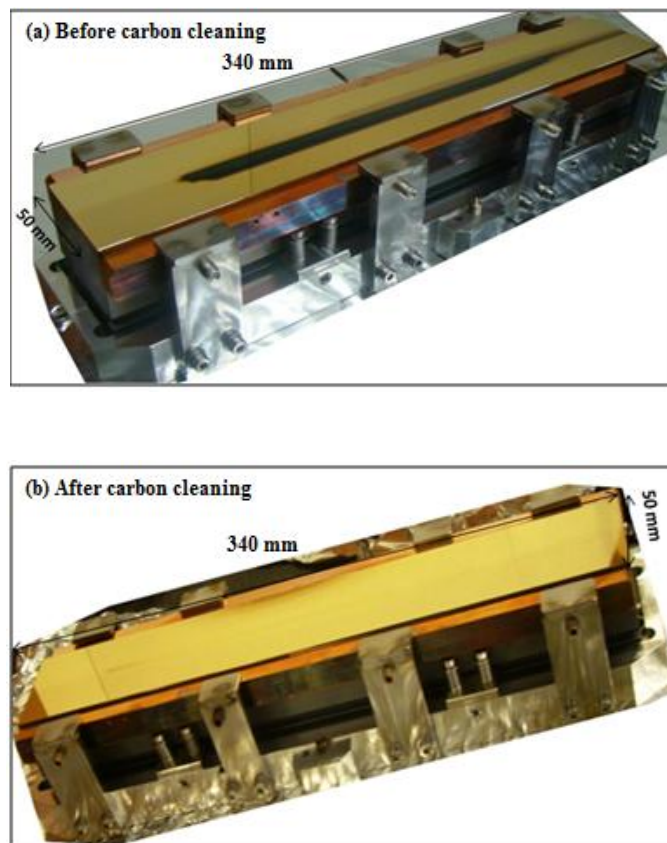


Figure 4.4: Gold coated spherical mirror (a) before and (b) after plasma exposure.

Black strip on mirror surface shows presence of carbon before exposing the mirror in plasma. After plasma exposure the black strip completely disappear from mirror

surface. For avoiding long shutdown period of beamline surface characterization was not done for this mirror and the mirror was reinstalled in the beamline in a minimum access time.

4.3 Analysis of Toroidal Mirror Surface before and after Plasma

Exposure

The primary condition of any optics refurbishing technique is that the structural and optical parameter should not change after refurbishment. So it is very important that after refurbishing the mirror its structural and optical parameters should be compared. The surface of mirror after plasma exposure was analyzed by Soft X-ray Reflectivity, Raman Spectroscopy and Atomic Force Microscopy measurements.

4.3.1 Structural Analysis and Reflectivity Gain of X-ray Mirror after Plasma

Exposure

Before and after plasma exposure, soft x-ray reflectivity (SXR) measurements at Indus-2 reflectivity beamline (BL-03) were carried out for determination of structural and optical parameters of Au and C layers. The angle dependent reflectivity measurements were performed at the center of the mirror (dense contamination region) using 1200 eV photon energy. The reflectivity spectra were fitted using the Parratt recursive formalism [83]. Measured and fitted reflected intensity versus momentum transfer spectra are shown in Figure 4.5. The critical momentum transfer of carbon and gold are indicated by vertical dashed lines in Figure 4.5. In reflectivity pattern a clear dip at critical momentum of carbon of contaminated mirror indicates the presence of carbon on mirror surface. The structural (thickness and roughness)

parameters and optical constant (δ and β) values are estimated from the data fittings of reflectivity curves. For data fittings, optical constants (δ and β) values for gold (Au), graphitic carbon (GC), chromium (Cr) and silicon dioxide (SiO_2) are taken from the Henke database [27]. For the data-fitting, the optical constant (δ and β) values for gold (Au), chromium (Cr) and the substrate (SiO_2) were kept as constant, while structural parameters (thickness, roughness) of carbon, gold and chromium layer and optical constants (δ and β) of carbon layer were kept as free (variable) parameters. The values of optical constants $\delta(\omega)$ and $\beta(\omega)$ of carbon contamination layer at $\lambda=10.3 \text{ \AA}$ were estimated 2.57×10^{-4} and 2.86×10^{-5} respectively from best fittings of reflectivity curve of carbon contaminated mirror. The optical density of carbon layer is estimated about 75% of graphitic carbon. Contamination layer thickness and roughness of carbon contamination layer were estimated 390 \AA and 40 \AA respectively. The slight variation in layer thickness and roughness is expected from previous one because deposition of layer is not uniform and during reflectivity measurement the location of the beam may be slightly different from previous location.

The best fit results of reflectivity curve of carbon cleaned mirror after plasma exposure show a low density thin layer of about 9.5 \AA thickness and 4.5 \AA surface roughness. Raman spectra do not show presence of carbon on mirror surface (see in Figure 4.8) and optical constants values of this thin layer also not matches with carbon optical constants. These observations reveal that this low density thin layer on mirror surface may be due to adsorption of atmospheric gases. The best fit values of thickness, roughness and optical constants are tabulated in table-4.1. After carbon cleaning, Au layer surface roughness was estimated 17 \AA , which is nearly equal to the

surface roughness value (16 Å) estimated before the cleaning the mirror. The tabulated value of surface roughness clearly indicates that after carbon removal the mirror surface decrease from 40 Å to 17 Å.

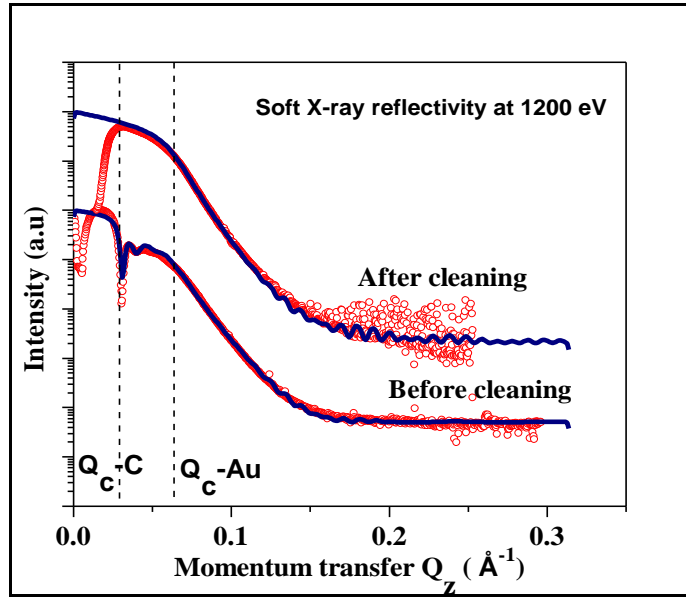


Figure 4.5: Measured (open circles) and fitted (continuous lines) soft x-ray reflectivity spectra taken before and after the removal of carbon contamination layer. Vertical dashed lines indicate the position of critical momentum transfer (Q_c) for C and Au.

Table - 4.1: Structural parameters [thickness (t), roughness (σ)] and optical constants (δ and β) of carbon, gold and chromium layers of carbon contaminated mirror before and after plasma cleaning obtained by the fitting of soft x-ray (1200 eV) reflectivity data.

Elements	Before cleaning				After RF plasma cleaning			
	t(Å)	δ	β	σ (Å)	t (Å)	δ	β	σ (Å)
C	390	2.57E-04	2.86E-05	40	9.5	2.01E-04	1.86E-05	4.5
Au	500	1.36E-03	5.45E-04	16	500	1.36E-03	5.45E-04	17
Cr	90	9.32E-4	2.73E-4	5	90	9.32E-4	2.73E-4	5
Substrate(SiO ₂)	Bulk	3.09E-4	3.54E-5	5	Bulk	3.09E-4	3.54E-5	5

To see cleaning effect on the reflectivity of mirror after plasma cleaning the energy dependent reflectivity in 750 eV to 1500 eV energy range at 2 degree incidence angle was measured before and after plasma cleaning. The energy dependent reflectivity spectrum of contaminated mirror clearly shows two minima at ~825 eV and ~1000 eV (shown in Figure 4.6a). These minima are due to interference effect of the carbon layer. On energy scale, position of minima depends on carbon layer thickness and incidence angle of beam. For a fixed incidence angle, the position of minima shifts towards higher/lower energy side as thickness of carbon layer decrease/increase. After cleaning the mirror, the interference effect of carbon layer or the reflectivity losses at 825 eV and 1000 eV disappeared indicating that after plasma exposure, carbon layer is removed from the surface of mirror. The fractional change in reflectivity $\Delta R = \left(\frac{R_{aftercleaning} - R_{before cleaning}}{R_{before cleaning}} \right)$ show that maximum change in reflectivity occurs at 825 eV (Figure 4.6b). Taking tabulated structural values of gold, chromium layer thicknesses, surface roughness and density of materials the reflectivity of plane gold mirror was simulated in 750 eV to 1500 eV energy range by labview based program [84] and compared with the measured reflectivity shown in Figure 4.6a. It is observed that the best simulated values have slightly higher value of surface roughness and angle of incidence which is under uncertainty values of reflectivity measurements. A slight variation in reflected intensity is expected be due to curvature in mirror surface.

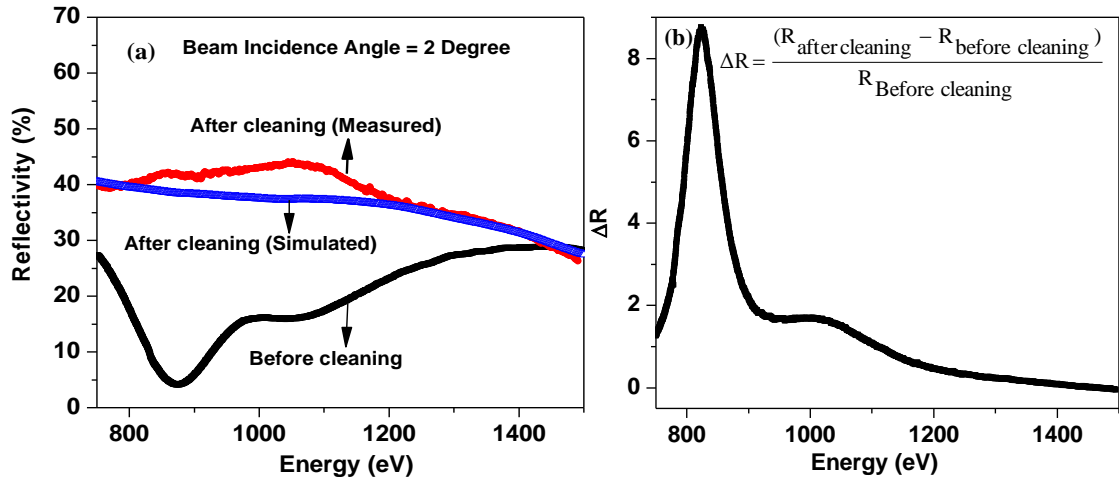


Figure 4.6: (a) Energy (750 eV to 1500 eV) dependent soft x-ray reflectivity of mirror before and after rf plasma cleaning at 2 degree incidence angle (b) Change (ΔR) in soft x-ray reflectivity after plasma cleaning.

4.3.2 Surface Morphology before and after Plasma Exposure

Surface morphology of mirror before and after plasma cleaning was imaged by atomic force microscopy (AFM). Quantification of surface roughness of mirror surface was done by AFM and XRR measurements. AFM measurements were carried-out by Keysight 5600LS AFM machine in non-contact mode. In non-contact mode the surface topography is imaged by sensing attractive forces (Van der Waals type) between cantilever tip and the surface of sample. For comparison of surface morphology and surface roughness before and after carbon cleaning three dimensional (3D) AFM morphology images of mirror surface were recorded nearly in the same region on mirror surface. The 3D images of the mirror surface before and after the plasma cleaning are shown in Figure 4.7. A slight variation in surface morphology with decrease in root mean square (rms) roughness from 28 Å (roughness of carbon contaminated region) to 24 Å is observed after the plasma cleaning. The soft x-ray

measurements also show decrease in surface roughness from 40 Å to 17 Å after plasma exposure. The discrepancy in the roughness value measured by AFM and SXR techniques is due to different area averaging (in SXR averaged area in mm² whereas in AFM it is in μm²) covered by two distinct measuring probes. Specular x-ray reflectivity probes the buried interface and gives averaged density profile along the vertical direction while the AFM can probe only the top surface and probe only local area.

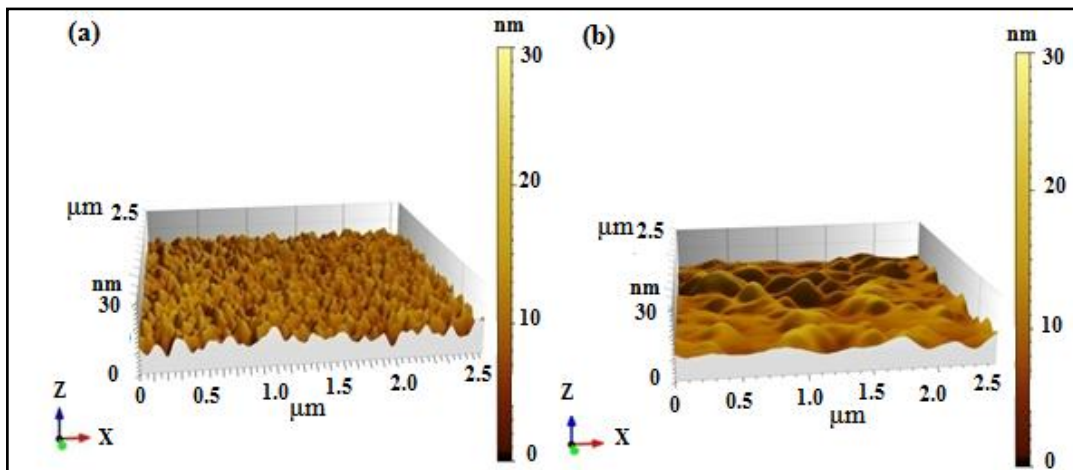


Figure 4.7: Three dimensional atomic force microscopy images (2.5μm × 2.5μm) (a) before and (b) after cleaning the mirror. AFM images clearly indicate that surface topography of mirror changes after carbon cleaning.

4.3.3 Raman Spectra of Mirror Surface before and after Plasma Exposure

Before and after carbon cleaning by plasma exposure Raman spectra were recorded from mirror surface at room temperature using Alpha 300SR Witec Instruments (GmbH Germany). The system consist of He-Cd laser ($\lambda= 441.6$ nm) as an excitation source. Single mode optical fiber was used for delivering 441.6 nm light to the microscope. Figure 4.8 shows the Raman spectra before and after cleaning the mirror.

These spectra were recorded from twelve distinct locations (P-1 to P-12) along the mirror length with an interval of 25 mm along the length of mirror (as discussed in chapter-3). The Raman spectra recorded from contaminated mirror surface before cleaning distinctly shows graphitic carbon G (1575-1590 cm^{-1}) and disordered graphitic carbon D (1362-1380 cm^{-1}) Raman peaks (see in Figure 4.8). These peaks are generally present in all poly-aromatic hydrocarbons. The disordered mode (D) at about 1360 cm^{-1} is due to A_{1g} symmetry mode at the K-point of Brillouin zone. Raman spectroscopy is one of the most sensitive tool for characterize disorders in graphitic (sp^2 hybridized) carbon materials. The presence of disorder in sp^2 hybridized carbon systems results in resonance Raman spectra. D-mode is inactive in perfect graphite systems and only becomes active in the presence of disorder [100]. The G-mode at $\sim 1580 \text{ cm}^{-1}$ is due to E_{2g} symmetry at the Γ -point of Brillouin zone. G-band is common to all sp^2 hybridized carbon systems whether they are present in the form of hexagonal rings or linear chains. This mode is arises from the stretching vibrations of the C-C bonds in sp^2 hybridized graphitic carbon materials and does not require the arrangement of six fold hexagonal rings. G and D both bands of graphitic carbon are completely absent in Raman spectra recorded from plasma exposed mirror surface, this indicates that by plasma exposure the carbon contamination from mirror surface is completely removed.

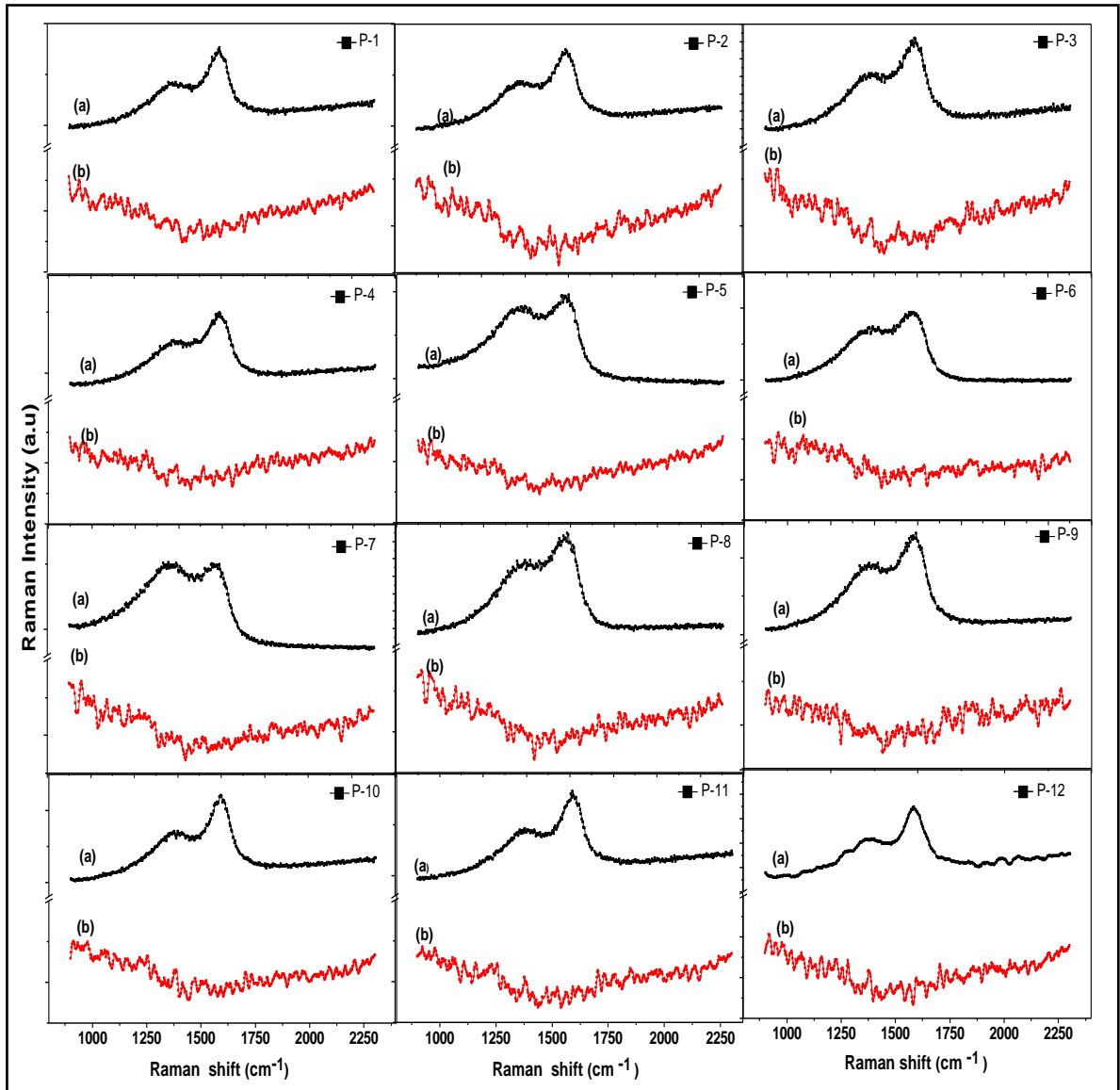


Figure 4.8: Raman spectra (a) before (black) and (b) after (red) plasma exposure from mirror surface. P-1 to P-12 indicates measurement points on mirror surface in interval of 25 mm along the length of mirror.

4.4 Summary

Refurbishment of carbon contaminations mirror without altering surface properties is a challenging task. Carbon contamination layer from a gold coated toroidal mirror

(TM) surface was successfully removed by exposing the mirror to capacitively coupled rf plasma. The contaminated mirror was exposed to rf plasma for approximately one hour at pre optimized parameters. In order to monitor the cleaning process optical emission lines of carbon monoxide and oxygen from the plasma were recorded during the cleaning process. Before and after plasma cleaning the mirror surface was characterized by different surface analysis techniques (Raman spectroscopy, SXR and AFM). The disappearance of 'G' and 'D' bands of graphitic carbon in Raman spectra after plasma exposure indicates the absence of carbon layer on mirror surface. Moreover, the disappearances of dip in soft x-ray reflectivity near the carbon critical momentum, which also shows absence of carbon layer. From analysis of reflectivity data it is concluded that the surface roughness of the Au layer remains same before and after rf plasma exposure. AFM measurements also show a decrease in surface roughness from 28 Å to 24 Å. Energy dependent x-ray reflectivity in 750 eV to 1500 eV energy range improved significantly. Finally we conclude that the carbon contaminated layer was successfully removed by rf plasma exposure without affecting mirror surface properties.

5 Refurbishment of X-ray Optics by Ultra Violet Radiations

5.1 Overview

Use of ultraviolet (UV) light is an effective method for removing variety of contaminants from surfaces. Non-destructive nature of UV radiations and its high dissociation cross section for organic contaminants (hydrocarbons), make the technique very useful for removing carbon contaminations from optics surfaces. Different types of UV radiation sources that can be used for hydrocarbon cleaning are given in Appendix-III. Average chemical bond dissociation energies for hydrocarbon molecules lies in 3.5 eV to 8.5 eV energy range [116], [117]. First time Bolon and Kunz [39] investigated the ability of UV radiations to de-polymerize photo-resist polymers and showed that UV de-polymerization produces an extremely clean surface. This method is simple, dry and cost effective and no need of specific environment such as vacuum, low/high temperature but in some cases it is observed that at increase in temperature and lowering in pressure (0.1 to 0.01 atmospheric) increase the contamination removal rate [39],[51]. Jellison [118] showed that long time UV exposure is highly effective in the cleaning of organic contaminants from gold surface. Sowell et al. [119] cleaned gold contacts and glass slides in ambient environment as well as at 10^{-4} mbar pressure of oxygen by UV exposure of 15 hrs. The effectiveness of techniques depends on certain parameters such as wavelengths emitted by UV source, distance between source and sample and irradiation time. Carbon contamination removal from SR beamlines optical components is of special

interest to retrieve the original optical performance. Kumar et al. [120] restored the blaze angle and absolute diffraction efficiency (ADE) of carbon contaminated variable line space (VLS) grating after cleaning by oxygen radicals generated by dissociation of oxygen molecules using VUV radiation ($\lambda = 172$ nm). UV/VUV sources can be used for both *in-situ* and *ex-situ* optics cleaning in beamlines. For *in-situ* cleaning, zero order synchrotron radiations (white beam) can be used as UV radiation source. *In-situ* cleaning technique is more suitable where optics are mounted in complex housing and difficult to remove from the beamline. Toyoshima et al. [9] used zero-order synchrotron radiation for optics cleaning in vacuum ultraviolet (VUV) and soft x-ray undulator beamline (BL-13A) at the Photon Factory at Japan. Hamamoto et al. [42] used this technique to remove the contaminations from Mo/Si multilayer optics. Tanaka et al. [53] cleaned carbon contamination from Schwarzschild optics using 172 nm wavelength radiation source, they observed that after carbon cleaning the mirror reflectivity increase from 2.5% to 30% at 92 eV energy. We also used both *in-situ* and *ex-situ* UV cleaning techniques for cleaning different optical components, this chapter covers results of UV cleaning on different optical component of SR beamlines.

5.2 Mechanism of UV Radiation Cleaning

Carbon cleaning by UV radiation exposure is the result of photo-activated oxidation process. The adsorbed molecules (contamination) on surface of optics are excited or dissociated by absorption of UV light photons (most organic molecules have a strong absorption of radiations of wavelength between 200 nm and 300 nm). Oxygen molecule have high absorption coefficient for 245.4 nm wavelength radiation.

Radiations of 253.7 nm wavelength emitted by low pressure mercury lamps are useful for dissociating contaminant hydrocarbon molecules but ozone molecule also have high absorption cross-section for this wavelength. The 184.9 nm wavelength radiations emitted by low pressure mercury lamp dissociates the oxygen molecule into oxygen radicals. The oxygen radicals combines with molecular oxygen O_2 and produce ozone (O_3) gas [39]. The dissociation cross section of O_3 is high near 253.7 nm wavelength. The 253.7 nm wavelength radiations not only responsible to excite/dissociate the adsorbed organic molecules but it also responsible for dissociating O_3 into singlet atomic oxygen $O(^1D)$ which has strong oxidation power. Absorption of 253.7 nm wavelength radiations by O_3 reduces its intensity, resultant dissociation of contaminant molecule decrease and cleaning efficiency decrease [39]. The excited contaminant molecules and/or free radicals of oxygen produced by the dissociation of oxygen and ozone molecules react at the contaminated surface form volatile gaseous species such as CO, CO_2 , CH_4 , H_2O etc. Vig et al. [51],[121] observed that the cleaning rate increases by order of magnitude when short wavelength UV radiations ($\lambda=185$ nm) and O_3 gas are used in combination instead of UV light alone or O_3 alone. Low wavelength UV radiations ($\lambda =172$ nm) emitted by excimer lamp are also found powerful tool for removing the carbon contamination from metallic surfaces because for 172 nm wavelength O_3 gas have low absorption cross section [52] as well as excitation of absorbed contamination molecules and generation of oxygen radicals (singlet or triplet atomic oxygen) simultaneously occurs by 172 nm wavelength. Figure 5.1 shows the mechanism of carbon removal and the reactions in vicinity of carbon contaminated surface in presence of oxygen molecules and UV radiations

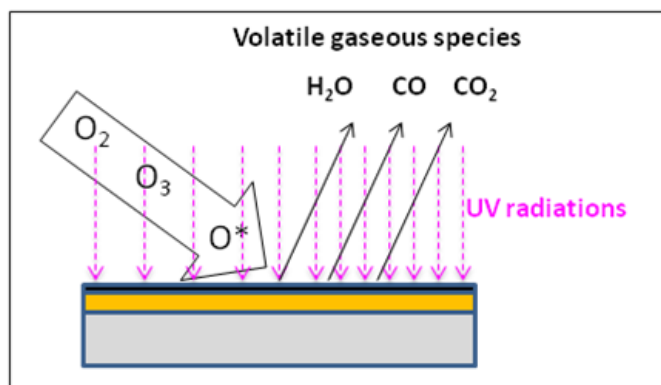
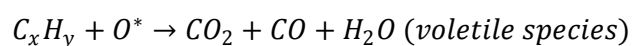
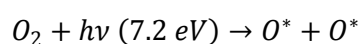
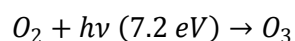


Figure 5.1: Mechanism of carbon removal by UV radiation in presence of oxygen environment.

Reaction of hydrocarbons and oxygen in presence of UV radiation of $\lambda = 172$ nm can be understood with following reaction formulas [53]



5.3 Cleaning Characteristics of Au Thin Film Surface using 172 nm UV Radiations

Xenon excimer lamp (Ex-mini L1253001, Hamamatsu) of 172 nm wavelength was used as UV source for removing carbon layer from gold thin film surfaces. The nature of synchrotron radiation induced carbon closely matches with the graphitic carbon, therefore sputtered graphitic carbon deposited on Au thin film surface are used for present study. For improving the adhesion between the silicon substrate and the gold layer a seeding layer of chromium (Cr) was deposited. The carbon coated gold surface (Si-substrate/Cr-75Å/Au-730Å/C-180Å) of 20 mm × 40 mm area was kept at

minimum accessible distance (4-5 mm) just below the lamp and continuously irradiated by UV radiations for 7 hrs in ambient environment. The lamp irradiation intensity at lamp surface is 50 mW/cm^2 in $75 \text{ mm} \times 30 \text{ mm}$ area. At 4-5 mm the carbon removing rate is $\sim 24 \text{ \AA}$ (discussed in chapter-2). After UV exposure the sample surface was characterized using different surface analysis techniques and results are compared with pristine Au sample ((Si-substrate/Cr-75Å/Au-730Å) of identical layers thicknesses.

5.3.1 Structural and Optical Parameters and Soft X-ray Reflectivity of UV

Cleaned Surface

The structural and optical characterizations of UV radiation treated and untreated surfaces were carried out by soft x-ray reflectivity measurement. Figure 5.2a. shows experimentally measured and fitted angle dependent soft x-ray reflectivity curves of pristine Au thin film surface, carbon coated (Au/C) thin film surface and after carbon cleaning using UV radiations. The reflectivity of carbon coated (Au/C) sample show interference fringes due to carbon layer and the reflectivity dip at carbon critical momentum, whereas in carbon cleaned sample absence of interference fringes and reflectivity dip at carbon critical momentum (vertical dashed line indicates carbon critical momentum in Figure 5.2a) gives a clear signature of carbon absence. The structural parameters of sample are determined by fitting of experimental data using SRxrr tool based on Parratt formalism [84]. First, the structural and optical parameters of pristine Au sample were determined. For best fitting a thin layer of $\sim 18 \text{ \AA}$ thickness with low absorption coefficient on Au surface was consider (shown in table-5.1). The obtained structural and optical parameters values of Si, SiO₂, Cr and Au were used for

carbon coated and UV treated samples. For carbon coated (Au/C) sample optical constants (δ and β), thickness (t), roughness (σ) of Au, Cr, SiO₂ and Si were kept constant (obtained from fitting of Au pristine sample) and carbon layer parameters were kept free for best fitting. Best fitting needed slight increase in Au layer thickness. For UV exposed sample, during data fitting both structural and optical parameters of Au, Cr, Si, SiO₂ and C layers were kept as free parameters because after UV exposure slight variation in structural and optical parameters may occurs. The best fitted values of optical constants and structural parameters for all three samples are shown in table-5.1. The tabulated values clearly reveal that the structural (thickness and roughness) and optical parameters of Au layer not alter after carbon layer removal by UV light exposure. After carbon removal it is also observed that a ~ 27 Å layer formed on the Au top surface, which was also present on pristine Au sample surface and the optical constants values of this layer are different from the carbon layer. The β/δ ratio of this additional layer at 90 Å wavelength is $\sim 6.5 \times 10^{-1}$, which is higher compared to graphitic carbon (β/δ ratio of graphitic carbon is $\sim 1.2 \times 10^{-1}$). After carbon removing soft x-ray reflectivity in 100 eV to 300 eV (which covers carbon absorption edge at 284 eV) was measured and compared to reflectivity of pristine Au and carbon coated (Au/C) samples (shown in Figure 5.2b). The energy dependent reflectivity clearly reveals that after carbon removing the reflectivity well matches with pristine Au sample surface reflectivity.

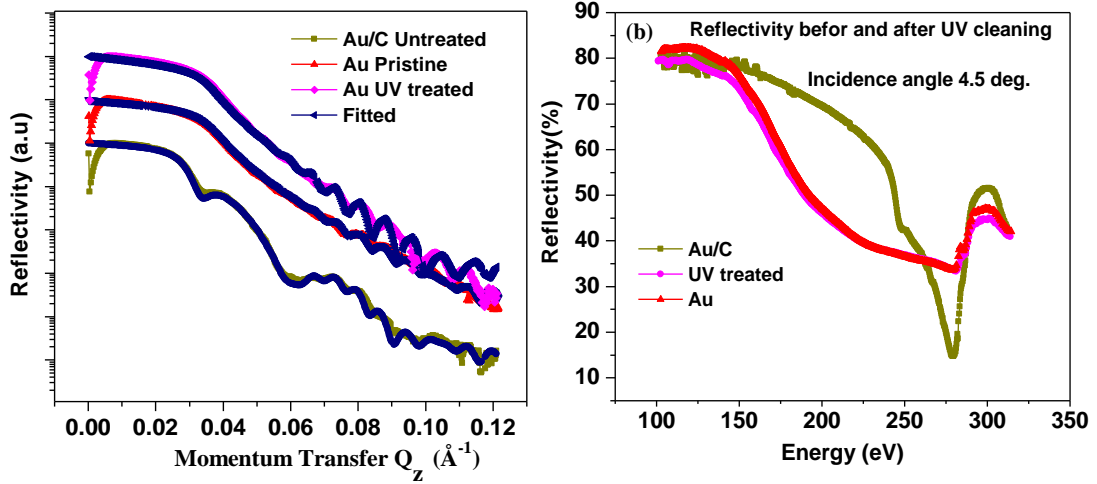


Figure 5.2: (a) Measured and fitted soft x-ray reflectivity spectra of carbon coated Au film, before and after carbon layer removal and pristine Au sample (b) Energy dependent soft x-ray reflectivity spectra of pristine Au, carbon coated (Au/C), and after carbon cleaning by UV exposure.

Table- 5.1: Optical and structural parameters obtained by curve fittings of soft x-ray reflectivity curves (measured at $\lambda = 90 \text{ \AA}$) of pristine Au, carbon coated Au sample before and after carbon layer removal. Bulk optical constants values are indicated in bracket.

Layer →		C	Au	Cr	SiO ₂	Si-Substrate
Samples ↓						
Untreated Au	δ	0.00933 (0.0166)	0.0335 (0.038)	0.03 (0.034)	0.017 (0.012)	0.0052 (0.0052)
	β	0.00102 (0.0019)	0.00928 (0.0097)	0.015 (0.017)	0.0169 (0.010)	0.016 (0.016)
	$t \text{ (\AA)}$	18.12	724	74.45	32.07	Bulk
	$\sigma \text{ (\AA)}$	7	18	12.51	12.41	5
Untreated Au/C	δ	0.0147 (0.0166)	0.0335 (0.038)	0.030 (0.034)	0.017 (0.012)	0.0052 (0.0052)
	β	0.00202 (0.0019)	0.00928 (0.0097)	0.015 (0.017)	0.017 (0.010)	0.016 (0.016)
	$t \text{ (\AA)}$	178	734	74.4	32.07	Bulk
	$\sigma \text{ (\AA)}$	23.3	18	12.5	12.41	5
UV exposed Au/C	δ	0.00747 (0.0166)	0.0335 (0.038)	0.022 (0.034)	0.013 (0.012)	0.0052 (0.0052)
	β	0.00496 (0.0019)	0.00928 (0.0097)	0.015 (0.017)	0.1698 (0.010)	0.016 (0.016)
	$t \text{ (\AA)}$	26.8	726	80.49	29	Bulk
	$\sigma \text{ (\AA)}$	8.95	15.15	8.31	6.21	5

5.3.2 Surface Analysis by XPS in Carbon K-edge Region

To see the chemical changes or composition on Au surface after UV light exposure on carbon coated Au surface, XPS experiments were carried out at BL-14 of Indus-2 synchrotron radiation source with photon beam of 4.3 keV energy [122]. This energy was chosen because below 4 keV, beryllium window have high absorption and in high energy side, cross section of generation of photoelectrons is poor.

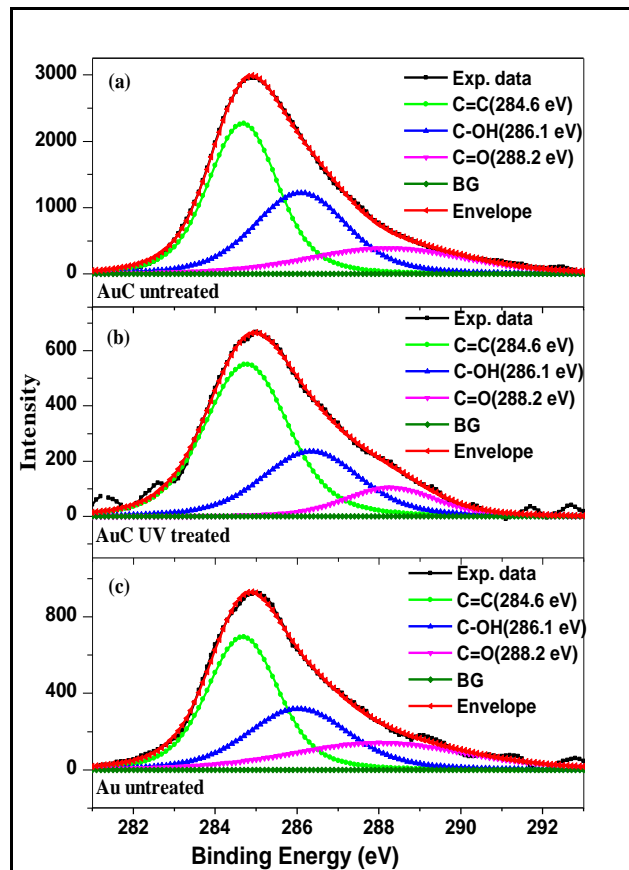


Figure 5.3: Deconvoluted XPS spectra in carbon K-edge region (a) Au/C untreated (b) Au/C UV treated (c) Au untreated samples.

Figure 5.3 shows XPS spectra of carbon cleaned sample and carbon coated and pristine Au sample in C (1s) energy region. The C (1s) peak is fitted by XPS peak fit program [88] and C (1s) peak deconvoluted into C=O (288.2eV), C-OH (286.1 eV)

and C-C (284.6 eV) peaks. In order to compare the intensity of carbon peaks, measured spectra are normalized with synchrotron ring current. The XPS spectra clearly reveal that after UV treatment the intensity of C (1s) peak decrease nearly five time and it is below the intensity of pristine Au sample intensity in C (1s) region. It indicates that carbon completely removed from Au surface after 7 hrs of UV exposure. The shift in energy of C (1s) peak after surface treatments also not observed, this indicates that carbon phase does not change after surface treatment and presence of carbon on Au surface is due to ambient adsorbed hydrocarbons.

5.3.3 Analysis of Bulk Structural Properties by GIXRD

In order to see bulk structural changes in Au layer after UV exposure, grazing incidence X-ray diffraction measurement were carried out using Bruker AXSD-8 Advance X-ray diffractometer. The diffractometer consist of monochromatic CuK_α ($\lambda = 1.54 \text{ \AA}$) radiation source. The incidence angle (θ) was kept fixed at 0.7° and diffracted angle (2θ) scan from 30° to 85° range with a step size of 0.01° . Figure 5.4 shows GIXRD spectra of carbon coated Au sample before and after UV exposure. The spectra show four diffraction peaks at 39.5° , 45.7° , 66.4° and 79.4° corresponds to Au (111), (200), (220) and (222) planes respectively. The observed diffraction peaks are fitted by considering Gaussian function. In pristine as well as UV radiation exposed samples, intensity of (111) planes is found highest in comparison to other planes intensity; it indicates that number of grains oriented in (111) direction are higher compare to other direction.

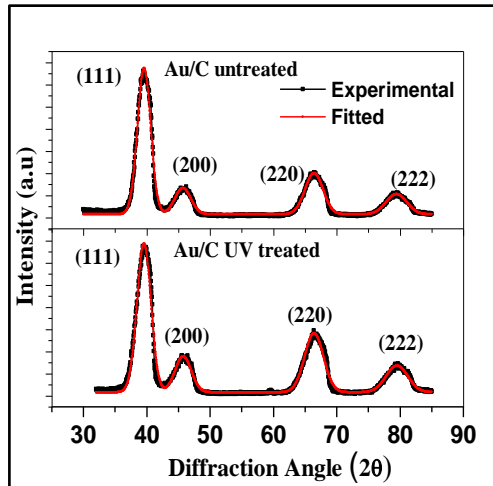


Figure 5.4: Grazing incidence angle X-ray diffraction spectra before and after carbon cleaning from Au thin film surfaces.

The peak positions and the width of the peaks are not changed after UV exposure, it indicates that after surface treatment inter plane spacing (d -spacing) of any planes are not change or any kind of stress (compressive/tensile) is not generated inside the Au layer. The area intensity ratios of (200), (220) and (222) peaks with respect to (111) peak is calculated and it is observed that ratio of (220) peak to (111) increase from 0.38 to 0.53 after UV exposure. The increase in intensity ratio of (220) peak with respect to (111) peak indicates that after surface treatment for carbon removal bulk morphology of Au layer changes by reorientations of crystallites. The reorientations of crystallites in bulk not affect the X-ray reflectivity of Au sample surface. The structural changes after surface treatment in metallic thin films are observed by many groups [123]–[125].

5.3.4 Analysis of Surface by Raman Spectroscopy

Raman spectroscopy is a sensitive tool for characterizing carbon based materials. In order to see the presence/absence of carbon after surface treatments, Raman spectra

from pristine Au sample, carbon coated (Au/C) sample and after carbon removals were recorded (shown in Figure 5.5). The Raman spectra were recorded by JobinYvon Horiba LABRAM-HR having $\lambda = 473$ nm excitation source. Single mode optical fiber was used for delivering laser light to the microscope. The Raman signal was collected using a 50X microscope objective and coupled to one end of multimode optical fiber (100 μm diameter) and second end of optical fiber is coupled to spectrometer. The Raman spectra were acquired using TE cooled (-72°C) CCD in the spectral region of 800 cm^{-1} to 1800 cm^{-1} at 1 cm^{-1} resolution. In order to avoid any heating damage on the sample surface a low power beam (25 mW) of $\sim 2\ \mu\text{m}$ spot size on sample surface was used.

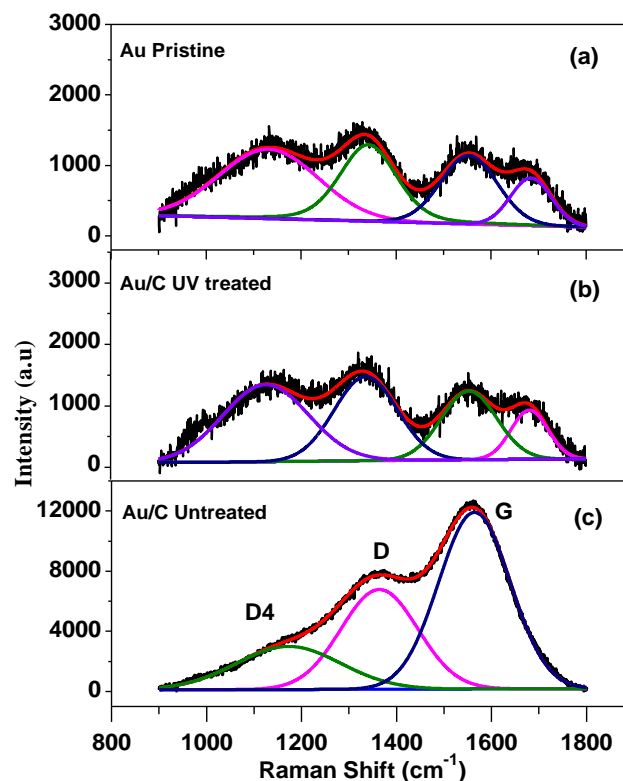


Figure 5.5: Raman spectra of (a) Pristine Au surface (b) Carbon cleaned Au surface by UV radiation exposure (c) Untreated carbon coated (Au/C) thin film surface.

The Raman spectrum of Au/C sample clearly shows G and D peaks of graphitic carbon. The G-band center around 1560 cm^{-1} and is due to an ideal lattice vibration mode with E_{2g} symmetry and show the presence of sp^2 hybridized carbon whether it is present in linear chains or rings. The D band indicates presence of disorder in carbon ring and is related to the breathing mode of the carbon hexagons [102]. The D4 peak center around 1180 cm^{-1} is attributed to presence of sp^2 - sp^3 mixed phase of carbon [126]. The Raman spectrum of carbon cleaned sample is well coincide with pristine Au sample spectrum. It indicates that carbon from Au surface completely removed. Presences of various low intensity peaks in pristine as well as in carbon cleaned surface after UV exposure are due to ambient adsorbed hydrocarbons on the Au surface.

5.4 *Ex-situ* Cleaning of Synchrotron Optics by UV Radiation

Exposure

In previous section we have described the surface characterization results of carbon cleaning from mirror like Au thin film surface using $\lambda = 172\text{ nm}$ UV source (Excimer lamp). On basis of previous experience actual synchrotron optic such as Pt coated totoidal shape post mirror (TM2) (30 mm×150 mm) of PES beamline (BL-02), Au coated pre mirror (TM1) (130 mm×110 mm) and Au coated grating (70 mm diameter) of photo-physics beamline (BL-05) of Indus-1 SR source were refurbished using *ex-situ* UV radiation ($\lambda = 172\text{ nm}$) exposure. These optics were in use in beamlines for more than a decade. The optic to be clean were put in center of uniform emission area at 4-5 mm distance just below the lamp using height adjustable stand. The distance between source and the mirror was pre optimized using carbon coated Pt samples.

Falkenstein [52] studied the surface cleaning phenomena at different pressures and distances from UV lamp. He observed that 5 mm distance from the source at low pressure (0.01 to 0.001 atm) is more effective compare to 1 mm. He concluded that at 5 mm distance from source the atomic oxygen concentration and its mean free path is sufficient at atmospheric pressure for efficient carbon cleaning from optics surfaces. For complete removal of carbon contaminations layer from TM2, the mirror was exposed to UV radiation for 7 hours continuously in atmospheric environment, whereas gold coated TM1 and grating of photo-physics beam line were exposed for 18 hours in same experimental conditions. The exposure time depends on carbon contamination layer thickness. The photograph of different optics before and after cleaning is shown in Figure 5.6 (Pt coated TM2), Figure 5.7 (Au coated TM1) and Figure 5.8 (Au coated grating).

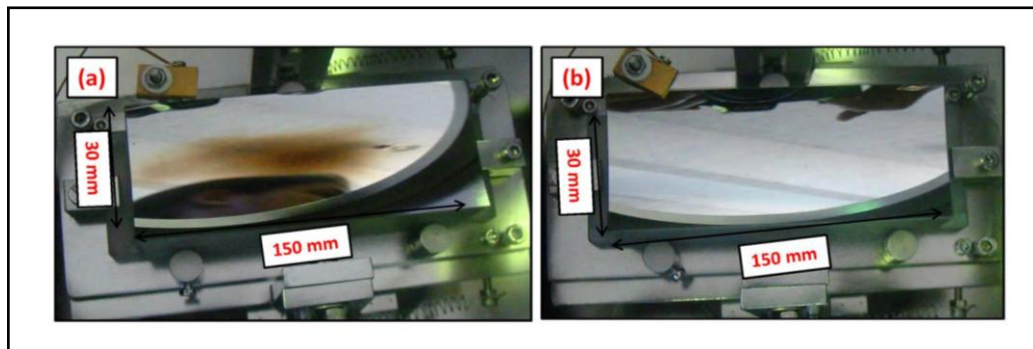


Figure 5.6: Pt coated post mirror (TM2) (a) before (b) after UV radiation exposure of 7 hrs.

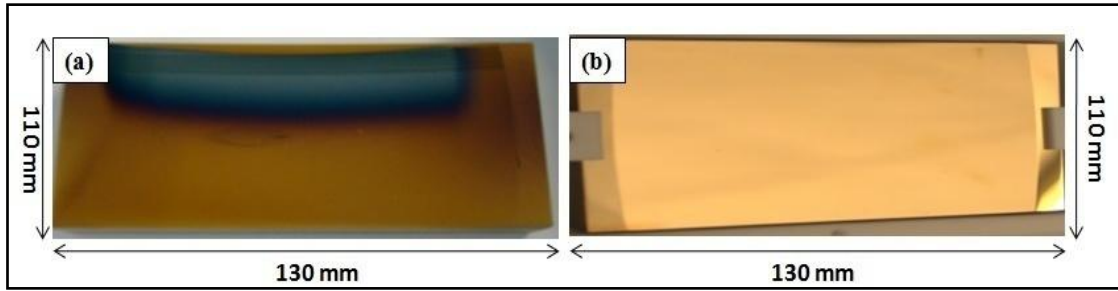


Figure 5.7: Au coated pre mirror (TM1) (a) before (b) after UV radiation exposure of 18 hrs.

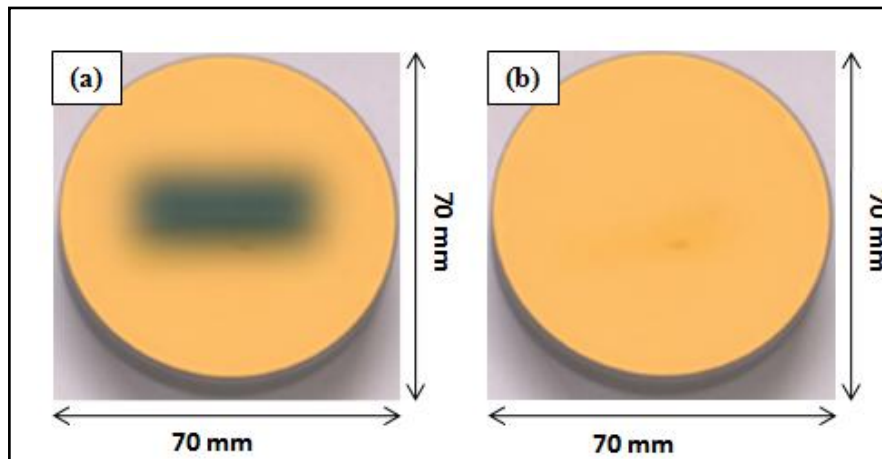


Figure 5.8: Au coated grating (a) before (b) after UV radiation exposure of 18 hrs.

5.5 *In-situ* Mirror Cleaning by Zero Order Synchrotron Radiations

In-situ optics refurbishing technique is used to refurbish post mirror (TM2) of reflectivity beamline at Indus-1. *In situ* cleaning technique is very useful where optics are mounted in complex geometry and their alignment is crucial. This technique also reduces down time of beamline. The technique involves the use of photo-generated reactants (oxygen radicals and excited hydrocarbons) produced by photo-ionization reactions in presence of oxygen gas and zero order synchrotron radiation. The production of photo-generated reactants and excitation of adsorbed hydrocarbon on optics surface both reactions are performed by zero order synchrotron radiation. After

raising oxygen pressure in $2-8 \times 10^{-6}$ mbar range the TM2 was exposed by zero order synchrotron radiations in four steps at different ring current values for ~ 40 hours. Detailed description about experimental setup used for *in-situ* cleaning in reflectivity beamline is given in Chapter-2. Details of cleaning procedure and the results are discussed in next section.

5.5.1 *In-situ* Cleaning Procedure for Post Mirror Cleaning at Reflectivity

Beamline of Indus-1

There are some essential requirements for *in-situ* cleaning of optics in beamlines such as the pressure in the vicinity of optics must be in the range of 10^{-8} - 10^{-10} mbar otherwise a reverse effect on optics surface may induce. There should be a proper vacuum safety interlocking between beamline and the storage ring.

The reflectivity beamline (BL-04) at Indus-1 is operational since 2001. The beamline operates in 10^{-9} - 10^{-10} mbar pressure. For *in-situ* cleaning of TM2 following procedure was followed. (i) To protect the vacuum of rest of the beamline as well as storage ring a suitable vacuum safety interlocks scheme was implemented (ii) before increasing oxygen gas pressure in post mirror section partial pressure of gases in absence of synchrotron beam was recorded by residual gas analyzer (iii) before cleaning the mirror two separate measurements of SR beam intensity in 100 eV to 300 eV energy region were carried out using a silicon photo diode detector (AXUV100G: IRD) (iv) Dry oxygen gas of 99.99% purity was injected in the post mirror chamber with the help of mass flow controller and a fine leak valve. In the post mirror chamber oxygen gas pressure was maintained in $2-8 \times 10^{-6}$ mbar by regulating gas flow through MFC and right angle valve mounted on turbomolecular pump (turbo-molecular pump is

mounted between post mirror section and monochromator section) (v) after pressure stabilization, zero order SR beam was allowed from monochromator for TM2 exposure in presence of oxygen gas pressure. The exposure was done in four stages when ring current in the storage ring decreased from (a) 40 mA to 16 mA (7 hrs duration) (b) 62 mA to 37 mA (5 hrs duration) (c) 82 mA to 11 mA (19 hrs duration) (d) 120 mA to 20 mA (10 hrs duration) (vi) During exposure with zero order SR beam, partial pressure in post mirror section was again recorded. (vii) after completion of cleaning experiment, again SR beam intensity in same energy range using same detector was measured. The intensity ratio, after cleaning to before cleaning was calculated to see the difference in photon intensity near the carbon K-edge.

5.5.2 Results of *In-situ* Cleaning of Post Mirror

Partial pressure of post mirror section of reflectivity beamline measured by residual gas analyzer at different stages of cleaning process. Before allowing SR beam and oxygen gas into post mirror section partial pressure of carbon and carbeneous gases such as C, CH₄, CO and CO₂ are 7.9×10^{-12} , 6.3×10^{-12} , 1.9×10^{-10} and 3.5×10^{-11} mbar respectively. During exposing the mirror by zero order SR beam in presence of oxygen gas environment, the partial pressure of C, CH₄, CO and CO₂ gases increases to 3.9×10^{-10} , 5×10^{-9} , 1.9×10^{-10} and 3×10^{-9} mbar respectively. The increase in carbeneous gases pressure is the result of formation of volatile gases species by the reaction of excited hydrocarbons adsorbed on mirror surface with photo-dissociated oxygen atoms/radical. After exposing the mirror for 40 hrs by zero order synchrotron the partial pressure of C, CH₄, CO and CO₂ gases decrease again to 9.1×10^{-12} , 8.3×10^{-12} , 4.2×10^{-10} and 4.8×10^{-11} mbar respectively. These observations reveal that in

presence of zero order synchrotron radiation and oxygen gas pressure carbonaceous gases are evolved and they are pumped out by dynamic pumping system resultantly partial pressure of carbonaceous gases decreases.

Figure 5.9 shows the photon intensity ratio in 100 eV to 300 eV energy range of two separate measurements of photon intensity before cleaning the post mirror. The graph indicates that photon intensity in two separate measurements remain nearly same.

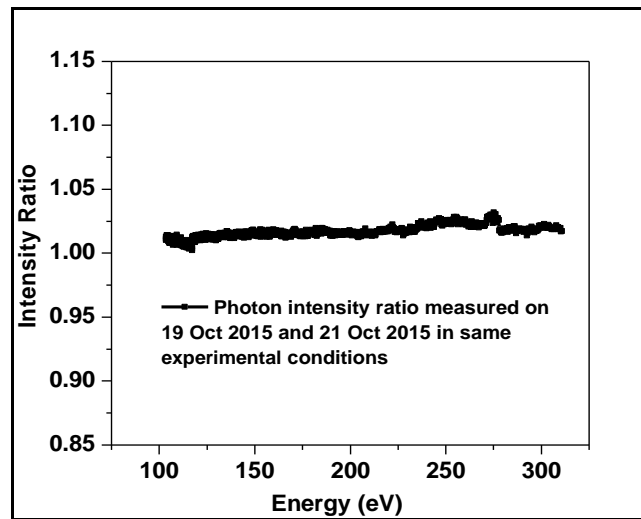


Figure 5.9: Reflectivity ratios of two independent measurements before cleaning the mirror in 100 eV - 300 eV energy range.

Figure 5.10a shows the photon intensity measurements before (black) and after (red) cleaning the post mirror. The ratio of photon intensity after cleaning to before cleaning is plotted in Figure 5.10b. The increase in photon intensity near carbon absorption edge (284 eV) indicates that carbon from mirror surface decreased. The decrease in photon flux in 100 eV to 275 eV is expected because in this energy region the reflection from carbon layer is higher in comparison to gold layer. The increase in photon intensity up to 35% near carbon absorption region and decrease in photon

intensity in 100 eV to 275 eV energy range clearly reveals the carbon cleaning effect of mirror surface.

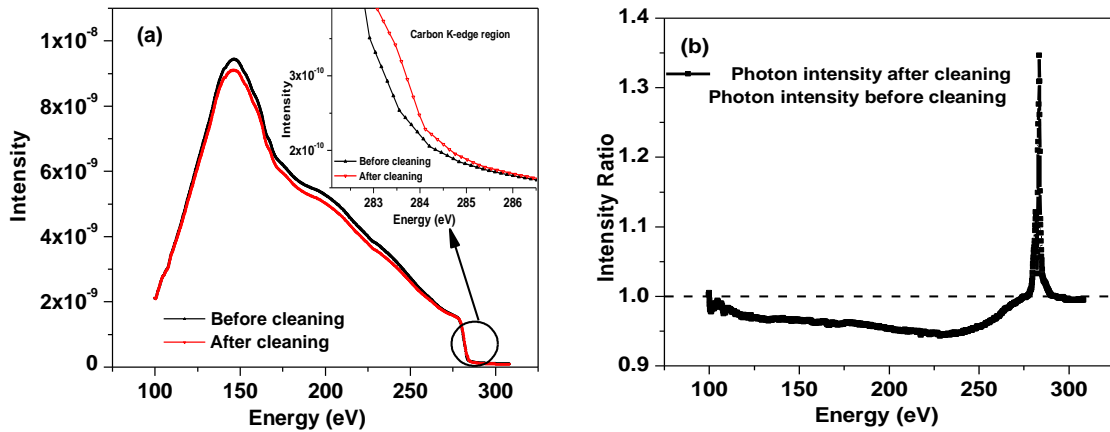


Figure 5.10: (a) Measured photon intensity in reflectivity beamline before (black curve) and after (red curve) in-situ cleaning the post mirror (inset image show change in reflectivity near K-edge region) (b) Photon intensity ratio after cleaning to before cleaning.

5.6 Summary

Use of ultraviolet (UV) radiation is an effective method for removing variety of contaminants from surfaces. We have successfully removed carbon contamination layer from Au thin film surface by UV radiation exposure. After carbon removal the surface of Au was analyzed by different surface analysis techniques and it is observed that Au surface not damage after carbon removal and soft x-ray (100 eV-300 eV) reflectivity of Au surface is regained up to pristine Au sample reflectivity. With the use of 172 nm UV radiation source different synchrotron optics used in different beamlines at Indus-1 SR source are refurbished using this technique. *In-situ* cleaning technique is successfully implemented in reflectivity beamline at Indus-1 for post

mirror (TM2) cleaning. *In-situ* cleaning result reveals that after TM2 cleaning, photon intensity in the beamline increased by 35% near carbon K-edge.

6 Refurbishment of X-ray Optics by IR Laser Scanning

6.1 Overview

Applications of laser for welding, drilling and cutting of metals by laser are well known for the years but surface cleaning by lasers without surface damage is still going through different phases of technology development. Laser cleaning can be defined as removal of unwanted contamination/coating layers from a solid surface. Requirement of non abrasive and non hazardous surface cleaning process has motivated the researchers to develop laser cleaning technology. The use of laser technology to remove contamination has been studied [44]. In recent days laser surface cleaning seems to be one of the best possible solution for selective material removal. In literature recent experimental results showed that laser cleaning technique may be real substitute to chemical and mechanical techniques to remove several types of contaminants from a large set of materials. Laser cleaning for removal of contaminations has high potential in replacing wet chemical method. In laser cleaning the material is removed by combination of thermal and mechanical effects [45]. The cleaning mechanism by laser strongly depends on laser beam properties, its delivery method (pulsed or CW laser beam) and physical and chemical properties of material to be removed. Different organic and inorganic materials can be removed selectively using optimized laser parameters (wavelength, intensity, pulse width, pulse repetition rate and beam size) [127]–[129]. In selective material removal, laser wavelength is an important parameter. The wavelength (1064 nm) emitted by Nd:YAG laser is strongly absorbed by most of the organic materials and the substrate materials (Au, Ag, etc.)

have low absorption coefficient for this wavelength in comparison to organic materials [130]-[131]. Due to large difference in energy absorption between two materials, selective contamination removal can be easily carried out using Nd:YAG laser at relatively low fluence ($F < 1 \text{ J/cm}^2$), which minimize the risk of damage to base material. At higher fluence ($F > 1.5 \text{ J/cm}^2$) the contamination removal mechanism becomes more complex due to formation of plasma and shock wave just above the surface, result in damage of the surface. Thus, in order to avoid the surface damage cleaning should be carried out at the optimum value of fluence. This chapter describes the mechanism of carbon removal using infrared (IR) laser and surface analysis results after carbon removal using IR laser at optimized laser parameters. The results of laser cleaning also compared with the results of other techniques (plasma and UV cleaning) used in this thesis.

6.2 Absorption of Laser Energy and Temperature Rise of Material

When a laser beam incident on a material surface, it can absorb, transmit and reflect from the material surface. Whether, incident photon will absorb or not absorb into electronic/vibration states, it depends on incident photon wavelength as well as on material properties. The phenomenon of absorption of light in metals, semiconductors and insulators are not same. Absorption of laser light (optical absorption) in metals is dominated by the free electrons through inverse bremsstrahlung [128]. After absorption of photons by free electrons, energy is subsequently transferred to lattice phonons by lattice collisions. In semiconductors and insulators, the absorption of laser light occur through and resonant excitations in inter-band and intra-band [54]. These excited electronic states can then transfer energy to lattice phonons. Photons with

energy below the band gap will not be absorbed. The time taken to transfer energy from the excited electronic states to phonons and thermalization process both are material specific. For most metals, the thermalization time ranges from pico seconds (*ps*) to nano seconds (*ns*), and in non-metals, due to variation in the absorption mechanisms, the thermalization time is of the order of microseconds (μs) [54]. The absorbed laser energy can be directly transformed into heat if thermalization rate is high in comparison to the laser-induced excitation rate. Such processes are known photo-thermal. For instance, laser processing of metals or semiconductors with laser pulse time greater than *ns* is typically characterized by photo-thermal mechanisms. When thermalization rate is low in comparison to laser induced excitation rate, large excitations can build up in the intermediary energy states. These excitation energies are sufficient for breaking the bonds. This type of non-thermal material modification process is known as photochemical process. The ultrafast femto second (*fs*) laser pulses can enable photochemical processing of metals and semiconductors. During purely photochemical processing, the temperature of the system remains relatively unchanged. Material responses exhibit both thermal and non-thermal mechanisms and are referred as photo-physical process [54]. In photo-thermal heat transfer mechanism, when fluence (energy/area) increased above a certain limit, the material will be heated to a sufficiently high temperature and vaporize it. The spatial and temporal evolution of temperature can be calculated by heat equation [132], [133].

$$\nabla^2 T(x,t) - \frac{1}{k} \frac{\partial T(x,t)}{\partial t} = - \frac{A(x,t)}{K} \quad (6.1)$$

Where $T(x,t)$ – is temperature at distance x inside the material after time t , $A(x,t)$ - heat produce per unit volume per unit time, k -thermal diffusivity and K -thermal

conductivity of material. If a constant laser flux I_a is incident at the surface ($x = 0$) and there is no phase change of the material, the solution of the above equation can be written as [132]

$$T(x,t) = \frac{2\alpha I_a}{K} (\sqrt{kt}) \operatorname{ierfc} \left(\frac{x}{2\sqrt{kt}} \right) \quad (6.2)$$

Here α is absorption coefficient, ierfc is the integral of the complimentary error function and the value of ierfc at the surface ($x = 0$) is given by

$$\operatorname{ierfc} \left(\frac{0}{2\sqrt{kt}} \right) = \operatorname{ierfc} (0) = \frac{1}{\sqrt{\pi}} \quad (6.3)$$

$$T(0,t) = \frac{2\alpha I_a}{K} \left(\sqrt{\frac{kt}{\pi}} \right) \quad (6.4)$$

Temperature as a function of laser fluence can be written as

$$T(0,t) = \frac{2\alpha F_a}{K} \left(\sqrt{\frac{k}{\pi t}} \right) \quad (6.5)$$

Where F_a is given by $I_a t$

6.3 Material Response during Laser Exposure

If laser induced excitation is photo-thermal than absorbed laser energy directly transform into heat. In such situation temperature gradient depends on rate of energy absorption or rate of temperature rise and rate of cooling for an exposure conditions. For ns pulsed laser the material heating rate can be as high as 109 K/second and this can be higher for fs pulsed laser. Depending on incident flux value variety of

temperature dependent phenomena within the solid material may occur, that are discussed below.

When fluence below the threshold of melting point of material: When fluence (energy/area) of laser on material surface is below the threshold of melting point of the material the rapid temperature gradients can reorganize the crystal structure of material; it can induce thermal stresses and thermo-elasticity. These stresses can contribute to work hardening, warping or cracking inside material. Localized laser heating can produce large temperature gradients which lead to rapid self-quenching of the material and trapping in highly non-equilibrium structures. The temperature rise can enhance diffusion rates promoting impurity doping and sintering of porous materials [134]–[136].

When Fluence above the threshold of melting point of material: Fluence higher than the threshold of melting point of material can lead to the formation of transient pools of molten material on the surface. Due to high solubilities and atomic mobilities of molten material compared to solid phase results in rapid material homogenization. High self-quenching rates with solidification front velocities up to several meter/sec can be achieved by rapid dissipation of heat into the cooler surrounding bulk material [136]. Such rapid quenching can freeze in defects [137]. Recrystallization of material with larger grains compared to original material may also occur at low resolidification rates. Im et al. [138] observed that recrystallization dynamics can be controlled by shaped beam profiles. Hydrodynamic motion can reshape the material when temperature is much higher than melting temperature. Radial temperature gradients of the order of 100 K/mm can develop in melt pools, causing convective flows to

circulate material. For most of the materials, the liquid's surface tension decreases with increasing temperature and the liquid is pulled from the hotter to the cooler regions (Marangoni effect) [139].

Ablation of material by laser exposure: In ablation process material is directly removed from substrate by direct absorption of laser energy. Ablation depends on absorption mechanism, material properties (microstructure, morphology and the presence of defects) and laser parameters (wavelength, pulse duration etc.). The ablation threshold value of fluence for organic materials lies between 0.1 and 1 J/cm², for inorganic insulators lies between 0.5 and 2 J/cm² and for metals it is between 1 and 10 J/cm² [54]. At low fluence, photo-thermal mechanism for ablation includes material evaporation and sublimation. Above the ablation threshold, the quantity of material removed per pulse typically shows a logarithmic increase with fluence. For a compound material, highly volatile species may be evaporate/sublimate more rapidly resultant a change in chemical composition of the remaining material occurs [140]. At higher fluences, heterogeneous nucleation of vapor bubbles leads to normal boiling. When material excitation rate is larger than the thermalization rate in the material, photochemical (non-thermal) ablation mechanisms can occur. For instance, with ultra fast pulses, direct ionization and the formation of dense electron-hole plasma can lead to explosive disintegration of the lattice and direct bond breaking [141].

Material responses often involve a combination of ablation (evaporation, sublimation), surface melting and thermally activated processes, which can lead to cumulative changes in the material's surface profile its chemistry. For instance, residual heat left

after ablating material from a surface can lead to further melting or other thermally activated processes in the remaining surface and surrounding volume of material.

6.4 Threshold Fluence for Laser Cleaning

Laser cleaning is a selective material removing process in which material removing process starts above a minimum fluence value known as threshold fluence (F_{th}). The threshold fluence for ablation is define as minimum fluence required for ejecting particle from the surface without damaging surface of base material. Laser cleaning initiated with thermal ablation of the material from the surface by irradiating the surface to a laser beam of short pulse duration ($\sim ns$) and high energy density [142]–[145]. The relation of threshold fluence with pulse width (t) is given by [132]

$$F_{th} = \frac{T(0,t)K}{2\alpha} \left(\sqrt{\frac{\pi t}{k}} \right) \quad (6.6)$$

Which shows that F_{th} is proportional to \sqrt{t} , and with long laser pulses the laser threshold fluence will be higher, which lead to increase in surface temperature. The carbon deposited gold thin film surfaces treated at two different fluence values (0.26 J/cm^2 and 0.5 J/cm^2) are shown in Figure 6.1. The sample exposed to high fluence (0.5 J/cm^2) value is damage due to sudden increase in temperature of gold surface. The damage regions are marked by red circles in the Figure 6.1b.

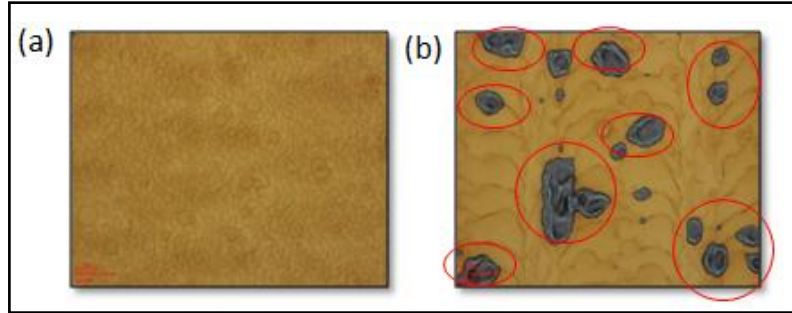


Figure 6.1: Confocal microscopic images ($473 \times 355 \mu\text{m}^2$) of carbon cleaned gold thin film surfaces (gold deposited on Si wafer) at two different fluence values (a) $F=0.26 \text{ J/cm}^2$ and (b) 0.5 J/cm^2 . The marked black spots represent damage region of gold surface at 0.5 J/cm^2 fluence value.

For carbon removal *ns* pulsed laser is generally used. Nano second pulses suddenly increase the temperature which produces thermal expansion in absorbing layer resultant thermal ablation of absorbing layer take place. Thermal ablation includes material evaporation, sublimation and physical detachment by thermal expansion. When force generated by thermal expansion is greater than the sum of all adhesive forces (Van-der Waals, electrostatic, capillary forces etc.) the contamination layer comes out or detach from substrate. The mathematical expression for thermal expansion force, vaporization temperature, ablation rate and depth are given in Appendix-IV.

6.5 Carbon Removal from X-ray Optics like Surface using IR Laser

6.5.1 Sample for Study

The nature of synchrotron radiation induced carbon contamination layer closely matches with the graphitic carbon [2],[8],[15],[20]. Due to limitation of synchrotron radiations induced carbon samples graphitic carbon deposited on Au coated mirror surface are used for the experiment of carbon removal using IR laser. The graphitic

carbon layer of $\sim 180 \text{ \AA}$ was deposited on $\sim 730 \text{ \AA}$ gold coated Si substrate using ion beam sputtering. For improving the adhesion between the silicon substrate and the gold layer a chromium (Cr) layer of $\sim 75 \text{ \AA}$ thickness was deposited. The layer structure of sample is Si-substrate/Cr-75 \AA /Au-730 \AA /C-180 \AA . Before and after carbon coating the image of the Au mirror is shown in Figure 6.2.

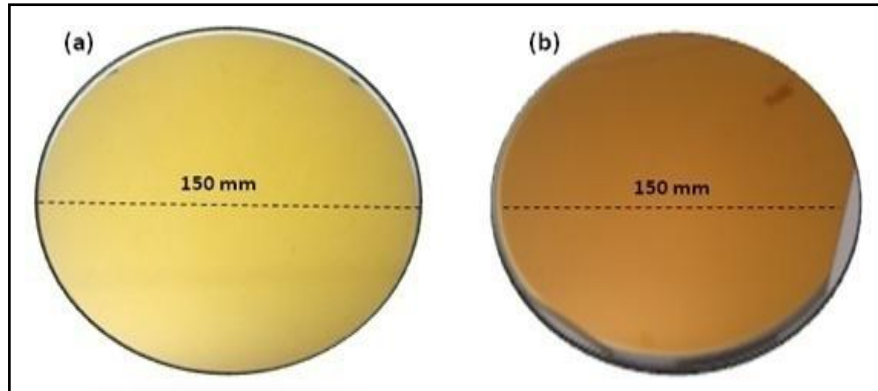


Figure 6.2: Gold coated mirror (a) Before carbon coating (b) After carbon coating

6.5.2 Carbon Removal Using IR Laser

Ytterbium (Yb) doped YAG fiber *ns* pulsed laser system was used to remove graphitic carbon layer from gold surface. The laser system description and its optimization process are given in chapter-2. To remove carbon from Au mirror surface a hatching pattern in x-y plane is chosen in such a way that maximum area can be covered by laser beam (laser beam scan sample surface at 0° , 45° and 90°). The laser scan scheme is shown in Figure 6.3. The sample of dimension $20 \text{ mm} \times 40 \text{ mm}$ was kept 5.5 mm above from the focal plane of laser beam (at 5.5 mm above the focal plane, beam diameter is $400 \pm 10 \text{ \mu m}$) and the laser was operated at 30 watts power, 90 kHz pulse frequency, 170 ns pulse width, 5000 mm/s scan speed (V_x) in x-direction and with step size of 15 \mu m in y-direction. The fluence value on these parameters is about

0.26 J/cm² and the overlapping is about 85% (see Figure 2.16). This fluence value is below the melting threshold fluence value of most of metallic surfaces. For bulk Au surface, the damage threshold fluence value (~ 2.5 J/cm²) was measured by Sergey et al.[131] using Nd:YAG ($\lambda=1064$ nm) laser, whereas Henely et al. [146] simulated melting threshold laser fluence for Au thin film, they observed that melting fluence value vary from 0.5 J/cm² to 0.3 J/cm² when film thickness vary from 50 Å to 400 Å.

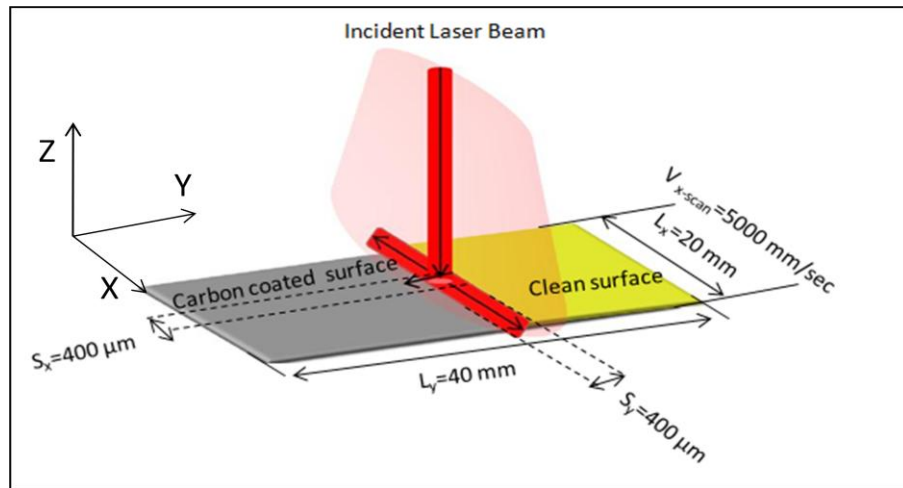


Figure 6.3: Schematic diagram of laser beam scanning on carbon coated surface. L_x and L_y represents sample length and width, S_x and S_y represents laser beam size in x and y directions, and V_{x-scan} represents laser scan speed in x direction.

In order to complete removal of carbon, the laser beam scans the carbon coated sample surface by twenty times, than for polishing purpose sample is move 3 mm above (away from focus plane, at reduced fluence) and the same scanning pattern was repeated for another ten times. The total time taken for removing the carbon from 20 mm × 40 mm sample is nearly 16 minutes. In order to avoid re-deposition of ablated carbon from gold surface during laser scanning a fan of 0.26 m³/min exhaust

capacity was used. Confocal microscopic images ($473 \mu\text{m} \times 355 \mu\text{m}$) before and after cleaning are shown in Figure 6.4.

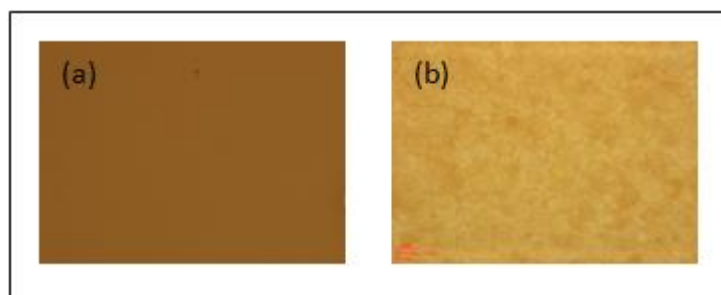


Figure 6.4: The confocal microscopic images ($473 \mu\text{m} \times 355 \mu\text{m}$) of carbon coated Au thin film surface (a) before and (b) after laser cleaning at 0.26 J/cm^2 fluence and at 85% overlapping of laser pulses.

6.6 Characterization of Carbon Coated Au Surface after Laser

Treatment

The exposure of laser beam to sample surface can induce several structural changes in the gold layer of mirror (discussed in section-6.3). In order to see the cleaning efficiency and surface morphology of carbon cleaned surface is characterized by Soft x-ray reflectivity, Raman spectroscopy (RS), Photoelectron spectroscopy (PES) and Atomic force microscopy (AFM) techniques.

6.6.1 Structural and Optical Parameters before and after Carbon Cleaning

The structural and optical parameters of IR laser cleaned sample were determined by soft X-ray reflectivity measurements and compared with pristine gold and untreated carbon coated gold (Au/C) surface of same structural parameters. The angle dependent soft x-ray reflectivity measurements were carried out using at reflectivity beamline (BL-04) of Indus-1. The incident X-ray wavelength 90 \AA is kept constant and incident

angle vary from 0 to 50 degree with step size of 0.08 degree. The reflected intensity from sample surface is detected by Si photodiode detector. Momentum transfer (Q_z) versus measured reflected intensity and fitted reflectivity spectra before and after carbon cleaning and pristine gold mirror surfaces are shown in Figure 6.5.

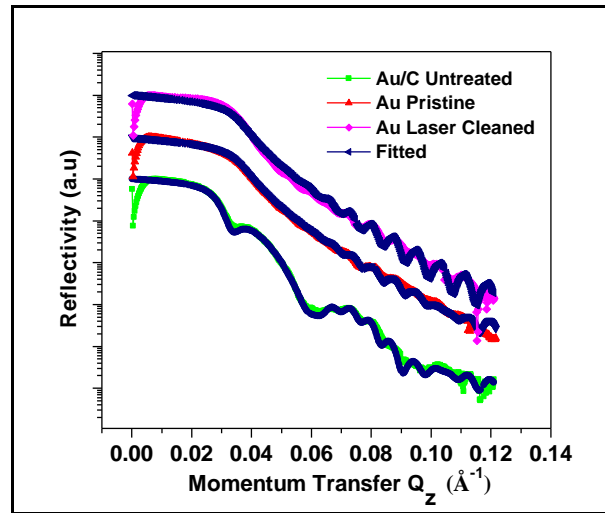


Figure 6.5: Measured and fitted soft x-ray reflectivity spectra before and after carbon cleaning from Au surface by IR laser and pristine Au surfaces.

The structural parameters are determined by fitting the experimental data using SRxrr tool [84]. For data fittings a similar procedure was adapted that was employed in case of UV cleaning. First the structural and optical parameters of pristine Au sample were determined. For best fitting a thin layer of ~ 18 Å thickness of $\delta = 9.3 \times 10^{-3}$ and $\beta = 1 \times 10^{-3}$ on Au surface was consider. The obtained structural and optical parameters values of Si, SiO₂, Cr and Au were used for Au/C untreated and Au/C IR laser treated samples. For Au/C untreated sample optical constants (δ and β), thickness (t), roughness (σ) of Au, Cr, SiO₂ and Si were kept constant and carbon layer parameters were kept free for best fitting. For IR laser treated samples, during data fitting both structural and optical parameters of Au, Cr, Si, SiO₂ and C layers were kept as free

parameters because after laser exposure slight variation in structural and optical parameters may occurs. The best fitted values of optical constants and structural parameters are shown in table-6.1. The tabulated values clearly reveal that the surface roughness of Au surface decrease from 18 Å to 15.15 Å and optical parameters of Au layer not change after carbon layer removal with IR laser exposure. After removal of carbon layer a 19.7 Å thin layer with $\delta= 1.82 \times 10^{-2}$ and $\beta= 4.8 \times 10^{-3}$ is observed on the Au top surface, which was also present on pristine Au sample surface with thickness of ~18 Å and the optical constants values of this thin layer is different from the carbon layer. The β/δ ratio of this additional layer at 90 Å wavelength is $\sim 2.5 \times 10^{-1}$, and it is different from graphitic carbon $\sim 1.3 \times 10^{-1}$).

Table- 6.1: Optical and structural parameters obtained by soft x-ray ($\lambda= 90\text{Å}$) reflectivity curve fittings using SRxrr tool [84]. Bulk optical constant values are mentioned in bracket.

Layers →		C	Au	Cr	SiO ₂	Si- substrate
Treatments ↓						
Untreated Au	δ	0.00933 (0.0166)	0.0335 (0.038)	0.03 (0.034)	0.017 (0.012)	0.0052 (0.0052)
	β	0.00102 (0.0019)	0.00928 (0.0097)	0.015 (0.017)	0.0169 (0.010)	0.016 (0.016)
	t (Å)	18.12	724	74.45	32.07	Bulk
	σ (Å)	7	18	12.51	12.41	5
Untreated Au/C	δ	0.0147 (0.0166)	0.0335 (0.038)	0.030 (0.034)	0.017 (0.012)	0.0052 (0.0052)
	β	0.00202 (0.0019)	0.00928 (0.0097)	0.015 (0.017)	0.017 (0.010)	0.016 (0.016)
	t (Å)	178	734	74.4	32.07	Bulk
	σ (Å)	23.3	18	12.5	12.41	5
IR laser treated	δ	0.0182 (0.0166)	0.0335 (0.38)	0.0022 (0.034)	0.013 (0.012)	0.0052 (0.0052)
	β	0.0048 (0.0019)	0.0093 (0.0097)	0.015 (0.0171)	0.169 (0.010)	0.016 (0.016)
	t (Å)	19.7	726	74.45	32	Bulk
	σ (Å)	13.9	15.15	8.31	6.21	5

6.6.2 XPS Analysis of Au Surface before and after Carbon Cleaning

To see the chemical composition on Au surface after laser exposure on carbon coated Au surface, XPS experiments were carried out at XPES beamline (BL-14) of Indus-2 SR source using 4.3 keV photon energy [122].

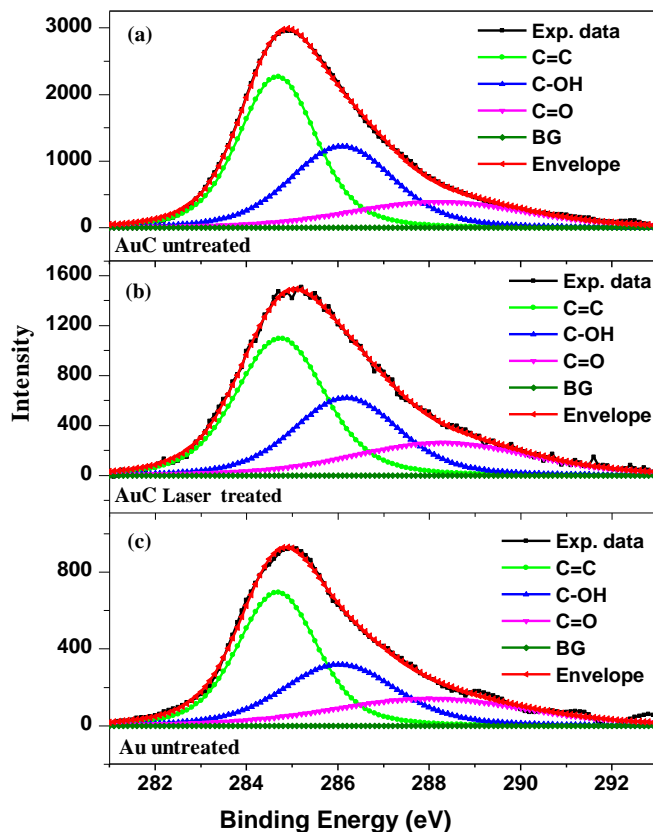


Figure 6.6: XPS spectra in C (1s) region (a) Au/C untreated, (b) Au/C laser treated and (c) pristine Au samples.

The XPS spectrum is compared with untreated carbon coated Au and pristine Au sample. For electron energy analysis and data acquisition, high resolution hemispherical analyzer (Phoibos 225Specs, Germany) with a micro-channel plate and CCD detector system with SpecsLab Prodigy and Casa XPS software was used. In order to compare the intensity of carbon peaks, measured spectra are normalized with

synchrotron ring current. The measured spectra are deconvoluted into three peaks (C-C, C-OH and C=O). The normalized spectra in 280 eV to 293 eV binding energy ranges are shown in Figure 6.6. The spectra clearly indicate that after laser treatment the carbon intensity in C (1s) region decreases in comparison to untreated Au/C sample but it still higher than pristine Au sample. This result reveals that carbon not removed completely from Au surface after laser treatment even though the laser fluence value was near to the gold threshold fluence value. Further increase in fluence may lead to surface damage.

6.6.3 Analysis of Au Surface before and after Carbon Cleaning by Raman Spectroscopy

The Raman spectra before cleaning and after cleaning with laser exposure are shown in Figure 6.7. The spectra for both samples are acquired in identical conditions at room temperature by JobinYvon Horibra LABRAM-HR spectrometer using $\lambda = 473$ nm excitation source. Raman spectra clearly show G and D peaks of graphitic carbon in both laser treated and untreated samples. The G peak is related to presence of sp^2 hybridized carbon and presence of D peak show disorder in graphitic carbon rings (details of G and D peaks of graphitic carbon are given in chapter-3). In laser treated sample intensity of G peaks decreases and its position shift from 1562 cm^{-1} to 1592 cm^{-1} . According to Ferrari and Robertson [102] G peak intensity decreases as numbers of sp^2 hybridized carbon layers decrease in the sample. Wall [147] established a relation between G peak position and the number of graphene layer in the stage ($W_G = 1581 + 11/(1+n^{1.6})$) where n represent number of graphene layers in stage. The relation clearly indicates that as number of layers decreases the G peak

position shift towards higher frequency. He also shows linear increase in G peak intensity as number of layers increases in the stage. In laser treated sample shift in G peak position toward high frequency and decrease in G peak intensity reveals that carbon layer thickness decrease but Raman spectrum not matches with spectrum of pristine Au sample spectrum (shown in section 6.7).

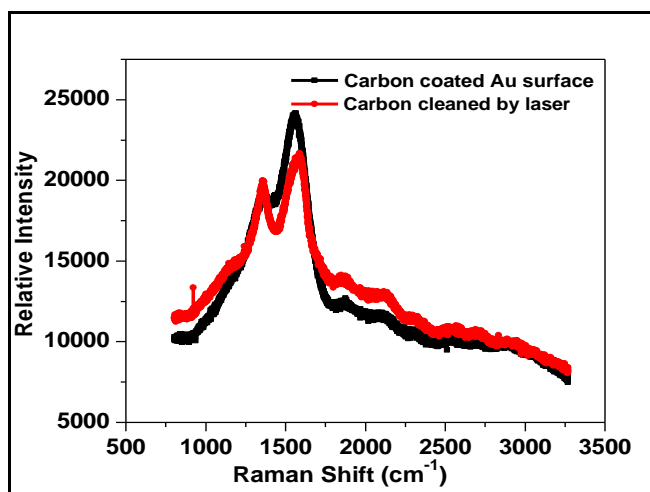


Figure 6.7: Raman spectra of carbon coated Au surface before and after carbon IR laser cleaning.

6.6.4 Analysis of Bulk Structural Properties by GIXRD

In order to see bulk structural changes in Au layer after laser treatment, grazing incidence x-ray diffraction measurement was carried out on laser treated and untreated samples using Bruker AXSD-8 Advance x-ray diffractometer with monochromatic Cu K_α radiation ($\lambda = 1.54 \text{ \AA}$). The incidence angle (θ) was kept fixed at 0.7° and diffraction angle (2θ) vary from 30° to 85° with a step of 0.01° . The diffraction patterns are shown in Figure 6.8. In both samples four diffraction peaks of Au (111), (200), (220) and (222) planes at 39.5° , 45.7° , 66.4° and 79.4° respectively are observed. The observed diffraction peaks are fitted by considering Gaussian function.

In both the cases highest intensity of (111) planes is observed highest in comparison to other planes intensity; it indicates that number of grains oriented in (111) direction are higher compare to other direction.

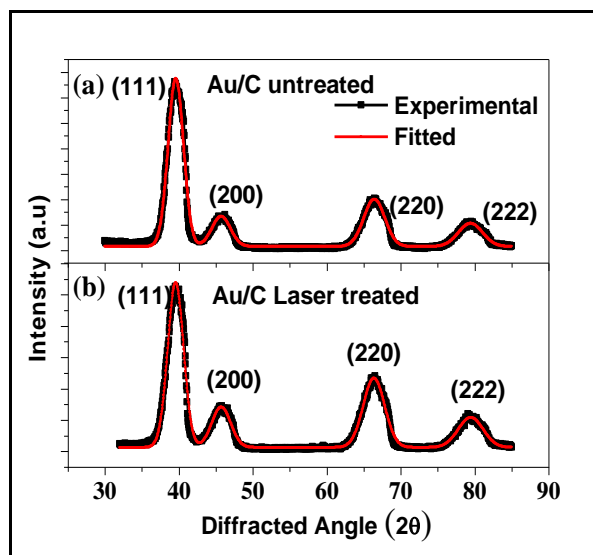


Figure 6.8: Grazing incidence X-ray diffraction spectra of carbon coated Au samples (a) before (b) after IR laser treatments for carbon removal.

The peak positions and the width after laser exposure not vary, it indicates that after surface treatment any kind of stress (compressive/tensile) is not induce inside the Au layer after laser treatments. The area intensity ratios of (200), (220) and (222) peaks with respect to (111) peak is calculated and it is observed that ratio of (220) to (111) peak increase from 0.38 to 0.56 after laser treatment. The increase in intensity ratio of (220) peak with respect to (111) peak indicates that after surface treatments bulk morphology of Au layer changed by re-orientations of crystallites. The bulk structural changes by irradiating metal thin films by UV light, plasma and laser are observed by various groups [123], [124],[148], [149].

The surface characterization results of soft x-ray reflectivity showed that carbon from Au surface was completely removed and surface roughness did not increase after surface treatment. A low density thin surface layer was observed after the carbon removal which might be formed due to interaction of cleaned surface with the ambient environment. The Raman spectroscopy and XPS results still showed presence of carbon on the laser treated sample surface. GIXRD results showed that after laser treatment reorientation of grains in Au layer occurs resultant (111) planes intensity goes down whereas (220) planes intensity increased.

6.7 Comparison of IR Laser Cleaning with UV and RF Plasma Cleaning

We have used three different techniques for removing carbon from mirror like surfaces and their results are discussed in this and previous two chapters. Here we compare the surface characterization results of carbon removing using these techniques. For comparison carbon from a uniform sample (Si-substrate/Cr-75Å/Au-730Å/C-180Å) surfaces are removed using UV radiations, RF plasma and IR laser techniques independently. The detailed surface characterization was carried out using surface analysis techniques [150]. The results of surface analyses are discussed in this section.

6.7.1 Surface and Bulk Properties after Carbon Removal

Surface and bulk structure properties after surface treatments were analyzed by soft x-ray reflectivity and grazing angle x-ray diffraction respectively. Figure 6.9a shows experimentally measured and fitted angle dependent x-ray reflectivity spectra of

pristine Au thin film with carbon layer and after carbon removal using three different techniques. The x-ray reflectivity measurements and data fitting procedure are discussed in section-6.6.1. The interference fringes and the reflectivity dip at carbon critical momentum in the reflectivity pattern of untreated carbon coated sample is an indication of carbon presence, whereas in the curves of treated samples with RF plasma, UV radiations and IR laser, there is clear absence of interference fringes and reflectivity dip at carbon critical momentum (vertical dashed line in figure 6.9a indicates carbon critical momentum (q_c)), figure 6.9b shows relative optical density (OD) profile of materials in the sample before and after surface treatments for carbon cleaning.

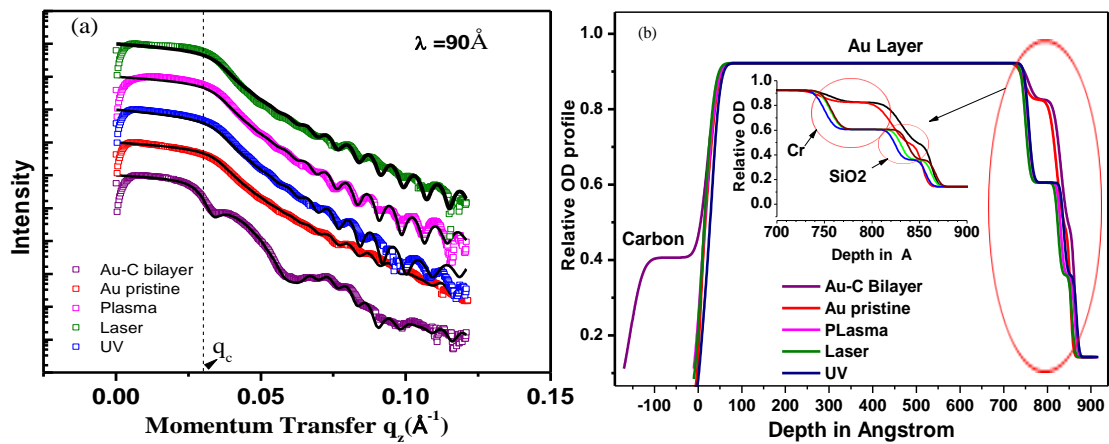


Figure 6.9: (a) Measured and fitted soft x-ray reflectivity spectra (b) Relative optical density profile of carbon coated Au surface, before and after carbon layer removal with UV, RF plasma and IR laser techniques. Vertical dashed line in (a) represents carbon critical momentum position on x -axis. Reprinted with permission from [150] © The Optical Society.

The best fitted values of optical constants and structural parameters are shown in table-6.2. The tabulated values clearly reveal that the structural and optical parameters of Au layer not vary after carbon layer removal with UV, RF plasma and IR laser

technique. After carbon removal, a 19.7 Å to 26.8 Å thin layer is observed on the Au top surface, which is 18.1 Å thick ($\delta=9.33\text{E-}3$, $\beta=1.02\text{E-}3$) in case of pristine Au sample. The β/δ ratio of this additional layer at 90 Å wavelength ranges from 2.2×10^{-1} to 6.6×10^{-1} , whereas for graphitic carbon it is $\sim 1.2 \times 10^{-1}$.

Table- 6.2: Optical and structural parameters obtained by soft x-ray ($\lambda= 90\text{Å}$) reflectivity curve fittings of carbon coated Au film before and after carbon layer removal using UV, RF plasma and IR laser surface exposures.

Layers →		C	Au	Cr	SiO ₂	Si-substrate
Treatments ↓						
Untreated Au	δ	0.00933	0.0335	0.03	0.017	0.0052
	β	0.00102	0.00928	0.015	0.0169	0.016
	t (Å)	18.12	724	74.45	32.07	Bulk
	σ (Å)	7	18	12.51	12.41	5
Untreated Au/C	δ	0.0147	0.0335	0.030	0.017	0.0052
	β	0.00202	0.00928	0.015	0.017	0.016
	t (Å)	178	734	74.4	32.07	Bulk
	σ (Å)	23.3	18	12.5	12.41	5
UV treated	δ	0.00747	0.0335	0.022	0.013	0.0052
	β	0.00496	0.00928	0.015	0.1698	0.016
	t (Å)	26.8	726	80.49	29	Bulk
	σ (Å)	8.95	15.15	8.31	6.21	5
RF plasma treated	δ	0.0212	0.0335	0.022	0.013	0.0052
	β	0.0048	0.00928	0.015	0.1698	0.016
	t (Å)	25.6	726	74.45	32	Bulk
	σ (Å)	15.89	15.15	8.31	6.21	5
IR laser treated	δ	0.0182	0.0335	0.022	0.013	0.0052
	β	0.0048	0.0093	0.015	0.1698	0.016
	t (Å)	19.7	726	74.45	32	Bulk
	σ (Å)	13.9	15.15	8.31	6.21	5

Figure 6.10 shows reflectivity versus photon energy spectra measured in 100 eV to 300 eV energy range for untreated and treated sample surfaces. The UV and rf plasma cleaned samples show reflectivity gain in carbon K-edge absorption region and the reflected intensities of these samples are closely matches with the pristine Au surface reflected intensity. The laser treated sample also shows increase in reflected intensity in carbon K-edge but not upto pristine Au sample reflectivity. This indicates that after

laser cleaning carbon not completely removed from Au surface. The sample also shows a decrease in reflected intensity in 100 eV to 200 eV region compared to pristine Au as well as untreated carbon coated Au surface. The fitting results of angle dependent reflectivity do not show presence of carbon after the laser treatment. The layer present on top surface of Au also not have same optical constant as graphitic carbon. This indicates that carbon on Au surface is not present as a continuous layer but it is dispersed on Au surface, which may be due to redeposition of ablated carbon particulates. Due to overlap of carbon edge at 284 eV and destructive interference fringe the unexposed carbon coated Au sample show a dip at 280 eV instead of 284 eV. This does not mean that the carbon edge shifts toward lower energy. Semaltianos et al. [151] also observed similar type of redeposition of debris of Si particles around ablated zone. The presence of carbon is also confirmed by XPS and Raman spectroscopy techniques (discussed in section 6.7.2).

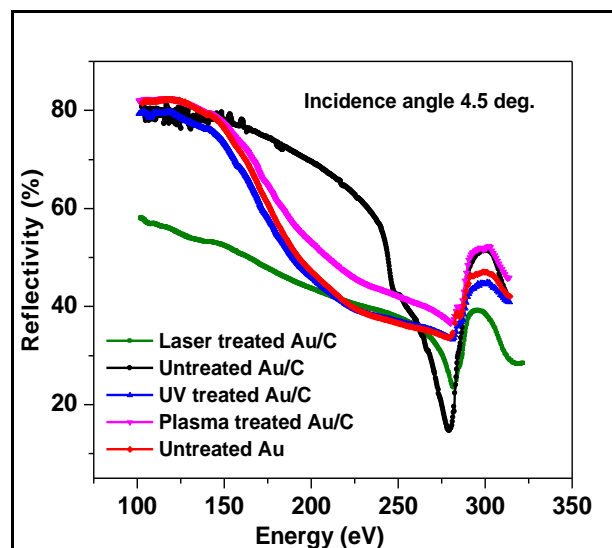


Figure 6.10: Energy dependent soft x-ray reflectivity spectra of untreated carbon coated Au film surface, before and after carbon layer removal and pristine Au thin film surface. Reprinted with permission from [150] © The Optical Society.

Bulk structural changes in the Au layer are determined by x-ray diffraction after different surface treatments and results are compared with pristine sample (shown in Figure 6.11). In pristine as well as treated samples, intensity of (111) planes is found highest in comparison to other planes intensity; it indicates that number of grains oriented in (111) direction are higher compare to other direction. The peak positions and the width of the peaks are not change after surface treatments; it indicates that after surface treatments *d*-spacing of any planes did not change after all three treatments. The area intensity ratios of (200), (220) and (222) peaks with respect to (111) peak is calculated (shown in Figure 6.12) and it is observed that ratio of (220) to (111) peak increase from 0.38 to 0.56 after laser and plasma treatments whereas after UV treatment this ratio increase from 0.38 to 0.53, other peak intensity ratios not vary so much. The increase in intensity ratio of (220) peak with respect to (111) peak indicates that after surface treatments bulk morphology of Au layer changes by reorientations of crystallites. Intensity ratios indicate that in laser and plasma treated samples grain reorientation is higher in comparison to UV treated sample. The angle dependent reflectivity shows that reorientation of crystallites not affect surface roughness.

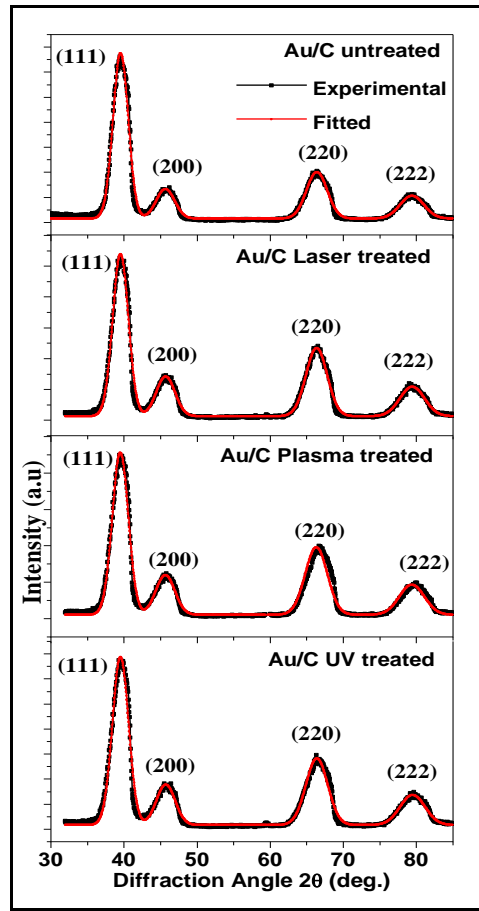


Figure 6.11: Grazing incidence X-ray diffraction spectra of untreated carbon coated Au film surface, before and after carbon layer removal and pristine Au thin film surface.

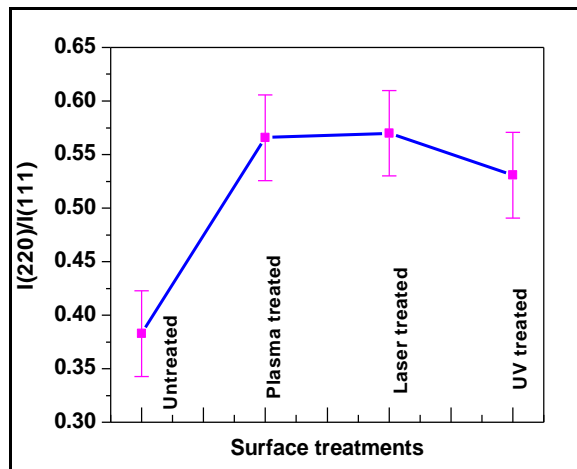
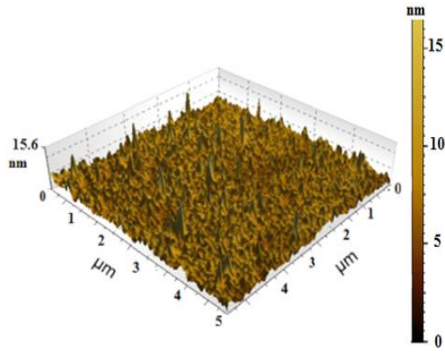


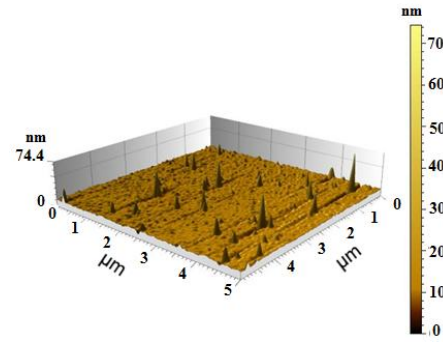
Figure 6.12: Diffraction peak area intensity ratios of Au (220) to Au (111) peak before and after different surface treatments.

The laser treated sample shows a loss in energy dependent reflectivity in 100 eV to 300 eV energy region compared to pristine Au as well as unexposed carbon coated Au surface. The fitting results of angle dependent reflectivity spectra does not show any increase in surface roughness after the laser exposure. The reasons of reflectivity loss are further analyzed by measurement of surface morphology using atomic force microscopy and presence of carbon by XPS and Raman spectroscopy measurements.

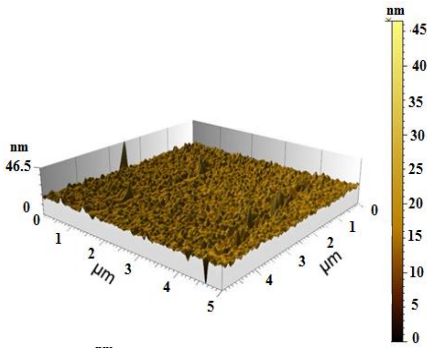
The top surface morphology of all the samples was imaged by AFM measurements. Three dimensional surface morphology images ($5\ \mu\text{m} \times 5\ \mu\text{m}$) with root mean square (σ_{rms}) are shown in Figure 6.13. The surface morphology images clearly reveals that after UV and plasma treatment for carbon removal the surface roughness decreases from $24.0\ \text{\AA}$ to $16.0\ \text{\AA}$ and $8.0\ \text{\AA}$ respectively whereas after laser treatment surface roughness increases from $24.0\ \text{\AA}$ to $56.0\ \text{\AA}$. The inconsistency in result of AFM and XRR measurements was also seen in previous studies [152]-[153]. Lee et al. [153] obtained surface roughness variation in Mo thin films by AFM and XRR by more than five times.



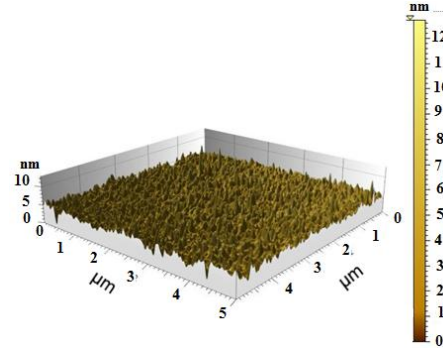
(a) Untreated Au, $\sigma_{\text{rms}} = 13.0 \text{ \AA}$



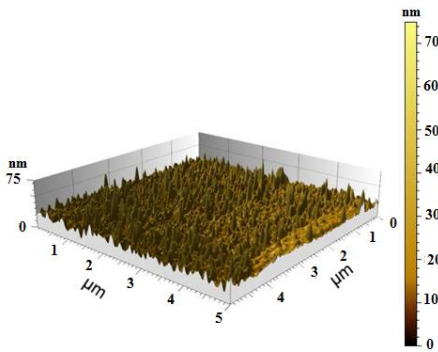
(b) Untreated Au/C, $\sigma_{\text{rms}} = 24.0 \text{ \AA}$



(c) UV treated Au/C, $\sigma_{\text{rms}} = 16.0 \text{ \AA}$



(d) Plasma treated Au/C, $\sigma_{\text{rms}} = 8 \text{ \AA}$



(e) IR Laser treated Au/C, $\sigma_{\text{rms}} = 56.0 \text{ \AA}$

Figure 6.13: Atomic force microscopic images ($5 \times 5 \mu\text{m}^2$) of (a) Pristine Au (b) Unexposed Au/C (c) UV exposed Au/C (d) Plasma exposed Au/C (e) IR laser exposed Au/C. Reprinted with permission from [150] © The Optical Society.

They concluded that low density particles cannot be detected by XRR whereas these particles easily detected by noncontact mode of AFM. Here we can also expect that after laser treatment for carbon cleaning the surface roughness increases by low

density particles that are dispersed on Au surface during laser scanning for carbon removal.

6.7.2 Chemical Property of Surfaces after Carbon Cleaning

X-ray photoelectrons spectra of untreated and treated samples in C (1s) region (280 to 295 eV) are shown in Figure 6.14. Shift in C(1s) peak position after surface treatments was not observed, this indicates that remaining carbon phase does not change after any surface treatment. In order to compare the intensity of carbon peaks, measured spectra are normalized with synchrotron ring current. The original recorded spectra are fitted by deconvolution using “XPSPEAK” program [88]. The deconvolution process included the subtraction of Shirley-type backgrounds from each spectrum and the fitting of XPS peaks with Gaussian (80%)-Lorentzian (20%) functions.

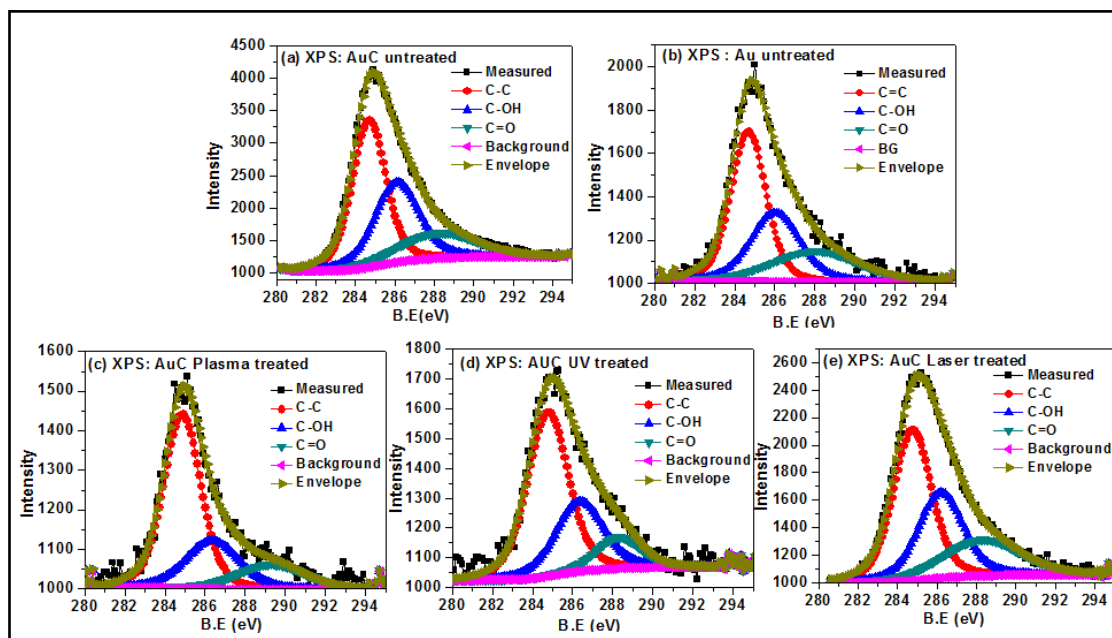


Figure 6.14: Deconvoluted XPS spectra in C (1s) (a) untreated Au/C (b) pristine Au (c) Au/C plasma treated (d) Au/C UV treated (e) Au/C laser treated sample surfaces. Reprinted with permission from [150] © The Optical Society.

For comparison, ratio (R) of total integrated areas under C(1s) peak and area under C-C(284.6 eV), C-OH(286.1eV) and C=O(288.2 eV) peaks to area under C(1s) and C-C, C-OH, C=O peak of pristine Au sample respectively calculated and plotted in Figure 6.15. The peaks area intensity ratios clearly reveal that after surface treatments using plasma and UV light the carbon gets completely removed and carbon concentration on Au surface is reduced to even concentration of adsorbed hydrocarbons on pristine Au surface. On the other hand in laser treated sample the area intensity ratio of all the peaks reduced significantly but it is still higher than the pristine Au sample as well as plasma and UV treated samples. Singh et al. [47] also analyzed Au surface XPS, after carbon removing with IR laser. They observed that presence of carbon signal in XPS may be due to ambient carbon adsorbed on the surface of Au.

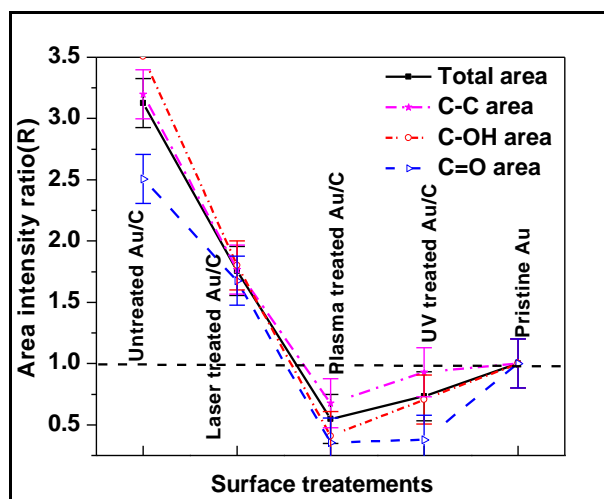


Figure 6.15: XPS C (1s) peak area intensity ratio of untreated Au/C, pristine Au, laser, plasma and UV treated Au/C to untreated Au, obtained using XPS. Reprinted with permission from [150] © The Optical Society.

The x-ray reflectivity results reveals that carbon is completely removed from Au surface after UV, RF plasma and IR laser surface treatment, but XPS results indicates that carbon on laser treated sample surface still present with less concentration

compare to unexposed carbon coated Au sample. To confirm the results of soft x-ray reflectivity and XPS, a more sensitive technique (Raman spectroscopy) with respect to carbon was used to determine presence of carbon on surface treated samples.

Figure 6.16 shows Raman spectra from pristine Au surface, carbon coated Au and after carbon removals using three different techniques. After carbon removal using UV radiations and RF plasma the Raman spectra are well coincide with pristine Au sample spectrum. It indicates that carbon from Au surface completely removed. Presences of various low intensity peaks in pristine as well as in UV and plasma treated samples are due to adsorbed ambient hydrocarbons on the Au surface. The laser treated sample still show presence of carbon. The first order spectra of laser treated sample and carbon coated untreated sample are fitted by peak fit program by considering mixed Lorentzian and Gaussian functions. In both spectra G and D bands of graphitic carbon with an additional band known as shoulder of D band at 1180 cm^{-1} (D4) are observed. The G-band center around 1560 cm^{-1} and is due to an ideal lattice vibration mode with E_{2g} symmetry and show the presence of sp^2 hybridized carbon. In laser treated sample splitting in G band into two bands G (1560 cm^{-1}) and (D2) 1600 cm^{-1} is observed. This type of splitting in graphitic sample occurs due to random distribution of impurities, the localized vibrations mode of impurities interact with extended phonon modes of graphene resulting splitting in G band observed [154]. The D band indicates presence of disorder in carbon ring and is related to the breathing of the carbon hexagons. Decrease in D band intensity indicates that number of carbon rings as well as disordering in given sample decrease. The D4 peak center around 1180 cm^{-1} is attributed to presence of sp^2 - sp^3 mixed phase of carbon. Dippel et al.

[126] reported this band at $\sim 1190\text{ cm}^{-1}$ in the Raman spectra of flame soot and attributed to sp^2 - sp^3 bonds or C-C and C=C stretching of vibrations of polyene like structures. XPS and Raman spectroscopy both techniques show presence of carbon after laser cleaning but intensity in both the cases decreased from pristine carbon coated sample.

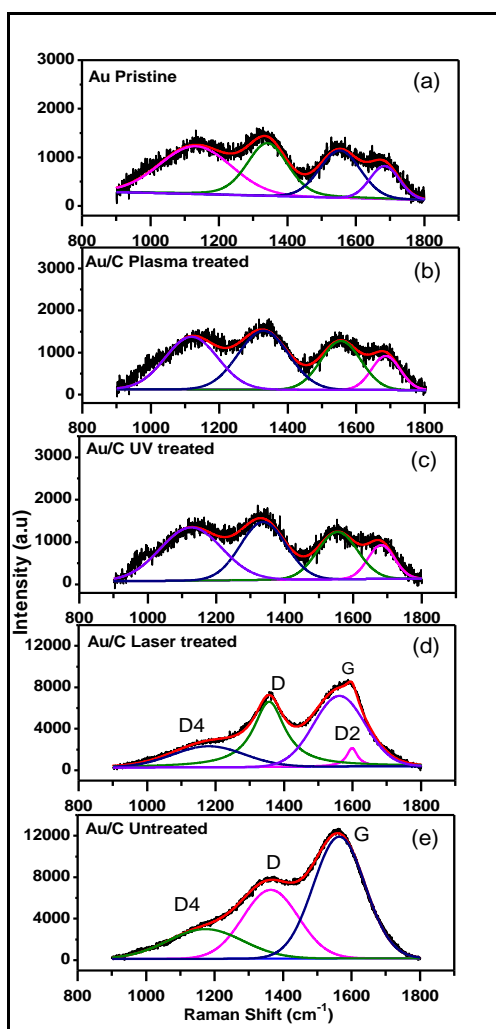


Figure 6.16: Raman spectra of carbon coated Au film before and after different treatments for carbon removal. (a) Pristine Au (b) Plasma treated (c) UV treated (d) Laser treated (e) Au/C untreated. Various peaks (G, D, D2, D4) related to graphitic carbon are indicated in (d) and (e). Reprinted with permission from [150] © The Optical Society

6.8 Summary

Here carbon from mirror like Au thin film surface is removed by IR laser scanning from carbon coated Au sample surface. After carbon removal from identical Au surfaces using IR laser, RF plasma and UV radiation, three independent samples were characterized by several surface analysis techniques. Soft x-ray reflectivity results clearly showed that carbon from Au surface is completely removed and surface roughness did not increase after surface treatment with all three different techniques. A 19.7 Å to 26.8 Å thick layer on Au surface was observed after the carbon removal. The β/δ ratio of this layer vary from 2.2×10^{-1} to 6.6×10^{-1} , this ratio does not matches with graphitic carbon β/δ ratio (1.2×10^{-1}). The Raman spectroscopy and XPS results still showed presence of carbon in the laser treated sample surface. Comparison of UV and plasma cleaned samples showed a gain in the soft x-rays reflectivity in carbon K-edge region and the reflected intensity of these samples closely matches with the pristine Au thin film intensity. The laser treated sample also shows increase in reflected intensity in carbon K-edge but not upto pristine Au sample reflectivity. The sample show a decrease in reflected intensity in 100 eV to 200 eV region compared to pristine Au as well as untreated carbon coated Au surface. GIXRD results showed that after surface treatment reorientation of grains in Au layer occurs, (111) planes intensity goes down whereas (220) planes intensity increased. Comparative study results suggest that rf plasma and UV radiation techniques are good for carbon cleaning whereas in IR laser cleaning some carbon particulates resettled on the cleaned surface from the removal debris of carbon.

Appendix-I

Adsorption Rate of Hydrocarbons [155],[156]

Adsorption Rate (R_a): According to kinetic theory of gases, the rate of gas adsorption (R_a) is proportional to the rate of collision (R_c) of molecules with the surface.

$$R_a = S \cdot R_c \quad (\text{I.1})$$

Where S is a proportionality constant, which represents probability of adhesion of colliding molecules on surface. The rate of collision is also related to temperature (T) (kinetic energy of gas molecule) and partial pressure (P) of gas molecules, corresponding collision rate equation is given by

$$R_c = \frac{P}{\sqrt{2\pi m k_B T}} \left(\frac{\text{molecules}}{\text{area} \cdot \text{sec}} \right) \quad (\text{I.2})$$

Where k_B is Boltzmanns constant and m is mass of gas molecule. Whether a molecule will adsorb or reflect (stick or not stick), it depends on two main factors: first one is activation energy of surface and second one is the configuration of molecule. If the fraction of molecules that possessing the required activation energy are, $\exp\left(-\frac{E_a}{k_B T}\right)$, where E_a is the activation energy of adsorption (the magnitude of E_a decides that the process of adsorption is physical or chemical) and the configuration probability that a molecule will occupy a single site is proportional to the fraction of unoccupied surface $(1 - n)$, where $n = \frac{N}{N_{max}}$ is the fractional of surface coverage. With the consideration of temperature, activation energy for adsorption and fraction of unoccupied sites on surface, the sticking probability S can be written as

$$S = \alpha(1 - n) \exp\left(\frac{-E_a}{k_B T}\right) \quad (I.3)$$

α - is a proportionality constant known as condensation coefficient. Using equation (I.1), (I.2) & (I.3) we get a final adsorption rate expression.

$$R_a = \frac{P}{\sqrt{2\pi m k_B T}} \cdot \alpha(1 - n) \exp\left(\frac{-E_a}{k_B T}\right) \left(\frac{\text{molecules}}{\text{area} \cdot \text{sec}}\right) \quad (I.4)$$

The adsorption rate decreases rapidly with increasing surface coverage; it reveals that the activation energy increases with the surface coverage (n). The condensation coefficient (α) also varies with surface coverage. These variations are caused by surface heterogeneity, the heterogeneity on surface occurs due to different values of condensation coefficient (α) and activation energy E_a . The most active sites are associated with lowest activation energy. Further, the interaction between occupied and unoccupied site also affects the rate of adsorption, hence (α) and (E_a) should be represented as function of (n)

$$R_a = \frac{P}{\sqrt{2\pi m k_B T}} \cdot \alpha(n)(1 - n) \exp\left(\frac{-E_a(n)}{k_B T}\right) \left(\frac{\text{molecules}}{\text{area} \cdot \text{sec}}\right) \quad (I.5)$$

Desorption Rate (R_d): As we have discussed that the adsorbed gases present on the surface are weakly bonded to the surface. When the adsorbed molecules receive energy greater than or equal to the energy of adsorption, it will leave the surface, this process is known as desorption. The adsorption and desorption phenomena happen simultaneously on surfaces. In equilibrium condition, the rate of adsorption and desorption are equal and rate of desorption is given by Polanyi –Wigner equation

$$R_d = \frac{-dN}{dt} = \beta n_a^m \exp\left(\frac{-E_d}{k_B T}\right) \left(\frac{\text{molecules}}{\text{area} \cdot \text{sec}}\right) \quad (\text{I.6})$$

Where, E_d is activation energy for desorption, β is the pre-exponential factor of desorption rate coefficient, n_a^m is the fraction of binding sites for the adsorbed molecules and m is kinetic order for desorption process. Kinetic order suggests the nature of elementary steps that governs desorption. A zero-order kinetics indicates that desorption occurs from multilayers, where desorption is independent of coverage. A first order kinetics indicates the presence of single surface species whereas second order kinetics indicates recombination of adsorbed atoms leading to production of a diatomic molecule on surface before it desorption.

Reflection Rate (R_f): When gas molecules strikes to the surface, there are two possible events may happen on the surface, the first one is the adsorption of gas molecule on the surface and the second one is the reflection of gas molecule from the previously adsorbed gas molecules. For calculating the rate of reflection from a given surface, first consider a partially filled surface with gas molecules. Let n is the fraction ($n = \frac{N}{N_{\max}}$) of filled sites on the surface, here N_{\max} are maximum sites at which gas molecules can be adsorbed. With consideration of filled sites the rate of reflected molecules can be written as $R_f = nR_c$. After implication the value of R_c from equation (3), the rate of reflected atoms from surface is given by

$$R_f = n \cdot \frac{P}{\sqrt{2\pi m k_B T}} \left(\frac{\text{molecules}}{\text{area} \cdot \text{sec}}\right) \quad (\text{I.7})$$

Appendix-II

Derivation for Secondary Yield Emission [5]

The generation of photoelectron and subsequently the secondary electron yield is a material dependent quantity. During carbon contaminations initially the electron yield is from the optical coating material, as contamination grows the secondary electron yield from contamination material and optical coating material both contributes. In this section we derive an expression for secondary electron yield (J_{SE}) as a function of photon intensity and carbon layer thickness D .

The number of photons absorbed per unit time into the sample surface $N_p(0)$ is directly proportional to the incident photons flux (I_0), exposed area (A_0) and $(1-R)$, where R is the reflectivity of optic surface.

$$N_p(0) = I_0 A_0 (1 - R) \quad (\text{II.1})$$

The differential rate of photons dN_p absorbed in thickness dz of optical coating material is

$$dN_p = -\mu N_p dz \quad (\text{II.2})$$

Where μ is the linear adsorption coefficient in cm^{-1} unit, the negative sign indicated as thickness increases the number of photons decreases due to absorption. Integrating Eq. (II.2) from the surface at $z = 0$ to a depth z leads to the number of photons absorbed at any depth z in the material:

$$N_p(z) = N_p(0) \exp(-\mu z) \quad (\text{II.3})$$

For simplicity we assume that dominant absorption process is photoelectric emission and one photo-electron is generated per absorbed photon, so that the differential rate

of photoelectrons (dN_e) generated in the differential thickness dz is the negative of the differential rate of photon absorption

$$dN_e = -dN_p = \mu N_p dz \quad (\text{II.4})$$

From equation (II.3) & (II.4)

$$dN_e = \mu N_p(0) \exp(-\mu z) dz \quad (\text{II.5})$$

From equation (II.1) & (II.5)

$$dN_e = \mu I_0 A_0 (1 - R) \exp(-\mu z) dz \quad (\text{II.6})$$

Before reaching the primary electrons on the surface of optics it scatters elastically and in-elastically which leads to generation of low energy secondary electrons. This process is described mathematically as the attenuation of the single primary electron multiplied by a gain factor $G_e(h\nu)$ which is an energy dependent parameter. The gain factor can be described as $G_e(h\nu) = \frac{\Omega}{4\pi} h\nu M$, where M is a material constant.

$$dI_{SE} = dN_e \exp\left(-\frac{z}{L}\right) \frac{\Omega}{4\pi} h\nu M \quad (\text{II.7})$$

Where L is the scape length of electrons inside the material.

$$dI_{SE} = \mu I_0 A_0 (1 - R) \exp\left(-\left(\mu + \frac{1}{L}\right)z\right) dz \frac{\Omega}{4\pi} h\nu M \quad (\text{II.8})$$

This expression describes differential rate (dI_{SE}) of generation of secondary electrons at optics surface. The photo absorption coefficient μ is very small in comparison to the ($1/L$), so the photo absorption coefficient (μ) may be neglected from equation (II.8). Additionally the solid angle for half spherical volume above the optic $\Omega = 2\pi$, with these assumptions equation (II.8) reduces to

$$dI_{SE} = \mu I_0 A_0 (1 - R) \exp\left(-\left(\frac{1}{L}\right)z\right) dz \frac{h\nu}{2} M \quad (\text{II.9})$$

The total rate of secondary electrons (I_{SE}) escaping the surface of the optics is determined by integrating equation (II.9) over the thickness of the optics.

$$I_{SE} = \int dI_{SE} = I_0 A_0 (1 - R) \frac{h\nu}{2} \int_{z=0}^{\infty} M \exp\left(-\left(\frac{z}{L}\right)\right) \mu dz$$

Let us consider the thickness of the contamination is D, so we split the integral at thickness D (contaminant/optics material)

$$I_{SE} = I_0 A_0 (1 - R) \frac{h\nu}{2} \left[\int_{z=0}^D M_c \exp\left(-\left(\frac{z}{L_c}\right)\right) \mu_c dz + \int_{z=D}^{\infty} M_{Au} \exp\left(-\left(\frac{z}{L_{Au}}\right)\right) \mu_{Au} dz \right]$$

$$I_{SE} = I_0 A_0 (1 - R) \frac{h\nu}{2} \left[\left[-M_c L_c \mu_c \exp\left(-\left(\frac{z}{L_c}\right)\right) \right]_0^D + \left[-M_{Au} L_{Au} \mu_{Au} \exp\left(-\left(\frac{z}{L_{Au}}\right)\right) \right]_D^{\infty} \right]$$

$$I_{SE} = I_0 A_0 (1 - R) \frac{h\nu}{2} \left[\left[M_c L_c \mu_c \left(1 - \exp\left(-\left(\frac{D}{L_c}\right)\right)\right) \right] + \left[M_{Au} L_{Au} \mu_{Au} \exp\left(-\left(\frac{D}{L_{Au}}\right)\right) \right] \right] \quad (\text{II.10})$$

M_c , L_c , μ_c and M_{Au} , L_{Au} , μ_{Au} denotes material constants, escape length of electrons and photo absorption coefficient for carbon and gold materials respectively.

Appendix-III

Different Type of UV Radiation Sources [157]–[161]

Sun is the universal source of radiations, which emits all three kind of UV radiation i.e. UV-A (315-400 nm), UV-B (280-315 nm) and UV-C (100-280 nm). In EM spectrum, UV radiation spectrum lies in between visible light and X-rays Figure 1. The man-made sources that emit radiations in this region are mercury lamp, excimer (excited dimmers) lamps and lasers and the most important source is the synchrotron radiation source which emits photons in broad spectrum of energy, starts from infrared to hard x-rays. Brief description about these sources is given below:

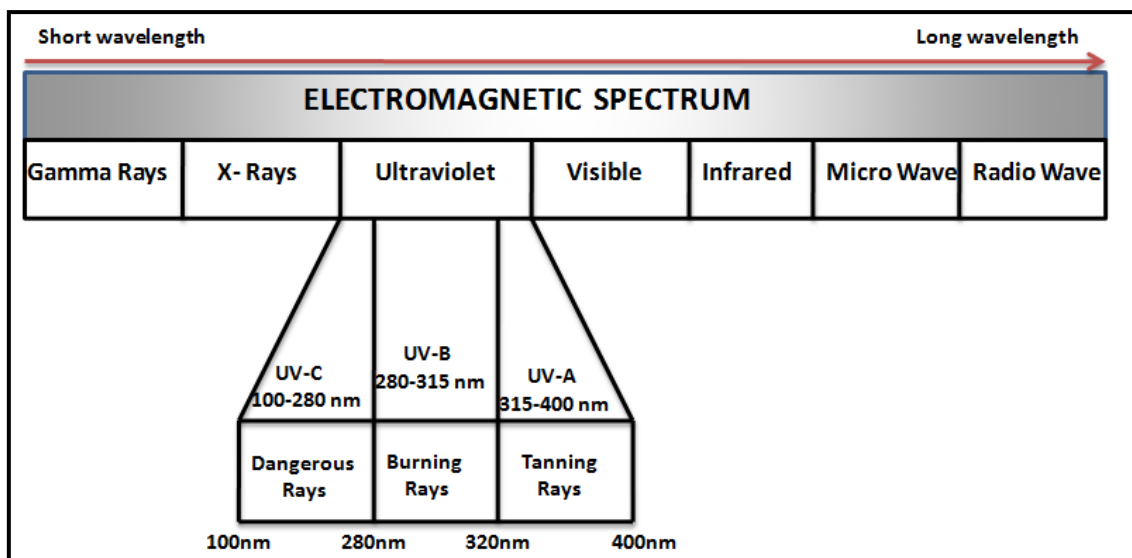


Figure 1: Typical electromagnetic wave spectrum start from radio waves (low energy) to gamma waves (high energy).

(a) Mercury Lamp

For laboratory applications particularly for short wavelengths UV radiations, low pressure mercury (Hg) vapor lamps are highly efficient source. A mercury-vapor

lamp is a gas discharge lamp that uses an electric arc through which excitation of vaporized mercury atoms take place and subsequent de-excitation process produce UV and visible radiations. The radiations emitted by the Hg discharge lamp also depend on envelope use to make the lamp. In low pressure (10^{-2} mbar) mercury lamps re-absorption of emitted UV radiation is weak, resultant resonance lines at 184.9 nm and 253.7 nm wavelengths are dominant lines. The synthetic quartz and borosilicate glass based lamps have good transmittance for both 184.9 nm and 253.7 nm wavelength radiations. The typical wavelengths emitted by a mercury lamp are given in table-1. The 184.9 nm and 254.7 nm wavelength radiations emitted by low pressure mercury lies in UV-C region and are useful for decomposition of organic layers. The 184.9 nm wavelength radiations also have large dissociation cross-section for dissociating oxygen molecule and generally used for ozone production.

Table 1: Typical radiations emitted by a low pressure mercury lamp

Wavelength (nm)	Line	Color
184.9		UV-C
253.7		UV-C
365.4	I-Line	UV-A
404.7	H-Line	Violet
435.8	G-Line	Blue
546.1		Green
578.2		Yellow-orange

(b) Excimer Lamp

Excimer means joining of two molecules or atoms of the same chemical composition in an excited state, if two atoms are not same chemical composition then it is known as exciplex. Excimer lamps are quasi-monochromatic radiations sources. Depending upon excimer molecules excimer lamp gives radiations in UV to VUV energy range.

The UV radiations are generated by spontaneous transitions from bound excited excimer electronic states to weakly bound or unbound ground states, with release of UV photons. For example: In a Xenon (Xe) excimer lamp after excitation with an electric discharge high-energy Xe atoms form excited dimer molecules (Xe_2). When these excited dimers decay into ground state they release UV photons of 172 nm wavelength. The typical excimer molecule emission process reaction can be understood as following.



The wavelengths emitted by different dimmers are given in table-2.

Table 2: The energy (eV) emitted by different dimer/excimer molecules.

Exciplex Molecule	Energy (eV)	Excimer Molecule	Energy (eV)
NeF	11.48	Ar ₂	9.84
ArBr	7.51	Kr ₂	8.49
ArCl	7.08	F ₂	7.84
KrI	6.52	Xe ₂	7.20
ArF	6.42	Cl ₂	4.78
KrBr	5.99	Br ₂	4.29
KrCl	5.58	I ₂	3.62
KrF	5.02		
XeI	4.90		
XeBr	4.39		
XeCl	4.02		
XeF	3.53		

(c)Excimer Laser

An excimer lasers uses mixer of noble and halogen gases as a lasing medium. In excimer lasers electrical discharge excites the gas atoms; subsequently excited atoms form a temporarily excited state compound of noble halides. When these excited compounds decay, they release UV photons. There is no stable ground state so

population inversion needs for laser action is easily obtained. The excimer lasers are pulsed devices, the typical pulse duration lies in nano-second range. Some examples of excimer lasers are ArF excimer lasers ($\lambda = 193$ nm), KrF excimer lasers (wavelength $\lambda = 248$ nm), XeCl excimer lasers ($\lambda = 308$ nm), and XeF excimer lasers ($\lambda = 351$ nm). The excitation and emission process is same as in case of excimer lamp, the difference is that excimer lasers are pulsating and give high intensity compare to UV lamp.

(d) Synchrotron Radiations as UV Source

Synchrotron radiation sources are more popular in field of material research due to wide range of energy tunability, high energy and high intensity. These sources emit radiations in infrared to hard x-ray energy region, which cover full energy spectrum of ultraviolet radiation. The total power radiated by relativistic electrons, that's are force to move along the circular path with a radius of curvature R is given by Schwinger formula.

$$P = \frac{e^2 c \gamma^4}{6 \pi \epsilon_0 R^2} \quad (\text{III.1})$$

Where e – electron charge, c - speed of light, γ - relativistic factor, ϵ_0 – permittivity of free space.

Total power radiated by N electrons can be written as

$$P = \frac{e^2 c \gamma^4}{6 \pi \epsilon_0 R^2} N = \frac{e I_b \gamma^4}{3 \epsilon_0 R} \quad (\text{III.2})$$

Where I_b (beam current) = $\frac{N e c}{2 \pi R}$

Frequency (ω) distribution of radiated power is given by

$$\frac{dP}{d\omega} = \frac{\sqrt{3} e^2 \gamma \omega}{4 \pi \epsilon_0 c \omega_c} \int_{\frac{\omega}{\omega_c}}^{\infty} \kappa_{\frac{5}{3}}(x) dx = \frac{2 e^2 \gamma}{9 \epsilon_0 c} S(y) \quad (\text{III.3})$$

$$S(y) = \frac{\omega R}{3 c \gamma^3} (1 + \gamma^2 \theta^2)^{\frac{3}{2}} \quad (\text{III.4})$$

Where ω_c is critical frequency and given by $\omega_c = \frac{3c\gamma^3}{2R}$ and $\kappa(x)$ is modified Bessel function with argument $x = \frac{1}{2} \frac{\omega}{\omega_c} (1 + \gamma^2 \theta^2)^{3/2}$, where θ is angle normal to deflecting plane.

The photon flux radiated from bending magnet source at Indus-1 parameters (B =1.5 Tesla, I= 100 mA and bending radius R= 1 meter) are calculated by CXRO (web based program) [27] and shown in Figure 2.

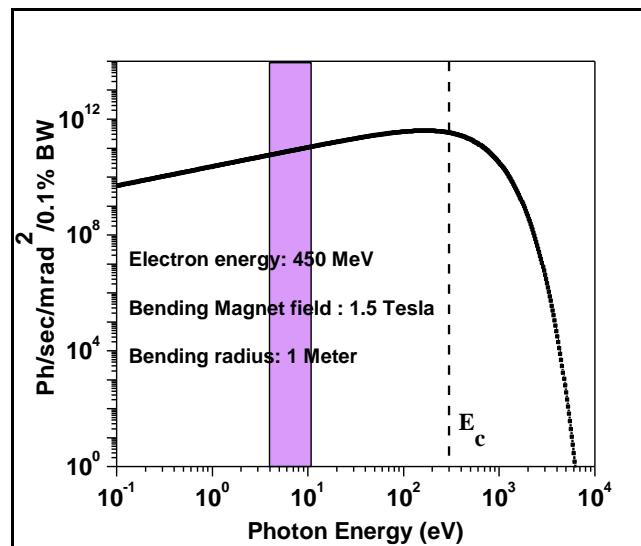


Figure 2: Spectral distribution of synchrotron radiations (Indus-1) as a function of energy, purple color represent ultraviolet radiation energy range.

Appendix-IV

Mathematical expressions for thermal expansion force, laser pulse width for vaporization temperature and for ablation rate and depth [132], [133] [162]–[167]

The thermal expansion force (cleaning force) is given by

$$F_c = \gamma E \nabla T(0, t) \quad (\text{IV.1})$$

Where, γ is linear thermal expansion coefficient, E is modulus of elasticity and $\nabla T(0, t)$ is the temperature rise in time interval $t = 0$ to t .

If $T(0, t) = T_v$ is the vaporization temperature and $t = t_v$ is the laser beam pulse width to achieve the vaporization temperature than t_v can be written as

$$t_v = \frac{k}{\pi} \left(\frac{2\alpha F_a}{KT_v} \right)^2 \quad (\text{IV.2})$$

Where k - thermal diffusivity, K is thermal conductivity, F_a is absorbed laser fluence, T_v laser fluence t_v is laser pulse width and α is absorption coefficient.

From equation (IV.2), it is clear that t_v strongly depends on F_a (absorbed fluence) and surface absorption coefficient (α), typical value of t_v varies from μs to ns for vaporization whereas the melting temperature is of the order of ms . Hence μs to ns pulse width laser beam with sufficient level of fluence must be used for efficient laser cleaning without melting the substrate and fast vaporization of contaminants. In order to remove an atom from a solid surface by laser irradiation, one needs to deliver energy greater than the binding energy of that atom. Short pulsed lasers with pulse

duration in the range of μs to ns are preferred for laser cleaning to avoid heat conduction and damage of the substrate. For thermal ablation of tightly bounded metallic coating on glass surfaces, ns duration pulses of infrared laser seems to be more suitable choice due to high energy and thermal heating requirements. For cleaning of particulates from solid surfaces, action of cleaning forces must overcome strong adhesion forces between the tiny particulates and the surface. Among these adhesion forces, Van-der-Waals force, capillary force, and electrostatic force are of prime importance. Thermal ablation rate or evaporation rate R_{evap} and ablation depth d per pulse can be determined with the help of laser intensity and laser fluence.

$$R_{evap} = \frac{I_a}{E_b} \quad (IV.3)$$

$$d = \frac{1}{\alpha_p} \ln\left(\frac{F}{F_{th}}\right) \quad (IV.4)$$

Where E_b – is binding energy per atom, I_a – is the absorbed laser intensity, $\frac{1}{\alpha_p}$ – is effective penetration depth of laser energy and F_{th} is threshold fluence. For example, for gold target binding energy $E_b = 3.37$ eV per atom and $\frac{1}{\alpha_p} = 13.7$ nm. The time t needed for the surface temperature to reach the vaporization temperature can be calculated by

$$T_s(t) - T_0 = \left[\frac{2I_a}{K} \right] \sqrt{\left(\frac{kt}{\pi} \right)} \quad (IV.5)$$

Where, $T_s(t)$ is surface temperature at a given time, I_a is the absorbed laser intensity, K is thermal conductivity ($W.m^{-1}.K^{-1}$) of the material, and k is thermal diffusivity (cm^2/s) of the material.

REFERENCES:

1. "Investigation of carbon contamination of mirror surfaces exposed to synchrotron radiation", K. Boller, R. P. Haelbich, H. Hogrefe, W. Jark and C. Kunz, *Nucl. Instrum. Methods Phys. Res.*, **1983**, 208, 273–279.
2. "Structural variation in a synchrotron-induced contamination layer (a-C:H) deposited on a toroidal Au mirror surface", P. K. Yadav, R. K. Gupta, M. K. Swami and M. H. Modi, *J. Synchrotron Radiat.*, **2017**, 24(4), 757–764.
3. "Comparison of photodesorption yields using synchrotron radiation of low critical energies for stainless steel, copper and electrodeposited copper surfaces", J. Gómez Goñi, O. Gröbner and A. G. Mathewson, *J. Vac. Sci. Technol. A*, **1994**, 12(4), 1714–1718.
4. "Vacuum technology", A. Roth, North-Holland, Second Rev. Edition 1982, 17-61.
5. "Modeling radiation-induced carbon contamination of extreme ultraviolet optics", J. Hollenshead and L. Klebanoff, *J. Vac. Sci. Technol. B*, **2006**, 24(1), 64–82.
6. "The foundation of chemical kinetics", S.W. Benson, McGraw-Hill Inc.,: New York, First Edition, **1960**.
7. "Handling the carbon contamination issue at Soleil", I. Yao-Leclerc, S. Brochet, C. Chauvet, N. De Oliveira, J.-P. Duval, J.-F. Gil, S. Kubsky, L. Nahon, F. Nicolas, F. Sirotti and M. Thomasset, *Proc. SPIE 8077*, **2011**, 807712 (1-4).
8. "Carbon contamination of soft X-ray beamlines: Dramatic anti-reflection coating effects observed in the 1 keV photon energy region", C. Chauvet F. Polack, M. G. Silly, B. Lagarde, M. Thomasset, S. Kubsky, J. P. Duval, P. Risterucci, B. Pilette, I. Yao, N. Bergéard and F. Sirotti, *J. Synchrotron Radiat.*, **2011**, 18(5), 761–764.
9. "In situ removal of carbon contamination from optics in a vacuum ultraviolet and soft X-ray undulator beamline using oxygen activated by zeroth-order synchrotron radiation", A. Toyoshima, T. Kikuchi, H. Tanaka, J. I. Adachi, K. Mase and K. Amemiya, *J. Synchrotron Radiat.*, **2012**, 19(5), 722–727.
10. "Performance of the HERMES beamline at the carbon K-edge", S. Swaraj, R. Belkhou, S. Stanescu, M. Rioult, A. Besson and A. P. Hitchcock, *J. Phys. Conf. Ser.*, **2017**, 849, 012046 (1-4).
11. "Resuscitation of carbon-contaminated mirrors and gratings by oxygen-discharge

- cleaning.1: Efficiency recovery in the 4-40-eV range”, T. Koide, M. Yanagihara, Y. Aiura, S. Sato, T. Shidara, A. Fujimori, H. Fukutani, M. Niwano and H. Kato, *Appl. Opt.*, **1987**, *26(18)*, 3884-3894.
12. “In situ optical element cleaning with photon activated oxygen”, W. K. Warburton and P. Pianetta, *Nuclear Instruments and Methods in Physics Research A* **1992**, *319*, 240–243.
 13. “Detection and characterization of carbon contamination on EUV multilayer mirrors”, J. Chen, E. Louis, Chris J. Lee¹, H. Wormeester, R. Kunze, H. Schmidt, D. Schneider, R. Moors, W. van Schaik, M. Lubomska and F. Bijkerk, *Opt. Express*, **2009**, *17(19)*, 16969-16979.
 14. “Preventing carbon contamination of optical devices for X-rays: The effect of oxygen on photon-induced dissociation of CO on platinum”, P. Risterucci, G. Held, A. Bendounan, Matthieu G. Silly, C. Chauvet, D. Pierucci, N. Beaulieua and F. Sirottia, *J. Synchrotron Radiat.*, **2012**, *19(4)*, 570–573.
 15. “Characterization of carbon contamination under ion and hot atom bombardment in a tin plasma extreme ultraviolet light source”, A. Dolgov, D. Lopaev, C. J. Lee, E. Zoethout, V. Medvedev, O. Yakushev, F. Bijkerk, *Appl. Surf. Sci.*, **2015**, *353*, 708–713.
 16. “Effect of the soft X-rays on highly hydrogenated diamond-like carbon films”, K. Kanda, K. Yokota, M. Tagawa, M. Tode, Y. Teraoka and S. Matsui, *Jpn. J. Appl. Phys.*, **2011**, *50(5)*, 055801 (1-3).
 17. “Development of refractive-index modulation type diffractive optical element using a-C:H film”, T. U. H. Matsuura, S. Ohkubo and K. Oda, *SEI, Tech. Rev.*, **2007**, *65*, 30–34.
 18. “Soft X-ray irradiation effect on the fluorinated DLC film”, H. Takamatsu, M. Niibe, X. Zhou, K. Komatsu, H. Saitoh, H Akasaka, A. Saiga, K. Tamada, M.Tagawa, K. Yokota, Y. Furuyama and K. Kanda, *Diam. Relat. Mater.*, **2017**, *79*, 14–20.
 19. “First commissioning results from high resolution vacuum ultraviolet beamline at Indus-1 synchrotron source,” P.J. Singh, A. Shastri, R. S. Kumar, S.N. Jha, S.V.N.B. Rao, R. D’Souza and B.N. Jagatap, *Nucl. Instruments Methods Phys. Res. A* **2011**, *634(1)*, 113–119.

20. “Ex-situ characterization of synchrotron radiation induced carbon contamination on LiF window”, P. K. Yadav, M. H. Modi, M. K. Swami and P. J. Singh, *J. Electron Spectros. Relat. Phenomena*, **2016**, *211*, 64–69.
21. “First results on the reflectometry beamline on Indus-1,” R. V. Nandedkar, K. J. S. Sawhney, G. S. Lodha, A. Verma, V. K. Raghuvanshi, A. K. Sinha, M. H. Modi and M. Nayak, *Curr. Sci.*, **2002**, *82(3)*, 298–304.
22. “Total electron impact ionization cross sections for simple hydrocarbon molecules”, H. Nishimurat and H. Tawara, *J. Phys. B*, **1994**, *27*, 2063–2074.
23. “Optics for coherent x-ray applications”, M. Yabashi, K. Tono, H. Mimura, S. Matsuyama, K. Yamauchi, T. Tanaka, H. Tanaka, K. Tamasaku, H. Ohashi, S. Goto and T. Ishikawa, *J. Synchrotron Radiat.*, **2014**, *21(5)*, 976–985.
24. “Reflectivity degradation of grazing-incident EUV mirrors by EUV exposure and carbon contamination”, H. Shin, J. R. Sporre, R. Raju and D. N. Ruzic, *Microelectron. Eng.*, **2009**, *86(1)*, 99–105.
25. “Carbon K-edge polarimetry with Cr/Sc multilayers”, A. Gaupp, F. Schäfers, M. MacDonald, S. Uschakow, N. N. Salashchenko and P. K. Gaykovich, *J. Phys. Conf. Ser.*, **2013**, *425 (12)*, 122013 (1-4).
26. “Refurbishment of an Au-coated toroidal mirror by capacitively coupled RF plasma discharge”, P. K. Yadav, M. Kumar, R. K. Gupta, M. Sinha, J. A. Chakera and M. H. Modi, *J. Synchrotron Radiat.*, **2019**, *26*, 1152–1160.
27. “The centre of optics (CXRO) at Berkeley National Laboratory, Berkeley, CA, USA.”, [Online]. Available: http://henke.lbl.gov/optical_constant/layer2.html.
28. “Development of contamination-free X-ray optics for next-generation light sources”, H. Ohashi, Y. Senba, H. Yumoto, T. Koyama, T. Miura and H. Kishimoto, *AIP Conf. Proc.*, **2016**, *1741*, 40023 (1-4).
29. “Etching of a-C :H films by an atomic oxygen beam,” E. B. D. Bourdon, A. Raveh, S. C. Gujrathi and L. Martinu, *J. Vac. Sci. Technol. A*, **1993**, *11(5)*, 2530–2535.
30. “Erosion of diamond films and graphite in oxygen plasma,” A. Joshi and R. Nimmagadda, *J. Mater. Res.*, **1991**, *6(7)*, 1484–1490.
31. “Hyperthermal atomic oxygen beam induced etching of HOPG (0001) studied by X-ray photoelectron spectroscopy and scanning tunneling microscopy”, H.

- Kinoshita, M. Umeno, M. Tagawa and N. Ohmae, *Surf. Sci.*, **1999**, *440*, 49–59.
32. “Spatially anisotropic etching of graphite by hyperthermal atomic oxygen”, K. T. Nicholson, T. K. Minton and S. J. Sibener, *J. Phys. Chem. B*, **2005**, *109*, 8476–8480.
 33. “Temperature dependent morphological evolution of HOPG graphite upon exposure to hyperthermal O (3 P) atoms”, K. T. Nicholson, T. K. Minton and S. J. Sibener, *Progress in Organic Coatings*, **2003**, *47*, 443–447.
 34. “Radio-frequency discharge cleaning of silicon-capped Mo/Si multilayer extreme ultraviolet optics”, S. Graham, C. Steinhaus, M. Clift and L. Klebanoff, *J. Vac. Sci. Technol. B*, **2002**, *20(6)*, 2393–2400.
 35. “Characterization, optimization and surface physics aspects of in situ plasma mirror cleaning,” E. Pellegrin, I. Sics, J. R. Herrera, C. P. Sempere, J. Josep L. Alcolea, M. Langlois, J. F. Rodriguez and V. Carlino, *J. Synchrotron Radiat.*, **2014**, *21(2)*, 300–314.
 36. “Remote plasma cleaning of optical surfaces: Cleaning rates of different carbon allotropes as a function of RF powers and distances”, M. G. Cuxart, J. Reyes-Herrera, I. Sics, A.R. Goni, H. Moreno Fernandez, V. Carlino and E. Pellegrin., *Appl. Surf. Sci.*, **2016**, *362*, 448–458.
 37. “Characterization of carbon-contaminated B₄C-coated optics after chemically selective cleaning with low pressure RF plasma”, H. M. Fernández, D. Rogler, G. Sauthier, M. Thomasset, R. Dietsch, V. Carlino and E. Pellegrin, *Sci. Rep.*, **2018**, *8(1)*, 1–13.
 38. “Contamination removal from EUV multilayer using atomic hydrogen generated by heated catalyze”, H. Oizumi, H. Yamanashi, I. Nishiyama, K. Hashimoto, S. Ohsono, A. Masuda, A. Izumi and H. Matsumura, *SPIE*, **2005**, *5751*, 1147–1154.
 39. “Ultraviolet depolymerization of photoresist polymers,” D. A. Bolon and C. Kunz, *J. Polym. Engin. Sci.*, **1972**, *12*, 109–111.
 40. “Ultraviolet/ozone cleaning of a soft x-ray grating contaminated by synchrotron radiation”, T. Harada, S. Yamaguchi, M. Itou, S. Mitani, H. Maezawa, A. Mikuni, W. Okamoto and H. Yamaoka, *Appl. Opt.*, **1991**, *30 (10)*, 1165–1168.
 41. “Cleaning of optical surfaces with photogenerated reactants”, R. W. C. Hansen, J.

- Wolske, D.Wallace and M. Bissen, *Nucl. Inst. Methods Phys. Res. A*, **1994**, 347, 249–253.
42. “Cleaning of extreme ultraviolet lithography optics and masks using 13.5 nm and 172 nm radiation”, K. Hamamoto, Y. Tanaka, T. Watanabe, N. Sakaya, M. Hosoya, T. Shoki, H. Hada, N. Hishinuma, H. Sugahara and H. Kinoshita, *J. Vac. Sci. Technol. B*, **2005**, 23(1), 247–251.
 43. “Use of zero order synchrotron radiation for in-situ cleaning of beamline optics: Results of trial experiments”, P. K. Yadav, R. K. Gupta and M. H. Modi, *AIP Conf. Proc.*, **2019**, 2115, 30290 (1-4).
 44. “An investigation into the feasibility and characteristics of using a 2.5 kW high power diode laser for paint stripping”, M. J. J. Schmidt, L. Li and J. T. Spencer, *J. Mater. Process. Technol.*, **2003**, 138 (1–3), 109–115.
 45. “Corrosion behaviour of laser-cleaned AA7024 aluminium alloy”, F.D. Zhang, H. Liu, C. Suebka, Y.X. Liu, Z. Liu, W. Guo, Y.M. Cheng, S.L. Zhang and L. Li, *Appl. Surf. Sci.*, **2018**, 435, 452–461.
 46. “Laser cleaning of steel for paint removal”, G. X. Chen, T. J. Kwee, K. P. Tan, Y. S. Choo and M. H. Hong, *Appl. Phys. A*, **2010**, 101(2), 249–253.
 47. “Cleaning of carbon layer from the gold films using a pulsed Nd:YAG laser”, A. Singh, A. Choubey, M. H. Modi, B.N. Upadhyaya, S.M. Oak, G.S. Lodha and S.K. Deb, *Appl. Surf. Sci.*, **2013**, 283, 612–616.
 48. “Towards chemically neutral carbon cleaning processes : plasma cleaning of Ni , Rh and Al reflective optical coatings and thin Al filters for free-electron lasers and synchrotron beamline applications research papers,” H. Moreno Fernandez, M.Zangrando, G. Sauthier, A.R. Goni, V.Carlino, and E. Pellegrin, *J. Synchrotron Radiat.*, **2018**, 25, 1642–1649.
 49. “Understanding plasma sources”, A. Ganguli and R. D. Tarey, *Curr. Sci.*, **2002**, 83(3), 279–290.
 50. “Principle of plasma discharges and material processing”, M. A. Lieberman and Allan J. Lichtenberg, Second Edition. Wiley, **2005**, 387–460.
 51. “UV/Ozone cleaning of surfaces”, J. R. Vig, *J. Vac. Sci. Technol. A*, **1985**, 3(3), 1027–1034.

52. "Surface cleaning mechanisms utilizing VUV radiation in oxygen containing gaseous environments surface cleaning mechanisms utilizing VUV radiation in oxygen containing gaseous environments", Z. Falkenstein, *Proc. SPIE*, **2001**, 4440, 246–255.
53. "Cleaning characteristics of contaminated imaging optics using 172 nm radiation", K. Tanaka, K. Hamamoto, N. Sakaya, M. Hosoya, T. Watanabe and H. Kinoshita, *Jpn. J. Appl. Phys.*, **2007**, 46(9B), 6150–6154.
54. "Laser processing and chemistry", D.Bäuerle, Third Edition, Berlin: Heidelberg, **2000**.
55. "The total reflection of X-rays" A. H. Compton, *Philos. Mag.*, **1923**, 45, 1121-1131.
56. "High-Resolution X-ray scattering from thin films and multilayers", V. Holy, U. Pietsch and T. Baumbach, *Springer*, Berlin, Germany, **1999**.
57. "Introduction to X-ray reflectivity", K. Sakurai, *Kodansha Scientific*, Tokyo, Japan, **2009**.
58. "Influence of surface roughness on near-surface depth analysis from X-ray reflectivity measurements", Y. Fujii, *Surf. Interface Anal.*, **2010**, 42(10–11), 1642–1645.
59. "Simple method of surface characterization by X-ray scattering at small glancing angle of incidence using a compact UHV X-ray diffractometer", Y. Fujii and T. Nakayama, *Surf. Interface Anal.*, **2008**, 40 (13), 1722–1724.
60. "X-ray reflectivity and diffuse scattering" A.Gibaud and S.Hazra, *Current Science* **2000**, 78(12), 1467-1477.
61. "*Elements of modern X-ray physics*", J. A. Nielsen and D. McMorrow, *John Wiley & Sons, New York, USA*, **2001**.
62. "A soft x-ray reflectivity beamline for 100-1500 eV energy range at Indus-2 synchrotron radiation source", M.H. Modi, R. K. Gupta, S. R. Kane, V. Prasad, C. K. Garg, P. Yadav, V. K. Raghuvanshi, A. Singh and M. Sinha., *AIP Conf. Proc.*, **2019**, 2054, 60022 (1–6).
63. "Introduction to magnetic materials" B. D. Cullity and C. D. Graham, *John Wiley & Sons. Inc., New Jersey*, **1969**.

64. "X-ray total external reflection Bragg diffraction: A structural study of the GaAs-Al interface", W. C. Marra, P. Eisenberger and A. Y. Cho, *J. Appl. Phys.*, **1979**, 50(11), 6927–6932.
65. "Angle dispersive X-ray diffraction beamline on Indus-2 synchrotron radiation source: Commissioning and first results," A. K. Sinha, A. Sagdeo, P. Gupta, A. Upadhyay, A. Kumar, M. N. Singh, R. K. Gupta, S. R. Kane, A. Verma and S. K. Deb, *J. Phys. Conf. Ser.*, **2013**, 425, 072017(7–11),
66. "Bonding state of silicon segregated to α -iron surfaces and on iron silicide surfaces studied by electron spectroscopy", B. Egert and G. Panzner, *Phys. Rev. B*, **1984**, 29 (4), 2091–2101.
67. "Formation of epitaxial $\text{Fe}_{3-x}\text{Si}_{1+x}$ ($0 \leq x \leq 1$) silicides on Si (111)", S. Hong, P. Wetzel, G. Gewinner, D. Bolmont and C. Pirri, *J. Appl. Phys.*, **1995**, 78(9) 5404–5410.
68. "The effect of oxygen on the formation of iron silicide", H. C. Swart and G. L. P. Berning, *Appl. Surf. Sci.*, **1994**, 78, 77–82.
69. "On a heuristic point of view about the creation and conversion of light?," A. Einstein, *Ann. Phys.*, **1905**, 17(132), 91-107.
70. "Handbook of X-ray photoelectron spectroscopy", J. F. Moulder, W. F. Stickle, P. E. Sobol and K. D. Bomben, *ULVAC-PHI, Inc.*, **1992**.
71. "Comparison of background removal methods for XPS", M. Repoux, *Surf. Interface Anal.*, **1992**, 18(7), 567–570.
72. "Atomic Force Microscope", G. Binnig, C. F. Quate and C. Gerber, *Phys. Rev. Lett.*, **1986**, 56(9), 930–933.
73. "Scanning Probe Microscopy of Thin Films", S. M. Hues, R. J. Colton, E. Meyer and H. Giintherodt, *MRD Bull.*, **1993**, 41–49.
74. "Modern Spectroscopy", M. Hollas, Fourth Edition. Wiley, **2004**.
75. "Light Scattering in Solids I.", R. M. Martin and L. M. Falicov, Springer Series, Berlin, **1983**.
76. "Raman scattering of carbon disulfide: The temperature effect", D. Wang, K. Mittauer, N. Reynolds, *Am. J. Phys.*, **2009**, 77(12), 1130–1134.
77. "Theoretical background of optical emission spectroscopy for analysis of

- atmospheric pressure plasmas”, T. Belmonte, C.Noel, T. Gries, J. Martin and G.Henrion, *Plasam Sources Sci. Technol.* **2015**, *064004*, 1-29,
78. “Preparation and properties of highly tetrahedral hydrogenated amorphous carbon”, M. Weiler, S. Sattel, T. Giessen, K. Jung and H. Ehrhardt, *Phys. Rev. B*, **1996**, *53(3)*, 1594–1608.
 79. “Diamond-like carbon for data and beer storage”, C. Casiraghi, J. Robertson and A. C. Ferrari, *Mater. Today*, **2007**, *10(1)*, 44–53.
 80. “Diamond-like amorphous carbon”, J. Robertson, *Mater. Sci. Eng.*, **2002**, *37*, 129–281.
 81. “Amorphous carbon”, J. Robertson, *Adv. Phys*, **1986**, *35*, 317–374.
 82. “EUV-driven carbonaceous film deposition and its photo-oxidation on a TiO₂ film surface”, N. S. Faradzhev, M. Mcentee, J. T. Yates, S. B. Hill and T. B. Lucatorto, *J.Phys. Chem. C*, **2013**, *117*, 23072–23081.
 83. “Surface studies of solids by total reflection of X-rays”, L. G. Parratt, *Phys. Rev.*, **1954**, *95 (2)*, 359–369.
 84. “Live simulator and data analysis tool for multilayer reflectivity using LabVIEW”, M. H. Modi, G. S. Lodha, and M. I. P. Mercere, The 9th International Conference on the Physics of X-Ray Multilayer Structures, Big Sky Resort USA, 2008.
 85. “Study of stacking structure of smorphous carbon by X-ray diffraction technique”, B. Manoj and A. G. Kunjomana, *Int. J. Electrochem. Sci.*, **2012**, *7*, 3127–3134.
 86. “Interlayer spacing anomaly of single-wall carbon nanohorn aggregate”, S. Bandow, F. Kokai, K. Takahashi, M. Yudasaka, L. C. Qin and S. Iijima, *Chem. Phys. Lett.*, **2000**, *321*, 514–519.
 87. “Structural investigation of graphitic carbon nitride via XRD and neutron diffraction structural investigation of graphitic carbon nitride via XRD and Neutron Diffraction”, F. Fina, S. K. Callear, G. M. Carins and John T. S. Irvine, *Chem. Mater.*, **2015**, 1–9.
 88. <http://www.phy.cuhk.edu.hk/~surface/XPSPEAK/forXPSPEAK4.1>.
 89. “Combined time-of-flight secondary ion mass spectrometry and X-ray photoelectron spectroscopy study of the surface segregation of soly (methyl methacrylate) (PMMA) in Bisphenol A Polycarbonate PMMA Blends”, J. Lhoest,

- P. Bertrand, L. T. Weng and J. Dewed, *Macromolecules*, **1995**, 28, 4631–4637.
90. “Advances in charge neutralization for XPS measurements of nonconducting materials”, G. Barth, R. Linder and C. Bryson, *Surf. Interface Anal.*, **1988**, 11, 307–311.
 91. “Applications of ESCA to polymer chemistry. XVII . Systematic investigation of the core levels of simple homo polymers”, D. T. Clark and H. R. Thomas, *J. Polym. Sci.*, **1978**, 16, 791–820.
 92. “Structural modifications in the amino acid lysine induced by soft x-ray irradiation”, M. J. Bozack, Y. Zhou and S. D. Worley, *J. Chem. Phys.*, **2011**, 100(11), 8392–8398.
 93. “Treatment of poly (ether ether ketone) (PEEK) surfaces by remote plasma discharge. XPS investigation of the ageing of plasma-treated”, C. Jama, O. Dessaux, P. Goudmand, L. Gengembre and J. Grimblot, *Surf. Interface Anal.*, **1992**, 18, 751–756.
 94. “An investigation of the surface chemistry of poly (ether etherketone). I . The effect of oxygen plasma treatment on surface structure”, D. J. Pawson, A. P. Ameen, R. D. Short, P. Denison and F. R. Jones, *Surf. Interface Anal.*, **1992**, 18, 13–22.
 95. “X-ray photoelectron spectra of methyl lithium and dilithiomethane”, G. F. Meyers, I. M. B. Hall, J. W. Chinn and R. J. L. Ib, *J. Am. Chem. Soc.*, **1985**, 107, 1413–1414.
 96. “Adsorption of carbon monoxide on Ni/Ti and Ni/TiO₂ surfaces prepared in-situ in the electron spectrometer: A combined UPS-XPS study”, M. K. Rajumon, M.S. Hegde and C.N.R. Rao, *Catal. Lett.* 1, **1998**, 1(565), 351–359.
 97. "The strong metal support interaction (SMSI) in Pt-TiO₂ model catalysts. A new CO adsorption state on Pt-Ti atoms”, C. Ocal and S. Ferrer, *J. Chem. Phys.*, **1986**, 84(11), 6474–6478.
 98. "Characteristic Raman frequencies of organic compounds" F. R. Dollish, W. G. Fateley and F. F. Bentley, Wiley, New York, **1974**.
 99. “Bonding in hydrogenated diamond-like carbon by Raman spectroscopy”, C. Casiraghi, F. Piazza, A. C. Ferrari, D. Grambole and J. Robertson, *Diam. Relat.*

- Mater*, **2005**, 14, 1098-1102.
100. "Raman Spectrum of Graphite", F. Tuinstra and J. L. Koenig, *J. Chem. Phys.*, **1970**, 53, 1126–1130.
 101. "Resonant Raman spectroscopy of disordered, amorphous and diamond-like carbon", A. C. Ferrari and J. Robertson, *Phys. Rev. B*, **2001**, 64, 75414(1-13).
 102. "Interpretation of Raman spectra of disordered and amorphous carbon," A. C. Ferrari and J. Robertson, *Phys. Rev. B*, **2000**, 61(20), 95–107.
 103. "Characterization of diamond films by Raman spectroscopy", D. S. Knight and W. B. White, *J. Mater. Res*, **1989**, 4, 385–393.
 104. "Raman scattering from high-frequency phonons in supported n-Graphene layer Films," A. Gupta, G. Chen, P. Joshi, S. Tadigadapa and P. C. Eklund, *NanoLett.*, **2006**, 6(12), 2667–2673.
 105. "Photoluminescence and Raman spectroscopy in hydrogenated carbon films", B. Marchon, J. Gui, K. Grannen, G. C. Rauch., *IEEE Trans. Magn.*, **1997**, 33(5), 3148–3150.
 106. "Plasma etching: An introduction", D. M. Manos and D. L. Flamm, Academic Press, New York, **1989**.
 107. "Gas discharge plasmas and their applications," A. Bogaerts, E. Neyts, R. Gijbels and J. Van Der Mullen, *Spectrochim. Acta Part B*, **2002**, 57, 609–658.
 108. "Cold plasma in material fabrication: from fundamentals to applications", A. Grill, IEEE Press, New York, **1994**.
 109. "Pulse-time modulated plasma discharge for highly selective, highly anisotropic and charge-free etching", S. Samukawa and T. Mieno, *Plasma Sources Sci. Technol.*, **1996**, 5, 132–138.
 110. "Resuscitation of carbon-contaminated mirrors and gratings by oxygen-discharge cleaning. 2 : Efficiency recovery in the 100-1000-eV range", T. Koide, T. Shidara, M. Yanagihara and S. Sato, *Appl. Opt.*, **1988**, 27(20), 4305–4313.
 111. "Removal of carbon contamination on silicon wafer surfaces by microwave oxygen plasma", A. Thedsakhulwong and W. Thowladda, *J.Met. Mater. Miner.*, **2008**, 18(2), 137–141.
 112. "Vacuum technology and coatings", A. Belkind and S. Gershman, *Vac. Coat.*

- Technol.*, **2008**, 46–57.
113. “Surface treatment of metals using an atmospheric pressure plasma jet and their surface characteristics”, M. C. Kim, S. H. Yang, J. Boo and J. G. Han, *Surf. Coatings Technol.*, **2003**, 174–175, 839–844.
 114. “Characteristics of GaAs substrate”, Y. Wang, Lu Zhou, B. Jia, D. Bai, Xu Yang, Xin Gao and B. Bo, *ICOM*, **2012**, 61177019, 16–20.
 115. “Optical emission spectroscopy characterization of oxygen plasma during treatment of a PET foil”, N. Krstulovic, I. Labazan, S. Milosevic, U. Cvelbar, A. Vesel and M. Mozetic *J. Phys. D. Appl. Phys.*, **2006**, 39, 3799–3804,
 116. “Hydrocarbon bond dissociation energies”, D. F. McMillen and D. M. Golden, *Ann. Rev. Phys. Chem.*, **1982**, 33, 493–532.
 117. “Bond dissociation energies of organic molecules”, S. J. Blanksby and G. B. Ellison, *Acc. Chem. Res.*, **2002**, A-I.
 118. “Effect of surface contamination on the thermo compression bondability of gold”, J. L. Jellison, *IEEE Trans. Parts, Hybrids, Packag.*, **1975**, PHP-11, 206–211.
 119. “Surface cleaning by ultraviolet radiation”, R. R. Sowell, R. E. Cuthrell, D. M. Mattox and R. D. Bland, *J. Vac. Sci. Technol.*, **1974**, 11(1), 474–475.
 120. “Restoration of absolute diffraction efficiency and blaze angle of carbon contaminated gratings by ultraviolet cleaning,” M. Kumar, M. H. Modi, H. Singhal, S. Sendhil Raja, J. A. Chakera, R. K. Gupta, P. A. Naik, G. S. Lodha, and P. D. Gupta, *Appl. Opt.*, **2013**, 52(8), 1725–1730.
 121. “UV/Ozone Cleaning of Surfaces”, J. R. Vig, and J. W. LeBus, *IEEE Trans. Parts, Hybrids Packag.*, **1976**, PHP-12, 365–370.
 122. “HAXPES beamline PES-BL14 at the Indus-2 synchrotron radiation source”, Jagannath, U. K. Goutam, R. K. Sharma, J. Singh, K. Dutta, U. S. Sule, R. Pradeep and S. C. Gadkari, *J. Synchrotron Rad.*, **2018**, 25, 1541–1547.
 123. “UV-Degradation Effect on Optical and Surface Properties of Polystyrene-TiO₂ Nanocomposite Film”, B. Jaleh, M. Shayegani Madad, M. Farshchi Tabrizi, S. Habibi, R. Golbedaghi and M. R. Keymanesh, *J. Iran. Chem. Soc.*, **2011**, S161–S168.
 124. “UV irradiation influence on the structural and optical properties of CdO thin

- films”, C. Dantus, D. Timpu, D. Luca, F. Iacomi, *Eur. Phys. J. Appl. Phys.*, **2012**, 1-14.
125. Preparation, structure evolution and dielectric properties of BaTiO₃ thin films and powders by an aqueous sol - gel process”, B. Lee and J. Zhang, “*Thin Solid Films*”, **2001**, 388, 107–113.
126. “NIR FT Raman spectroscopic study of flame soot”, B. Dippel, H. Jander and J. Heintzenberg, *Phys. Chem. Chem. Phys.*, **1999**, 1, 4707–4712.
127. “Laser cleaning of steel for paint removal”, G.X. Chen, T. J. Kwee, K. P. Tan, Y. S. Choo and M. H. Hong, *Appl Phys A*, **2010**, 101, 249–253.
128. “Femtosecond, picosecond and nanosecond laser ablation of solids”, B. N. Chichkov, C. Momma, S. Nolte, F. Von Alvensleben and A. Tu, *Appl. Phys. A* **1996**, 63, 109–115.
129. “Influence of laser pulse shape on dry laser cleaning”, D. Grojo, M. Boyomona, A. Cros, and P. Delaporte, *Appl. Surf. Sci.*, **2006**, 252, 4786–4791.
130. “A theoretical investigation of the laser damage threshold of metal multi-dielectric mirrors for high power ultrashort applications”, B. Wang and L. Gallais, **2013**, 21(12), 2686–2689.
131. “Laser-induced damage thresholds of gold, silver and their alloys in air and water”, S. V. Starinskiy, Y. G. Shukhov and A. V. Bulgakov, *Appl. Surf. Sci.*, **2017**, 396, 1765–1774.
132. “Pulsed Laser Heating and Melting”, D. Sands, *Heat Transfer Engineering Applications*, **2011**, 47–70.
133. “Ultrafast ablation with high-pulse-rate lasers. Part I: Theoretical considerations”, E. G. Gamaly, A. V. Rode and B. Luther-Davies, *J. Appl. Phys.*, **1999**, 85(8), 4213–4221.
134. “Selective laser sintering of parts by compound formation of precursor powders”, D. L. Bourell, H. L. Marcus, J. W. Barlow and J. J. Beaman, *Int. J. Powder Met.*, **1992**, 28(4), 369–381.
135. “Rapid surface heat treatments- a review of laser and electron beam hardening”, A. J. Hick, *Heat Treat. Met.*, **1983**, 10 (1), 3–11.
136. “Laser Material Processing”, W. M. Steen, Third Edition. Springer, London **2003**.

137. "Solute trapping: Comparison of theory with experiment," M. J. Aziz, J. Y. Tsao, M. O. Thompson, P. S. Peercy and C. W. White, *Phys. Rev. Lett.*, **1986**, 56 (23), 2489–2492.
138. "Controlled super lateral growth of Si films for microstructural manipulation and optimization", J. S. Im, M. A. Crowder, R. S. Sposili, J. P. Leonard, H. J. Kim, J. H. Yoon, V. V. Gupta, H. J. Song and H. S. Cho, *Phys. Status Solidi A Appl. Res.*, **1998**, 166(2), 603–617.
139. "Marangoni mechanism in pulsed laser texturing of magnetic disk substrates", T. D. Bennett, D. J. Krajnovich, C. P. Grigoropoulos, P. Baumgart and A. C. Tam, *J. Heat Transf.*, **1997**, 119(3), 589–596.
140. "Preferential vaporization during laser ablation inductively coupled plasma atomic emission spectroscopy" X. L. Mao, A. C. Ciocan and R. E. Russo, *Appl. Spectrosc.*, **1998**, 52(7), 913–918.
141. "Coulomb explosion in ultrashort pulsed laser ablation of Al₂O₃", R. Stoian, D. Ashkenasi, A. Rosenfeld and E. E. B. Campbell, **2000**, 62(19), 167–173.
142. "Laser cleaning of stone artefacts : A substitute or alternative method?," G. Lanterna and M. Matteini, *J. Cult. Herit.*, **2000**, 1, S29–S35.
143. "Effect of pulsing parameters on laser ablative cleaning of copper oxides," J. Zhang, Y. Wang, P. Cheng and Y. L. Yao, *ICALEO*, **2005**, 602, 276–285.
144. "Preliminary study on the laser cleaning of stainless steels after high temperature oxidation", P. Psyllaki and R. Oltra, *Mater. Sci. Eng. A*, **2000**, 282, 145–152.
145. "Effect of laser treatment on the surface of copper alloys," H. Garbacz, E.F. Zalesna, J. Marczak, A. Koss, A. Zatorska, G. Z. Zukowska, T. Onyszczyk, K. J. Kurzydowski, *Appl. Surf. Sci.*, **2011**, 257 (17), 7369–7374.
146. "Pulsed-laser-induced nanoscale island formation in thin metal-on-oxide films", S. J. Henley, J. D. Carey and S. R. P. Silva, *Physical Rev. B*, **2005**, 72, pp. 195408 (1–10).
147. "Raman Spectroscopy Optimizes Graphene Characterization", M. Wall, *Adv. Mater. Process.*, **2012**, 35–38.
148. "Film texture evolution in plasma treated TiN thin films", S. Ikeda, J. Palleau, J. Torres, B. Chenevier, N. Bourhila and R. Madar, *J. Appl. Phys.*, **1999**, 86(4),

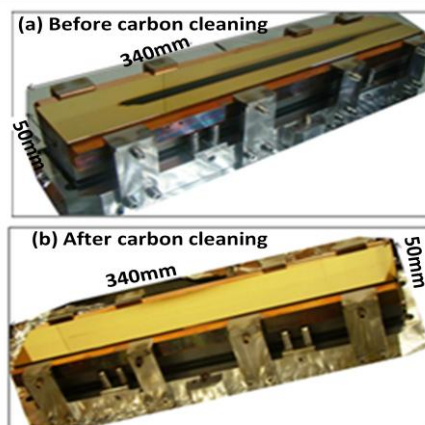
2300–2306.

149. “Thermal annealing using ultra-short laser pulses to improve the electrical properties of Al : ZnO thin films”, D. Scorticati, A. Illiberi, T.C. Bor, S.W.H. Eijt, H. Schut, G.R.B.E. Römer, M. Klein Gunnewiek, A.T.M. Lenferink, B.J. Kniknie, R. Mary Joy, M.S. Dorenkamper, D.F. de Lange, C. Otto, D. Borsa, W.J. Soppe and A. J. Huis in ’t Veld, *Acta Mater.*, **2015**, 98, 327–335.
150. “Carbon removal from a mirror-like gold surface by UV light , RF plasma , and IR laser exposure : a comparative study,” P. K. Yadav R. K. Gupta, A. K. Choubey S. Ali, U. K. Goutam, and M. H. Modi, *Applied Optics*, **2021**, 60(1), 89-97.
151. “Nanoparticle formation by the debris produced by femtosecond laser ablation of silicon in ambient air,” N. G. Semaltianos, W. Perrie, V. Vishnyakov, R. Murray, C. J. Williams and S. P. Edwardson, *Mater. Lett.*, **2008**, 62, 2165–2170.
152. “A comparison between X-ray reflectivity and atomic force microscopy on the characterization of a surface roughness”, H. C. Su, C. H. Lee, M. Z. Lin, and T.W. Huang., *Chin. J. Phys.*, **2012**, 50, 291-300.
153. “The thickness dependent of optical properties, resistance, strain and morphology of Mo thin films for the back contact of CIGS solar cells”, C. H. Lee, F.G. Guo and C.C. Chu, *Chin. J. Phys.*, **2012**, 50(2), 311-321.
154. “Raman spectroscopy of graphene and graphite : Disorder , electron phonon coupling, doping and nonadiabatic effects”, A. C. Ferrari, *Solid State Commun.*, **2007**, 143, 47–57.
155. “A review of theoretical models of adsorption, diffusion, desorption, and reaction of gases on metal surfaces,” S. J. Lombard and A. T. Bell, *Surface Science Reports*, **1991**, 13, 1-72.
156. “Thermal Desorption From Metal Surfaces: A Review”, D. A. King, *Surf. Sci.*, **1975**, 47, 384–402.
157. "Microbiology of waterborne diseases", N. F.Gray, Second Edi. **2014**.
158. “RP Photonics Encyclopedic”, R. Paschotta, [Online] https://www.rp-photonics.com/excimer_lamps.html.
159. “Tunable excimer lasers”, R. C. Sze and D. G. Harris, *Tunable Lasers Handbook*, Academic Press, Inc., **1990**, 33–61.

160. "On the classical radiation of accelerated electrons", J. Schwinger, *Phys. Rev.*, **1949**, 75 (12), 1912–1925.
161. "Theory of synchrotron radiation. In: Particle accelerator physics. graduate texts in physics", H. Wiedemann, *Springer*, Cham, **2015**.
162. "Cleaning force in laser cleaning of silicon substrate, D. M. L. and T. S. L. W.D Song, Y.F. Lu, K.D. Ye, C.K.Tee, M.M.Hong, SPIE, 1997, 3184, 158-165.
163. "A thermal detachment mechanism for particle removal from surfaces by pulsed laser irradiation", J. D. Kelley and F. E. Hovis, *Microelectron. Eng.*, **1993**, 20, 159–170.
164. "Laser surface cleaning of carbonaceous deposits on diesel engine piston", Y. C. Guan, G. K. L. Ng, H. Y. Zheng, M. H. Hong, X. Hong and Z. Zhang, *Appl. Surf. Sci.*, **2013**, 270, 526–530.
165. "Comparative study of ornamental granite cleaning using femtosecond and nanosecond pulsed lasers", T. Rivas, A. J. Lopez, A. Ramil, S. Pozo, M. P. Fiorucci, M. E. López de Silanes, A. García, J. R. Vazquez de Aldana, C. Romero and P. Moreno, *Appl. Surf. Sci.*, **2013**, 278, 226–233.
166. "Theoretical and experimental studies on molybdenum and stainless steel mirrors cleaning by high repetition rate laser beam", A. Leontyev, A. Semerok, D. Farcage, P.Y. Thro, C. Grisolia, A. Widdowson, P. Coad, M. Rubel and JET-EFDA contributors, *Fusion Eng. Des.*, **2011**, 86, 1728–1731,
167. "Laser-cleaning techniques for removal of surface particulates particulates," A. C. Tam, W. P. Leung, W. Zapka and W. Ziemlich, *J. Appt. Phys.*, **1992**, 71(7), 3515–3522.

Thesis Highlights

Synchrotron radiation (SR) induced carbon contamination on optical elements is a serious issue in SR beamlines. In order to know characteristics of SR induced carbon layer on optical elements, SR induced carbon contaminated Au coated toroidal mirror of reflectivity beamline and a LiF window of high resolution vacuum ultraviolet beamline of Indus-1 are taken for a case study. Detailed analysis



of carbon contaminated Au mirror surface reveals that nature of carbon growth has direct correlations with synchrotron dose. Raman study

Figure-1: *Synchrotron radiation induced carbon contaminated Au coated spherical mirror before (a) and after (b) rf plasma cleaning.*

shows that carbon layer has mixed phases of sp^3 and sp^2 hybridized carbon contents, number of carbon layers, disordering and cluster size in the layer increases with photon dose. The contamination layer has presence of hydrogen (hydrogenated carbon layer) and hydrogen contents decrease with photon dose. Soft X-ray reflectivity results indicate that optical density of carbon layer in maximum thickness region is about 75% with respect to graphitic carbon and surface roughness is nearly 60 Å. The Raman Spectroscopy and XPS results of carbon layer deposited on LiF window surface also show graphitic carbon nature.

In order to refurbish the contaminated optics, a capacitively coupled RF plasma system is in-house developed, IR laser (Yb:YAG) system is customized and excimer based ($\lambda=172$ nm) UV source is installed in the laboratory. The system parameters are optimized such that the process does not damage the Au or Pt coating of actual mirror. At optimized parameters the system was successfully used to clean different mirrors of Indus synchrotron beamlines. A SR induced gold coated spherical mirror before and after rf plasma cleaning is shown in fig-1. An in-situ cleaning technique using zero order SR is deployed at Indus-1 reflectivity beamline for post mirror cleaning. In order to find out merits and demerits of cleaning techniques results of all three techniques are compared. The results of comparative study suggest that UV and rf plasma cleaned samples show gain in the soft x-rays reflectivity near carbon K-edge region in comparison to carbon coated Au sample whereas the IR laser treated sample showed reflectivity gain near carbon K-edge region but not upto pristine Au surface reflectivity.